
**Measurement of thermodynamic data at elevated
pressure and temperature conditions with a microfluidic
setup**

Der Fakultät für Maschinenbau, Verfahrens- und Energietechnik der Technischen
Universität Bergakademie Freiberg
genehmigte

Dissertation

zur Erlangung des akademischen Grades Doktor-Ingenieur (Dr. Ing.)

vorgelegt

von

Michael Hubertus Horst Fechter, M. Sc.

Geboren am 05.10.1991 in Lichtenfels, Bundesrepublik Deutschland

Gutachter: Prof. Dr.-Ing. Andreas S. Bräuer, Freiberg, Deutschland

Prof. PhD Cara Schwarz, Stellenbosch, Südafrika

Freiberg, den 28.09.2023

Versicherung

Hiermit versichere ich, dass ich die vorliegende Arbeit ohne unzulässige Hilfe Dritter und ohne Benutzung anderer als der angegebenen Hilfsmittel angefertigt habe; die aus fremden Quellen direkt oder indirekt übernommenen Gedanken sind als solche kenntlich gemacht.

Bei der Auswahl und Auswertung des Materials sowie bei der Herstellung des Manuskripts habe ich Unterstützungsleistungen von folgenden Personen erhalten:

Prof. Dr. Andreas Siegfried Bräuer

Weitere Personen waren an der Abfassung der vorliegenden Arbeit nicht beteiligt. Die Hilfe eines Promotionsberaters habe ich nicht in Anspruch genommen. Weitere Personen haben von mir keine geldwerten Leistungen für Arbeiten erhalten, die nicht als solche kenntlich gemacht worden sind. Die Arbeit wurde bisher weder im Inland noch im Ausland in gleicher oder ähnlicher Form einer anderen Prüfungsbehörde vorgelegt.

Danksagung

Die Dissertation sei meiner Frau Tijana, Tochter Milena, sowie meinen Eltern Claudia und Horst gewidmet. Vielen Dank für eure vielfältige Motivation und Unterstützung, ohne welche ich nicht diese Arbeit verfasst hätte. Danke für das Geschehene und für alles was noch kommen wird!

Ich möchte mich ferner hiermit bei allen Personen bedanken, die innerhalb der letzten 5 Jahre dazu beigetragen haben, dass ich meine wissenschaftliche Tätigkeit hiermit erfolgreich abschließen kann.

Hierbei vor allem bei meinem Promotionsbetreuer, Arbeitsgruppenleiter und Vorgesetztem Professor Andreas Bräuer, der mir trotz damaliger geringer Kenntnisse in Disziplinen wie Phasengleichgewichtsthermodynamik, Hochdrucktechnik oder Optik eine Stelle als wissenschaftlicher Mitarbeiter in seiner Arbeitsgruppe ermöglichte. Besonders hervorzuheben ist die direkte Hilfe bei allen praktischen oder theoretischen Fragen einschließlich unzähliger spontaner Besprechungen, das geschenkte Vertrauen bei Home-Office-Tätigkeiten während der Pandemiezeit oder die aktive Förderung durch das Ermöglichen von Konferenzbesuchen.

Ferner bedanke ich mich bei allen früheren oder jetzigen Kollegen aus dem Institut und der Arbeitsgruppe, unter anderem bei Martin Dirauf, Mirko D'Auria und Matthias Grumann, mit welchen ich einst das „Projekt Promotion“ am ITUN anging und welche mir zusammen mit Tobias Klima und Medhanie Gebrekidan vor allem in der Anfangszeit mit Rat und Tat zur Seite standen.

Weiterhin möchte ich mich auch bei den Leitern der Werkstätten, Jan Radzynski und Clemens Lütgert bedanken, ohne welche die technische Umsetzung experimenteller Vorhaben nicht möglich gewesen wäre. Ebenfalls Dank gebührt Frau Jana Latte für die Abwicklung hunderter Bestellungen, Dr. Volker Herdegen für die Hilfe bei Fragen rund um die Hochdrucktechnik, sowie Dr. Roland Haseneder für Hilfestellungen bei diversen chemischen Fragen.

Abstract

With this thesis, I present an experimental study focusing on the provision of thermodynamic data of fluids at elevated pressure and temperature conditions. Hereby a microcapillary setup that is equipped with an *in situ* Raman Spectroscopy unit as well as with a high-speed camera, was further improved within the scientific employment of the author. The setup consists in principle of a fused-silica microcapillary embedded in a heating block, which is furthermore connected to high pressure syringe pumps.

Pure compounds and mixtures were studied with the microfluidic setup and different thermodynamic properties were determined. For instance, vapor pressures of Poly(oxymethylene) Dimethyl Ethers (OME₃ and OME₄), a potential class of renewable diesel fuels, were the first time measured for temperatures exceeding the atmospheric boiling temperature. Hereby the regarded compound is pressurized at constant temperature, from what the vapor pressure is determined optically by detecting bubble or film formation, indicating the transition from vapor to liquid state.

The main results of this thesis were however the vapor-liquid equilibria (VLE) of fuel/air-systems that were determined by *in situ* Raman Spectroscopy, whereby the Stokes-scattered Raman signal can be successfully separated phase-dependently by light barrier technology. A further task was the determination of saturated mixture densities of the validation system ethanol/CO₂.

With this study, I intend to contribute to the scarce literature data for the studied systems and properties. Therewith I want to help to enhance the understanding of microprocesses such as the evaporation and mixing formation in diesel combustion engines.

Table of Contents

Versicherung.....	i
Danksagung	ii
Abstract.....	iii
Abbreviations and symbols	vi
Scientific publications	ix
1 Introduction	1
2 State of the art	3
2.1 Vapor pressure measurements	3
2.2 VLE measurements.....	4
2.2.1 Spectroscopic determination of fluid phase equilibria	5
2.2.2 Raman spectroscopy coupled microfluidic devices	7
2.3 Mixture density measurements	8
3 Application oriented fundamentals	10
3.1 Thermodynamic fundamentals	10
3.1.1 p v T -behavior and equilibrium conditions.....	10
3.1.2 Equations of state (EoS)	13
3.1.3 Density correlations.....	16
3.1.4 Clapeyron equation and vapor pressure correlations.....	18
3.1.5 Vapor-liquid phase diagrams.....	19
3.2 Microfluidics.....	22
3.3 Raman spectroscopy	23
3.3.1 Raman spectra	25
3.3.2 Quantitative Raman spectroscopy	25
4 Experimental	28
4.1 Experimental Setup.....	28
4.1.1 Light barrier system for phase-selective measurement	30

4.1.2	Raman probe head	30
4.1.3	Control of experimental setup	31
4.1.4	Preparation of microcapillaries.....	33
4.1.5	Microfluidic behavior and segmented flow.....	34
4.2	Experimental procedure	36
4.2.1	Vapor pressure measurements	36
4.2.2	VLE measurements	37
4.2.3	Mixture density measurements.....	44
4.3	Deviation and measurement uncertainty.....	47
5	Results and discussion.....	49
5.1	Saturated vapor pressure measurements	49
5.1.1	Materials and methods.....	49
5.1.2	Results	49
5.1.3	Conclusion.....	56
5.2	VLE measurements.....	57
5.2.1	Materials and Methods	57
5.2.2	Results	58
5.2.3	Conclusion.....	75
5.3	Mixture density measurements	76
5.3.1	Materials and Methods	76
5.3.2	Results	76
5.3.3	Conclusion.....	77
6	Summary	79
7	Perspective	79
8	Tabulated experimental data	80
9	References	86

Abbreviations and symbols

symbol	description	unit
a	PR-EOS parameter	$\text{Nm}^4 \cdot \text{mol}^{-2}$
AAD	absolute average deviation	%
AD	absolute deviation	%
b	PR-EoS parameter	$\text{m}^3 \text{mol}^{-1}$
b	Tait parameter	variable unit
B	Tait parameter	MPa
c	Tait parameter	variable unit
C	Tait parameter	-
C^2	coefficient of determination	-
d	diameter	m
f	fugacity	MPa
fr	frequency	Hz
F	objective function	-
g_{kl}	pseudo-Voigt parameter	-
g	Molar Gibbs energy	kJ mol^{-1}
$\Delta_{vap}h$	molar latent heat of vaporization	kJ mol^{-1}
H	Henry's law coefficient	MPa
I	Raman intensity (integrated area)	-
k_b	Boltzmann constant	$1.380649 \cdot 10^{-23} \text{J K}^{-1}$
k_{ij}	binary interaction coefficient	-
K_{ij}	binary Raman calibration constant	-
L	adjustable variable	-
m	PC-SAFT parameter (segment diameter)	-
m	mass	kg
np	number of data points	-
nc	number of compounds	-
n	number (e. g. number of property)	-
N_B, N_C	number of Tait parameters	-
M	molar mass	kg mol^{-1}
p	pressure	MPa, bar

<i>prop</i>	property	-
r_{ij}	Raman signal ratio	-
R	universal/ideal gas constant	8.31446 J mol ⁻¹ K ⁻¹
R_{ij}	molar ratio	-
R^2	coefficient of determination	-
S	Raman signal	-
t	global fit parameter (film correction)	-
T	temperature	K
u	uncertainty	variable unit
v	molar volume	m ³ mol ⁻¹
V	volume	m ³
w	phase-independent mass fraction	-
x	liquid phase mole fraction	-
y	vapor phase mole fraction	-
z	phase-independent mole fraction	-
Z	compressibility factor	-
α	PR-EoS pure compound parameter	-
ε	PC-SAFT parameter	J
κ	PC-SAFT parameter	-
ρ	density	kg m ⁻³
φ	fugacity coefficient	-
ω	acentric factor	-
σ	PC-SAFT parameter	m
τ	PPDS parameter for $\Delta_{vap}h$	-
λ	wavelength	nm
$\bar{\nu}$	Raman shift	cm ⁻¹
ν	wavenumber	cm ⁻¹
μ	weighting factor	-

Superscript:

b: boiling; *m*: melting; *s*: at saturation; *vap*: vapor phase; *liq*: liquid phase; *exp*: experimental; *cal*: calculated; *hc, disp, assoc*: denotes PC-SAFT contributions; *PR, PCS*: referring to PR-EoS or PC-SAFT; *: pure;

Subscript:

alk: n-alkane; *a*: type A; *b*: type B; *bub*: bubble; *c*: combined (e. g. in u_c); *cyl*: cylinder; *crit*: critical; *CH – str*, *N₂ – str*, *O₂ – str*, *OH – str*: stretching vibrations; *eth*: ethanol; *k, l*: running variables; *n*: repeating units; *oct*: 1-octanol; *r*: reduced; *sph*: spherical; *unit*: unit cell; *v*: based on volume; *w*: based on weight; *mix*: indicating binary or ternary system; *ref*: reference condition; *Td*: temperature dependent; *OME*: polyoxymethylene dimethyl ether; *0*: standard / reference condition or variable number;

Scientific publications

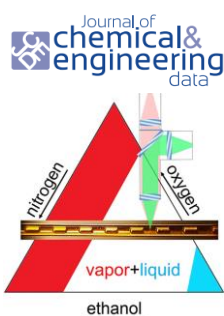
Within the time of the author's scientific employment, the following publications have been released in international peer-reviewed journals. In this thesis however, only the results of the works are discussed, to which the author contributed in 1st-authorship. A 2nd-authorship publication appears in the cumulative dissertation of the respective 1st author Thomas Deleau, for what it is not included in this thesis.

Determination of mass transfer coefficients in high-pressure two-phase flows in capillaries using Raman spectroscopy;

Authors: T. Deleau, M. H. H. Fechter, J-J. Letourneau, S. Camy, J. Aubin, A. S. Braeuer, F. Espitalier

Chemical Engineering Science 2020, 228, 115960;

DOI: <https://doi.org/10.1016/j.ces.2020.115960>



Vapor–Liquid Equilibria of Mixtures Containing Ethanol, Oxygen, and Nitrogen at Elevated Pressure and Temperature, Measured with In Situ Raman Spectroscopy in Microcapillaries;

Authors: Michael H. H. Fechter and Andreas S. Braeuer

J. Chem. Eng. Data 2020, 65, 7, 3373–3383

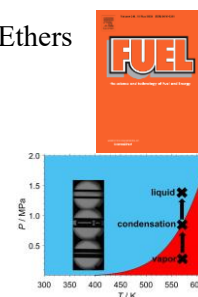
DOI: <https://doi.org/10.1021/acs.jced.0c00184>

Vapor pressures and latent heats of vaporization of Poly(oxyethylene) Dimethyl Ethers (OME₃ and OME₄) up to the vicinity of the critical temperature;

Authors: M. H. H. Fechter, P. Haspel, C. Hasse, A.S. Braeuer

Fuel 2021, 303, 121274;

DOI: <https://doi.org/10.1016/j.fuel.2021.121274>

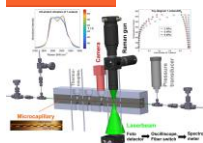


Vapor-Liquid equilibria of the systems 1-octanol/nitrogen and 1-octanol/oxygen at pressures from 3 to 9 MPa and temperatures up to 613 K – Measured in a microcapillary with Raman spectroscopy;

Authors: M. H. H. Fechter, J. Koschack, A. S. Braeuer

Fuel 2022, 323, 124352

DOI: <https://doi.org/10.1016/j.fuel.2022.124352>

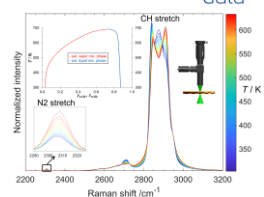


Vapor-Liquid Equilibria of binary systems consisting of nitrogen and n-tridecane, n-pentadecane, n-hexadecane and n-heptadecane at pressures of 1.5 - 9 MPa and temperatures of 303 – 633 K – determined with a Raman Spectroscopy coupled microfluidic device

Authors: M. H. H. Fechter and A. S. Braeuer

J. Chem. Eng. Data (accepted manuscript, June 2023)

DOI: <https://doi.org/10.1021/acs.jced.3c00107>



1 Introduction

How accurately can a chemical plant be designed or a thermodynamic process be modeled? One of the answers to this question lies in the thermodynamic data that is considered by the engineer for the regarded task. Especially at conditions that deviate from ambient temperature and pressure, it can be difficult to find for pure fluids or mixtures either an accurate dataset or to choose a suitable model with appropriate input parameters.

A process that takes place at those elevated conditions is for instance an injection inside a diesel combustion chamber, where a fuel that is at the beginning of the process in liquid state is heated up, partially evaporated and mixed with the oxidizer air before the fuel/air mixture eventually self-ignites. Along these micro processes of injection, heat-up and spray-formation, different thermodynamic properties are of relevance in order to model and understand these phenomena [1,2].

The determination of thermodynamic data is thus still of high relevance and marks a key discipline in Engineering Research [3] due to ongoing process intensification, for the usage of new compounds or for the design of all sorts of novel apparatuses [4–6]. Thermodynamics per se can be defined as being “the study of energy, including the conversion of energy from one into another and the effects that adding or removing energy have on a system” [7,8]. In thermodynamics a variety of properties are regarded, that can be differentiated by being either intensive, meaning that the property’s magnitude is independent of a system’s mass, or extensive with the opposite dependency of the beforementioned [7,8].

In thermodynamic data, which can be also named thermophysical or thermochemical data, the properties depend on the studied system, the present temperature and pressure conditions, and possibly on the system’s composition. A system can hereby be a single pure compound (more clearly: pure substance), or a mixture consisting of two or more compounds.

There is especially a lack of thermodynamic data regarding novel fuels, also referred to as e-fuels, that could be synthesized for example by power-to-X production cycles using renewable energy sources. Those fuels are for example so-called Poly(oxyethylene) Dimethyl Ethers or alcohols such as 1-octanol. The lack of data is because these substances were not in the focus of researchers providing especially thermodynamic data at elevated temperature and pressure conditions, which is the aim of this thesis.

During my scientific employment at the Institute of Thermal-, Environmental- and Resources Process Engineering (ITUN) of the Technische Universität Bergakademie

Freiberg (TU BAF), thermodynamic data were determined by the use of a microfluidic device. Microfluidics as an alone-standing discipline, mark the carrying out of processes in miniaturized systems [9,10], such as capillaries or channels with diameters of typically $d < 10^{-3}\text{m}$. There are several advantages arising from the use of microcapillaries compared to pipes and cells of larger volumes. One of those advantages lies for instance in the easy-to-achieve optical accessibility, which is especially important for the here carried out optical and spectroscopic analysis.

By using Raman spectroscopy with self-engineered probe heads, compositions at both unsaturated and saturated conditions are measured *in situ*. Thereby it is possible to measure accurately the vapor-liquid equilibria of fuel/air systems at elevated pressure and temperature conditions, since datasets are here especially scarce in the archival literature. Precise calibration measurements and spectral evaluation procedures were applied, while for the latter also new methods were developed in order to resolve saturated vapor phase spectra that are interfered with by the signal of a liquid film.

By photo-optical measurements it was moreover possible to determine vapor pressures of Poly(oxymethylene) Dimethyl Ethers (OME₃ and OME₄) at temperatures above the atmospheric boiling point and closely up to the critical temperature, which also marked the first time that vapor pressure data were determined by the here used microcapillary setup. Thermodynamic correlations and models, such as the Peng Robinson Equation of State (PR-EoS) or the Perturbed Chain Statistical Associating Fluid Theory (PC-SAFT) have been furthermore used within this thesis, in order to derive related properties such as the latent heat of vaporization or Henry's law coefficients.

By connecting both photo-optical and Raman-spectroscopic measurements, it was an additional task of this thesis to determine vapor and liquid phase mixture densities. The applied experimental procedure is therefore validated for future use.

2 State of the art

This section gives an overview of the archival literature and discusses the motivation for the performed experimental studies.

2.1 Vapor pressure measurements

For modeling purposes, precise functions of vapor pressure and latent heat of vaporization are relevant, especially over the full temperature range up to the compound's critical temperature [11,12]. A large majority of vapor pressure datasets however were measured below a compound's atmospheric boiling point temperature and logically no compounds were in the focus that are now being studied for their potential use as an e-fuel.

Experimental setups that allow the vapor pressure measurements for pressures exceeding one atmosphere have been relatively early developed [13,14]. They are in principle based on a cell that resists high pressure and temperature conditions. Especially in the time of the 1960s to 1990s, the vapor pressures and critical properties of a variety of organic compounds were precisely studied. For example, the works of Ambrose and Sprake [15,16] or Radosz, Lydersen and Tsochev [17,18] can be named hereby. These apparatuses however use relatively large amounts of substance, the experiments can result in a potentially long experimental time and general setup handling might be difficult. As a consequence, a measurement procedure employing a microfluidic setup was developed, with which the vapor pressures of pure compounds at elevated temperatures can be determined and the experimental time and material consumption are also lower compared to cells. The compound class of so-called Poly(oxymethylene) dimethyl ethers (OME_n ; $\text{H}_3\text{C} - \text{O} - (\text{CH}_2\text{O})_n - \text{CH}_3$) is regarded. These compounds have drawn attention in recent years for their possible utilization as non-fossil-based fuels in diesel engines [19–21], which is due to the potential integration into an electrofuel (e-fuel) production cycle [22–26] and desirable diesel characteristics, such as high cetane numbers and soot-free combustion behavior [27–29]. In this work, the polymers with a repeating unit of 3 and 4 (OME_3 , OME_4) are studied. For the usage of OME_n as a diesel fuel, it is of utmost importance to gain knowledge about the fuel behavior within the following micro processes: injection, spray formation, fuel/air-mixture formation, ignition and combustion [30,31].

The only available dataset of vapor pressures was provided by Richard H. Boyd [32], who measured the vapor pressures of these and other Poly(oxymethylene) Dimethyl Ethers, up to their atmospheric boiling temperatures. There is furthermore a force field simulation carried out by Kulkarni et al.[33], by which the vapor pressures of OME_3 were predicted up

to a temperature of 543.06 K and in the case of OME₄ up to 582.21 K. It is however relevant to state that the only vapor pressure dataset that Kulkarni et al.[33] considered for the development of their force field is the one of Boyd. The experimental acquisition of saturated vapor pressure data, especially for temperatures that exceed the atmospheric boiling temperature of the compound, can thus provide the necessary reliable data for the earlier mentioned modeling tasks. By using a full temperature range vapor pressure correlation, it is furthermore possible to derive therefrom the latent heat of vaporization.

2.2 VLE measurements

Staying in the context of a fuel injection process, the knowledge of vapor-liquid equilibria (VLE) is furthermore relevant regarding the fuel/air phase boundary [34,35]. By accurate VLE data, one can relate the amount of air that is dissolving into the fuel-rich liquid droplet and vice versa the amount of fuel that is evaporated into the air-rich vapor phase. For the determination of elevated pressure and temperature VLE data, mainly pressure cell setups can be found in the literature that are technically relatively similar compared to the ones mentioned before for vapor pressure data measurements. The same difficulties or disadvantages count for those devices. Publications reporting high pressure and high temperature VLE data of systems including a fuel and oxygen are however especially scarce, due to the potentially ignitable mixture compositions during experimentation. By *in situ* Raman spectroscopy and by microfluidics using only small sample volumes, the personal risk and the potential material damage that an explosion would cause is significantly reduced compared to high pressure cells.

Alcohols such as ethanol and 1-octanol are potential drop-in fuels for fossil-based or renewable diesel [36–51]. This is mainly due to the possible reduction of particulate matter, due to the potentially lowered soot formation during alcohol combustion [51–53], and for their possible synthesis by either biomass conversion [54,55] (in the case of ethanol) or by power-to-X [56,57] production cycles. The latter counts also for higher n-alkanes, which are known as petroleum or fuel ingredients. N-alkanes can be synthesized following the routes of Fischer Tropsch chemistry [58].

Regarding systems that consist of a fuel (here: ethanol, 1-octanol, n-alkane) and a gas (N₂, O₂, synthetic air) there are only scarce data in the archival literature, especially at engine-relevant pressures in the range of $p = \{1.5 \text{ to } 9\}$ MPa and for high temperatures.

For the ethanol/N₂ system the only available dataset at elevated pressure, besides atmospheric solubility data, is from Fischer and Wilken [59]. Klima and Braeuer were

therefore measuring VLE for this specific system [60]. There are furthermore solubility data expressed by Henry coefficients, both for the system ethanol/N₂ and ethanol/O₂, e.g. of Schnabel et al. [61] or Malviya and Vrabec [62].

VLE data of the binary systems 1-octanol/N₂, as well as 1-octanol/O₂ are available at atmospheric conditions for both binary systems [63,64], while data at elevated pressure have been only reported for the binary system 1-octanol/N₂ by Weng et al. [65] and Lu et al. [66]. Lu et al. [66] published liquid phase compositions only, which however deviate from the comparable data of Weng et al. [65] (see results section).[67]

Regarding n-alkane/N₂ systems, VLE are investigated with the n-alkane being either n-tridecane, n-pentadecane, n-hexadecane or n-heptadecane. Unlike for the systems of N₂ with n-tridecane, n-pentadecane or n-heptadecane, for which VLE data at the here discussed conditions are not available, datasets of Lin et al.[68], Sultanov et al.[69] and Rowane et al.[34] are available in the archival literature for the binary system of n-hexadecane/N₂. There are further publications of Llave and Chung[70], Gao et al.[71], García-Córdova et al.[72] and D’Avila et al.[73] that report VLE data of the binary system n-dodecane/N₂, as well as of de Leeuw et al.[74] reporting only liquid phase (*px*) data for the binary system n-tetradecane/N₂. The data that can be regarded for validation are summarized in detail by Table 1. The type denotes hereby either saturated liquid and vapor phase data (*pxy*), saturated liquid phase data only (*px*) or Henry law coefficients *H*.

Table 1: Data that were regarded for validation of the VLE measurements

Binary system	<i>p</i> / MPa	<i>T</i> / K	type	Reference
n-hexadecane/N ₂	2 – 25.5	463 – 703	<i>pxy</i>	Lin et al. [68]
n-hexadecane/N ₂	2 – 25.5	423 – 623	<i>pxy</i>	Sultanov et al. [69]
n-hexadecane/N ₂	10.9 – 127.6	323 – 536	<i>px</i>	Rowane et al.[34]
1-octanol/ N ₂	1 – 10	333.15 – 453.15	<i>pxy</i>	Weng et al. [65]
1-octanol/ N ₂	–	333.15 – 453.15	<i>H</i>	Weng et al. [65]
1-octanol/ N ₂	2.495 – 8.369	273.27 – 317.92	<i>px</i>	Lu et al.[66]
ethanol/O ₂	–	273.15 – 473.15	<i>H</i>	Malviya and Vrabec[62]
ethanol/O ₂	–	273.15 – 498.15	<i>H</i>	Schnabel et al.[61]

2.2.1 Spectroscopic determination of fluid phase equilibria

Methods for the determination of fluid phase equilibria can be very generally classified as in a review by Deiters and Schneider [75] published in 1986, defining different types of experimental setups that have been developed in order to determine the composition of a fluid phase equilibrium. Those are classified as follows:

- *synthetic methods*, where the initial (respectively global) composition of the system is precisely known. The temperature and the pressure are adjusted so that the formation of one homogeneous phase can be observed. During an experimental run the pressure or the temperature is varied until the formation of a new phase is observed. The pressure, the temperature and the known mole fraction mark thus a phase equilibrium point.

- *analytical methods*, where the initial composition is unknown and the equilibrium composition can be determined by sampling or *in situ* measurements of the two or more phases.

Especially the preparation of the initial mixture for the synthetic method, as well as sampling in the case of the analytical method, might be prone to error. As originally stated by Schwedt [76] and later cited in a review by Peper and Dohrn [77] “sampling is the step where the highest error might occur”. Peper and Dohrn further point out that working steps of which sampling is composed of, such as depressurization, might disturb the equilibrium and can thus cause an erroneous determination of the equilibrium compositions if not handled carefully. It can be derived therefrom that Spectroscopy which allows *in situ* applications can be advantageous to several sampling-dependent techniques, especially at temperatures and pressures that differ from ambient conditions.

The first characterizations of fluid phase equilibria by spectroscopy were the publications of Swaid et al. and Nickel et al. [78,79], with both works originating from the same research group. In these publications, several systems containing carbon dioxide are studied by *in situ* near-infrared (NIR)-absorption spectroscopy. Schneider was utilizing in consecutive works both, *in situ* NIR- and *in situ* ultraviolet and visible (UV-VIS)-absorption spectroscopy for higher organic molecules and colorants until the early 2000s.

In the case of *in situ* Raman spectroscopy it took 12 years after the pioneering publication of Diller and Chang [80] in 1980, who reported the quantitative analytical analysis of unsaturated natural gas mixtures at elevated pressure, when the method was used by Kaiser et al. for the determination of VLE [81]. The reader might generally wonder, why the earlier mentioned, conventional measurement techniques still exist, if the preparation (synthetic method) or sampling (analytical method) can be avoided with remotely working spectroscopic techniques. The reason lies in the precise calibration that is necessary before a spectroscopic method can qualify for the quantification of fluid phase equilibria of unknown mixtures. Uncertainties in the calibration procedure can thus cause errors that might be similar or larger compared to mixture preparation (synthetic method) or sampling (analytical method).

2.2.2 Raman spectroscopy coupled microfluidic devices

Microfluidic devices for the determination of thermodynamic data are in general still relatively novel, especially when they are coupled with Raman spectroscopy. Comparable microfluidic setups that are equipped with an *in situ* Raman spectroscopy unit for the determination of fluid phase equilibria (such as LLE and VLE) are relatively scarce in literature. Setups were recently used by Liebergesell et al. [82,83], Liu et al. [84] or Wang et al. [85–87] for the determination of VLE respectively solubility data, as well as by Thien et al. [88,89] and Kasterke et al. [90] for measurements of liquid-liquid equilibria (LLE). The first study carried out with an *in situ* Raman spectroscopy coupled microfluidic device by the research group of this thesis' supervisor, dates back to the years 2014 and 2015. Luther et al. [91,92] determined the VLE of the ethanol/ CO_2 system at elevated pressure conditions. Hereby the Raman signal is taken selectively from either the saturated vapor or the saturated liquid phase. The light barrier technology with which the phase-selective measurement is realized was later on improved by Klima and Braeuer [60] with the introduction of a pulsed fiber switch. This principle is in detail explained in the sections that deal with the experimental setup since the light barrier system is unchanged since then. Klima and Braeuer [60] introduced furthermore an approach to correct the spectra of the saturated vapor phase from the signal contribution that stems from a liquid film that surrounds the vapor slugs / bubbles (see details in 4.2.2). It was also applied in this thesis for the VLE study of ethanol/ N_2/O_2 systems (see Figure 1). Hereby the phase-dependency of the OH-stretching vibration band is exploited. While the OH-stretching vibration band is typically broad in spectra of the liquid phase, it is a sharp peak in spectra of the vapor phase. This is a direct result of the hydrogen bonding of ethanol molecules in the liquid state.

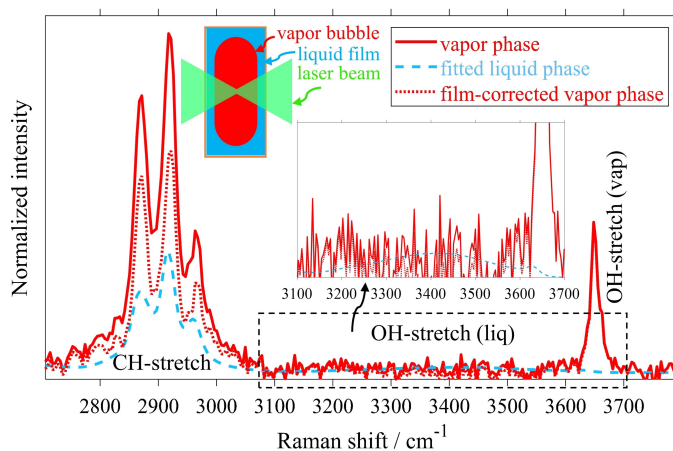


Figure 1: Correction of liquid film contribution for the system ethanol/ N_2/O_2 at $T = 373 \text{ K}$ and $p = 6.5 \text{ MPa}$ [93]

By this method, the corresponding (same p and T) saturated liquid phase spectrum $S_{OH-str-liq}^{liq,s}$ is fitted by iterating the fit parameter t in least-squares sense, to the spectral range inside the film-influenced saturated vapor phase spectrum $S_{OH-str-liq}^{vap,s,film}$ where the liquid OH-stretch vibration band would appear.

$$S_{OH-str-liq}^{vap,s,film} = t \cdot S_{OH-str-liq}^{liq,s} \quad (1)$$

As it can be seen in Figure 1 the signal contribution of the liquid film can thus be quantified in the relevant range of the CH-stretch vibration. The corrected saturated vapor phase spectrum $S_{CH-str}^{vap,s}$ (red dotted lines) can thus be obtained by the subtraction of the film-influenced vapor phase spectrum $S_{CH-str}^{vap,s,film}$ (red lines) and the fitted saturated liquid phase spectrum $t \cdot S_{CH-str}^{vap,s}$ (blue dashed lines).

$$S_{CH-str}^{vap,s} = S_{CH-str}^{vap,s,film} - t \cdot S_{CH-str}^{liq,s} \quad (2)$$

The other spectral parts where the N₂- and O₂-stretch vibrations appear do not have to be corrected, since the film-influence is there only marginal (counts also for the other systems studied). In general, this film-correction method can however be regarded critically, since the OH-stretching band causes a poorer signal compared to the CH-stretching vibration band for instance. This causes a fit in a spectral regime where the signal-to-noise ratio is relatively low (compare spectral noise in the OH-stretching vibration band regime in Figure 1). It is furthermore clear that this approach is only applicable to OH-group containing molecules, such as alcohols, water or ammonia. In the case of n-alcohols however, the signal of the OH-stretch vibration band becomes weaker with increasing carbon chain length. Due to the given reasons, other methods for the correction of the film-influence were developed and introduced that are not any longer dependent on the OH-group.

2.3 Mixture density measurements

The accurate determination of the saturated mixture densities marks a challenging task due to the difficulties that arise from the precise volume determination. Hübner and Minceva [94,95] introduced recently a microfluidic platform that allows the determination of liquid-liquid equilibria (LLE) compositions, as well as the saturated mixture densities of the ternary system water/acetone/toluene. The densities are determined by a micro density meter. This

experimental approach of Hübner and Minceva is however based on a parallel flow pattern, which is formed by two liquid phases in a rectangular capillary. Since such a microfluidic flow pattern cannot be obtained for an asymmetric system such as ethanol/CO₂ and since the microfluidic setup is limited in pressure and temperature conditions, we developed the here introduced experimental approach (compare section 4.2.3). The experimentally obtained saturated densities can be compared to available literature data listed in Table 2. Unsaturated densities or saturated densities at low temperatures were not regarded.

Table 2: Available literature data reporting saturated liquid and vapor phase densities for binary system ethanol/CO₂

p / MPa	T / K	type	Reference
1 – 8	291 – 313	$\rho^{s,liq}, \rho^{s,vap}$	Chang et al. [96,97]
1 – 6	303, 328	$\rho^{s,liq}, \rho^{s,vap}$	Kariznovi et al. [98]
3.3 – 8.1	291 – 323	$\rho^{s,liq}$	Stievano and Elvassore [99]
0.1 – 11.2	313 – 343	$\rho^{s,liq}, \rho^{s,vap}$	Seifried and Temelli [100]
0.6 – 9.4	313, 328	$\rho^{s,liq}, \rho^{s,vap}$	Tsivintzelis et al. [101]
0.8 - 8	291 - 313	$\rho^{s,liq}, \rho^{s,vap}$	Day et al. [102]
1.5 – 7.8	308	$\rho^{s,liq}, \rho^{s,vap}$	Tanaka and Kato [103]

In this work a bubble is assumed to consist of two hemispherical caps and a middle cylindrical part. This assumption was also chosen in several other works in the field of microfluidics [104–109] for systems such as water/CO₂, water/air or monoethanolamine/CO₂.

3 Application oriented fundamentals

In this chapter, the fundamentals that are necessary for the understanding of this thesis' content are covered. These are separated into thermodynamic fundamentals, microfluidics and Raman spectroscopy.

3.1 Thermodynamic fundamentals

3.1.1 pVT -behavior and equilibrium conditions

The relation between the state variables pressure p , temperature T and volume V (or its intensive quantities v_m and v) of a pure compound can be visualized in pVT -diagrams, indicating different thermodynamic states.

The pVT -diagram, here for a pure compound that does not feature anomaly (for instance carbon dioxide (CO_2)), shows this relation three-dimensionally. Pure substances or mixtures can generally be in solid, liquid, or vapor state of aggregation (phase) or can coexist for constant pVT -conditions in more than one phase at once, a phenomenon known as “phase equilibrium”.

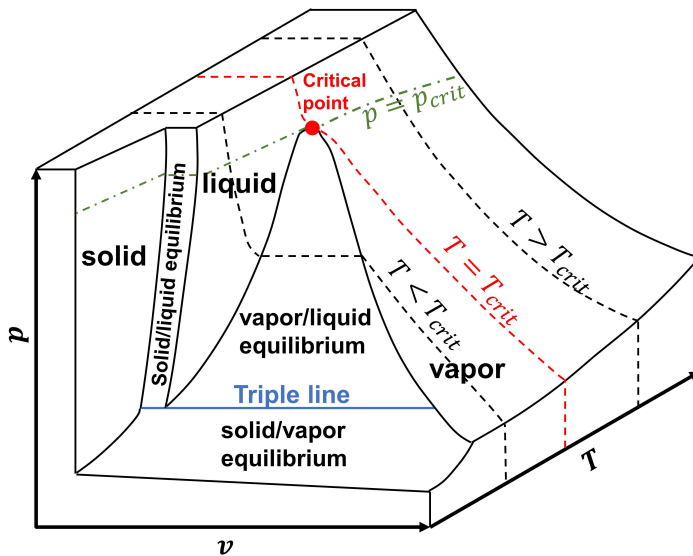


Figure 2: Three-dimensional pVT -diagram of a pure compound without anomaly (own artwork)

While within certain areas two states coexist, such as the vapor-liquid equilibrium (VLE), three states are in equilibrium along the triple line. A pure compound is furthermore supercritical for conditions exceeding the critical temperature T_{crit} and critical pressure p_{crit} . The critical point at the top of the vapor/liquid equilibrium regime is thus on the critical isotherm ($T = T_{crit}$) and the critical isobar ($p = p_{crit}$). From the pVT -diagram of a

pure compound, two major two-dimensional projections can be derived, the pT - and the pv -diagram (see Figure 3). [8,110]

While in the pv -diagram the phase equilibrium regimes can be seen as areas like in the pvT -diagram, those areas are projected on curves in the case of the pT diagram. Since within this thesis fluids and thus no solids are specifically regarded [8], vapor/liquid equilibria of pure substances are in the further considered, while equilibria including the solid state are not. When the vapor and liquid phases are in equilibrium with each other, the terms saturated vapor and saturated liquid are used in order to describe this specific condition (compare labels in Figure 3).

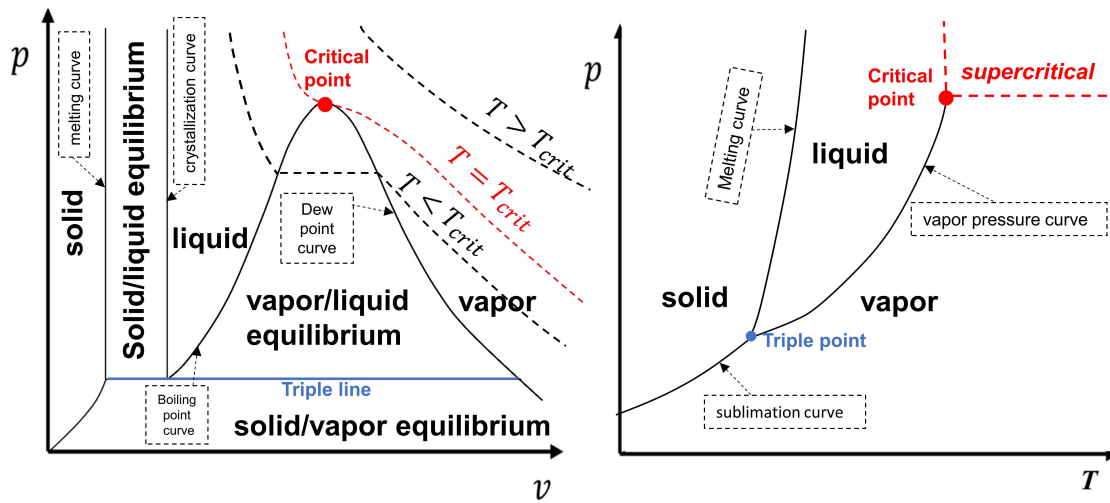


Figure 3: Two-dimensional pv - and pT -projections of a pure compound without anomaly (own artwork); nomenclature for saturated curves from Gmehling et al. [8]

Three equilibrium conditions are necessary in order to define a phase equilibrium (here: VLE), beginning with the chemical equilibrium. It is in principle based on the equivalence of Gibbs energies g that are equal to the chemical potential μ for a pure substance. [8]

$$g^{liq} = g^{vap} \quad (3)$$

When combining the chemical equilibrium condition of eqn. (3) with the residual function of the Gibbs energy given in eqn. (4),

$$(g - g^{id})_{T,p} = RT \ln\left(\frac{f}{p}\right) = RT \ln(\varphi) \quad (4)$$

wherein R is the universal gas constant, f is the fugacity and φ is the fugacity coefficient, one can obtain with eqn. (5) the isofugacity criterion. Eqn. (6) can be further simplified and

in eqn. (7) can be obtained in case a pure compound is regarded. Therein only the fugacity coefficients must be considered.

$$f^{liq} = f^{vap} \quad (5)$$

$$p\varphi_i^{liq} = p\varphi_i^{vap} \quad (6)$$

$$\varphi_i^{liq} = \varphi_i^{vap} \quad (7)$$

A phase equilibrium is furthermore defined by its thermal (considering T) and mechanical equilibrium (considering p) between the here regarded vapor and liquid phases. [8]

$$T^{liq} = T^{vap} \quad (8)$$

$$p^{liq} = p^{vap} \quad (9)$$

For a system consisting of more than one compound i (e. g. binary or ternary systems or generally speaking: a mixture), phase equilibria are not only described by the state variables p, v, T , but also by the composition. Composition dependent phase diagrams for mixtures are therefore introduced at a later point (compare 3.1.5). In this thesis z denotes a phase-independent mole fraction (see eqn. (10); relating molar amounts of substance n_i), while y and x refer specifically to the vapor phase and the liquid phase.

$$z = \frac{n_i}{\sum_{i=1}^{nc} n_i} \quad (10)$$

The isofugacity criterion introduced with eqn. (5) to (7) for pure compounds, is as follows provided for mixtures by eqn. (11).

$$x_i\varphi_i^{liq} = y_i\varphi_i^{vap} \quad (11)$$

Mixtures can moreover coexist in equilibria between two phases of the same state, e. g. liquid-liquid equilibria or vapor-liquid-liquid equilibria. In this thesis however, the vapor-liquid equilibria (VLE) of pure compounds, as well as of mixtures are of relevance.

Eqn. (7) and (11) which are also known by the expression $\varphi - \varphi$ approach, are especially of relevance for in this work applied equations of state (EoS) modeling (see following section). [8,111]

3.1.2 Equations of state (EoS)

Equations of state (abbreviation: EoS) are thermodynamic models that relate the state variables p, T and v with each other. Since the introduction of the first EoS in 1873 by the later Nobel prize winner van der Waals [112,113], a large number of models were introduced, as well as extensions and modifications of those [114]. The majority of these models are cubic in respect to the molar volume v (see relation to density by eqn. (12)) or the compressibility factor Z (see eqn. (13)), just like the van der Waals equation.

$$\rho = \frac{M}{v} \quad (12)$$

$$Z = \frac{pv}{RT} \quad (13)$$

The cubic character of these EoS results for instance in obtaining three solutions for the saturated molar volume v^s , as illustrated in Figure 4 for CO_2 at $T = 278.15\text{K}$, whereas the isotherm predicted by the ideal gas law does not approach a liquid phase regime.

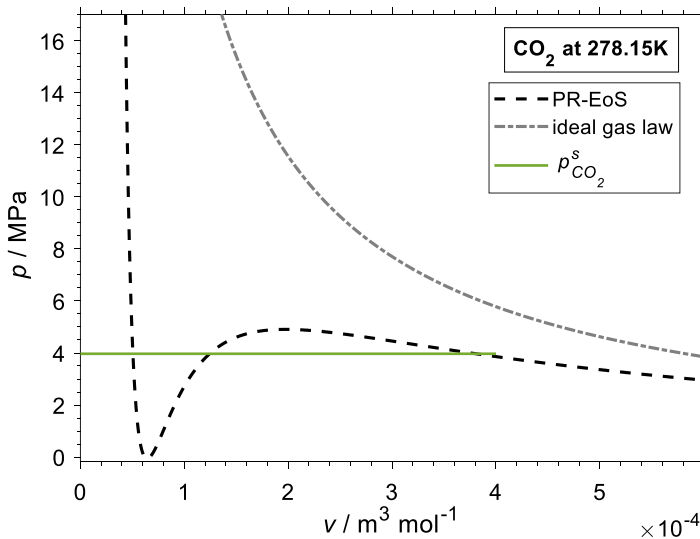


Figure 4: pv -diagram showing the isotherms of CO_2 at 278.15 K predicted by the PR-EoS (passing through the vapor phase, vapor-liquid two phase region and liquid phase) and by the ideal gas law

One of the most successful cubic EoS was introduced by Peng and Robinson [115] in its original form in the year 1976, which is since then of high relevance for all sorts of fluid processes, especially due to its capability in modeling fluid phase equilibria.

The equation that is abbreviated PR-EoS has been used for modeling in the publications [67,93,116] that led to this thesis and is expressed in respect to the pressure p as,

$$p = \frac{R \cdot T}{v - b} - \frac{a}{v \cdot (v + b) + b \cdot (v - b)} \quad (14)$$

with a and b being the PR-EoS parameters. These parameters are in this work calculated according to the van der Waals one fluid mixture rule (vdW1).

$$a = \sum_{i=1}^{nc} \sum_{j=1}^{nc} a_{ij} \cdot z_i \cdot z_j; b = \sum_{i=1}^{nc} b_{ii} \cdot z_i \quad (15)$$

$$a_{ij} = \sqrt{a_{ii} a_{jj}} \cdot (1 - k_{ij}^{PR}) \quad (16)$$

Therein k_{ij}^{PR} is a binary interaction coefficient between compound i and compound j . The binary interaction coefficient can be regarded as both, temperature-independent and temperature-dependent. Regarding the latter, a group contribution model introduced by Privat et al. [117] as well as Jaubert and Mutelet [118], which is known under the abbreviation PPR78, is employed for in this work studied n-alkane/N₂ systems, while in the other VLE publications (ethanol/N₂/O₂ and 1-octanol/N₂/O₂) k_{ij}^{PR} is a self-adjusted fit parameter. The PR-EoS pure-compound parameters are obtained from the critical pressure p_{crit} and temperature T_{crit} by eqn. (17) and (18).

$$a_{ii} = a_{crit,i} \cdot \alpha_i = 0.457235 \frac{R^2 T_{crit,i}^2}{p_{crit,i}} \cdot \alpha_i \quad (17)$$

$$b_{ii} = 0.077796 \frac{R T_{crit,i}}{p_{crit,i}} \quad (18)$$

Therein α_i is calculated by the original functions from 1976 (see eqn. (19); for publications [67,93,116]), except for the VLE study of the n-alkane/N₂ study, wherein the PPR78 is applied that uses a modified function for longer chain molecules introduced by Peng and Robinson in 1978 [119] (see eqn. (20); for publication: [120]).

$$\alpha_i = [(1 + (0.37464 + 1.54226\omega_i - 0.26992\omega_i^2))(1 - T_{r,i}^{0.5})]^2 \quad (19)$$

$$\alpha_i = [(1 + (0.379642 + 1.48503\omega_i - 0.164423\omega_i^2 + 0.016666\omega_i^3))(1 - T_{r,i}^{0.5})]^2; \quad (20)$$

for $\omega_i > 0.491$; for $\omega_i < 0.491$ see eqn. before

In the α -functions T_r is the reduced temperature ($T_r = T \cdot T_{crit}^{-1}$). If a pure compound is considered, as in the work regarding the OME_n [116], eqn. (15) and (16) simplify to $a = a_{ii}$ and $b = b_{ii}$. Another group of EoS is formed by models that consider the statistical associating fluid theory, in short: SAFT. Here the Perturbed Chain variation (PC-SAFT) is used which is expressed in terms of the compressibility factor,

$$Z = 1 + Z^{hc} + Z^{disp} + Z^{assoc} \quad (21)$$

by the sum of different contributions according to Gross and Sadowski [121,122]. In eqn. (21) Z^{hc} denotes the hard-chain term, Z^{disp} the dispersion term and Z^{assoc} the contribution due to association. For non-associating molecules (n-alkanes, N₂ or O₂) the associating term becomes $Z^{assoc} = 0$, since those molecules are solely defined by the number of segments per chain m , the segment diameter σ and the depth of the pair potential ε/k_b , with k_b being the Boltzmann constant [67]. According to the 2B scheme defined by Huang and Radosz [123], two further pure-compound parameters are necessary for the associating interactions of alcohols, such as 1-octanol [67].

These are ε^{AiBi}/k_b as the association energy and κ^{AiBi} as the effective association volume between the association sites (A of molecule i and B of molecule i). The mixing rules are provided by eqn. (22) and (23), with k_{ij}^{PCS} being a temperature-dependent or temperature-independent binary interaction coefficient (analog to the PR-EoS). Logically, mixing rules do not have to be applied in case a pure compound is regarded.

$$\sigma_{ij} = \frac{1}{2}(\sigma_i + \sigma_j) \quad (22)$$

$$\varepsilon_{ij} = (\varepsilon_i \cdot \varepsilon_j)^{0.5} \cdot (1 - k_{ij}^{PCS}) \quad (23)$$

Methods on how to fulfill the isofugacity criterion, more detailed PC-SAFT equations for the calculations of the different contributions, as well as more detailed equations for obtaining the fugacity coefficient, are here for simplicity not further provided.

Besides the PR-EoS and PC-SAFT, the Wagner and Span EoS [124] is applied in this work, especially for the density calculations of carbon dioxide (CO₂). The data can be however directly extracted from the NIST pure fluids database [125] and therefore no equations are here given.

While both PC-SAFT and the PR-EoS can provide accurate results for the molar volume of the unsaturated and saturated vapor phase, large errors can result from predicting the saturated molar volume of the liquid phase v^{liq} , especially with a cubic equation like the PR-EoS. Even if the PR-EoS is extended by a P eneloux-style volume translation [126], the predicted liquid densities might be still inappropriate. For this specific reason, density correlations are in most cases a good choice to reproduce accurately liquid phase densities at least for pure compounds.

Equations of state can be also considered for the calculation of Henry’s law coefficients, which describe the temperature-dependent solubility of a considerable low-density compound j (here e.g.: N₂/O₂) in a saturated liquid phase that is rich in the high-density compound i (here e.g.: 1-octanol, ethanol or n-alkane). The Henry’s law coefficient is calculated as follows,

$$H_{j-i} = \lim_{\substack{x_i \rightarrow 1 \\ p \rightarrow p_i^s}} \left[\frac{f_j^{s,vap}}{1 - x_i} \right] \quad (24)$$

wherein x_i denotes the mole fraction of i in the saturated liquid phase, p_i^s the saturated vapor pressure of compound i and $f_j^{s,vap}$ the fugacity of compound j (N₂/O₂) in the saturated vapor phase, that can be computed by an EoS. According to Gmehling et al., “Henry’s law is exactly valid only for the case where the partial pressure is identical to the vapor pressure of the solvent” [8]. The application of the Henry constant should thus be restricted only to low concentrations of the solute j , but is however also applied for conditions diverging from the beforementioned.

3.1.3 Density correlations

Various approaches exist for the calculation of liquid phase densities, respectively liquid phase molar volumes, at both, saturated and unsaturated conditions. With the general relationship between molar volume and density already introduced in eqn. (12), most correlations regard the liquid density ρ^{liq} instead of the liquid molar volume v^{liq} . An

exception is the Rackett Spencer and Danner equation for liquids at saturation [127–130] that in its simplified and recently used form [8,26] is expressed by eqn. (25),

$$v^{s,liq} = \frac{L_0}{L_1^{1+(1-T_r)L_2}} \cdot 10^{-6} \text{ m}^3 \text{ mol}^{-1} \quad (25)$$

wherein L_0 to L_2 are adjustable parameters and T_r is the reduced temperature. Its applicability to polar compounds such as ethers, esters and alcohols, was discussed in detail by Spencer and Adler [129]. Another important liquid density correlation is the Tait equation [8], which covers liquids at both saturated and unsaturated state and allows furthermore the application to mixtures by mixing rules (not regarded however in this thesis). The Tait equation is written as follows,

$$\rho(T, p, \vec{c}, \vec{b}) = \frac{\rho(T, p_{ref}(T))}{1 - C(T, \vec{c}) \ln \left[\frac{B(T, \vec{b}) + p}{B(T, \vec{b}) + p_{ref}(T)} \right]} \quad (26)$$

with $B(T, \vec{b})$ and $C(T, \vec{c})$ being defined as,

$$C(T, \vec{c}) = \sum_{i=0}^{N_C} c_i \left[\frac{T - T_0}{100} \right]^i; \quad \vec{c} = \{c_i\} = \{c_0, \dots, c_{N_C}\} \quad (27)$$

$$B(T, \vec{b}) = \sum_{i=0}^{N_B} b_i \left[\frac{T - T_0}{100} \right]^i; \quad \vec{b} = \{b_i\} = \{b_0, \dots, b_{N_B}\} \quad (28)$$

wherein c_i , b_i and T_0 (with condition $C(T_0) = c_0$ and $B(T_0) = b_0$) are adjustable parameters and with $p_{ref}(T) = 0.1013 \text{ MPa}$ (for $T < T^b$) or $p_{ref}(T) = p^s$ (for $T > T^b$). Therein b_i should not be mistaken for the earlier introduced PR-EoS parameter.

The vapor phase density (at both unsaturated and saturated state) of a pure compound or a binary system can be well described even for relatively polar compounds (e. g. alcohols) by a cubic EoS, such as the PR-EoS. There are however correlations, such as the one described by Dillon and Penoncello for the saturated vapor phase density of ethanol. [131]

3.1.4 Clapeyron equation and vapor pressure correlations

The vapor pressure curve of pure compounds ending on the critical point, as shown in the pT diagram in the right part of Figure 3, can be expressed by the equation of Clapeyron,

$$\Delta_{vap}h = (v^{s,vap} - v^{s,liq}) \cdot \frac{dp^s}{dT} \cdot T \quad (29)$$

which relates the latent heat of vaporization $\Delta_{vap}h$, with the saturated molar volumes of the vapor and liquid phases $v^{s,vap}$ and $v^{s,liq}$, as well as with temperature T and saturated vapor pressure p^s [8]. Clausius introduced the assumptions to neglect $v^{s,liq}$, due to $v^{s,vap} \gg v^{s,liq}$, and further the description of the saturated vapor molar volume by the ideal gas law. These simplifications that lead to eqn. (30),

$$\Delta_{vap}h = \frac{RT^2}{p^s} \cdot \frac{dp^s}{dT} \quad (30)$$

are well suitable for conditions up to the atmospheric boiling point of a pure compound [132,133], but can lead to errors for temperatures and pressures above. For conditions exceeding the atmospheric boiling point and for the case that associating compounds are regarded, the use of eqn. (29) is recommended [8]. For the computation of $\Delta_{vap}h(T)$, both $v^{s,vap}$ and $v^{s,liq}$ have to be accurately described. While the latter can be expressed by a density correlation, $v^{s,vap}$ can be computed by an EoS. The slope of the vapor pressure curve can be either obtained by an EoS, or by a vapor pressure correlation, such as the extended Antoine equation that is provided as follows.

$$\ln\left(\frac{p^s}{p_0}\right) = L_0 + \frac{L_1}{\frac{T}{T_0} + L_2} + L_3 \cdot \frac{T}{T_0} + L_4 \cdot \ln\left(\frac{T}{T_0}\right) + L_5 \cdot \left(\frac{T}{T_0}\right)^{L_6} \quad (31)$$

The temperature T has therein the unit K and the pressure p is given in bar. The reference conditions are $p_0 = 1$ bar and $T_0 = 1$ K and the parameters L_0 to L_6 are adjustable. There are several other vapor pressure functions, such as the Tchebychev polynomial correlation or the Wagner correlation. The latter is especially interesting since it is dependent on the critical point of the regarded pure compound (see eqn. (32)). [8]

$$\ln\left(\frac{p^s}{p_{crit}}\right) = \frac{1}{T_r} \cdot [L_0(1 - T_r) + L_1(1 - T_r)^{1.5} + L_2(1 - T_r)^3 + L_3(1 - T_r)^6] \quad (32)$$

For the calculation of $\Delta_{vap}h$ it has to be taken care of that in the near-critical region the difference of molar volumes and thus the Clapeyron predicted heats of vaporization can be erroneous. As described by Gmehling et al. [8] this inaccuracy can be avoided if the latent heat of vaporization is fitted by the PPDS correlation (see eqn. (33); for $T_r < 0.975$), which can then be extrapolated up to the critical temperature. Therein τ is defined by eqn. (34). [116]

$$\Delta_{vap}h = R \cdot T_{crit} (L_0 \cdot \tau^{\frac{1}{3}} + L_1 \cdot \tau^{\frac{2}{3}} + L_2 \cdot \tau + L_3 \cdot \tau^2 + L_4 \cdot \tau^6) \quad (33)$$

$$\tau = 1 - T_r \quad (34)$$

3.1.5 Vapor-liquid phase diagrams

With the equilibrium conditions described and the relevant equations and correlations given, VLE and their surrounding unsaturated regimes can be presented in phase diagrams that are of relevance in this study. If the pT -diagram of the binary system ethanol/ CO_2 is regarded (see Figure 5), the VLE is located between the saturated vapor pressure curves of the pure compounds as well as the critical locus.

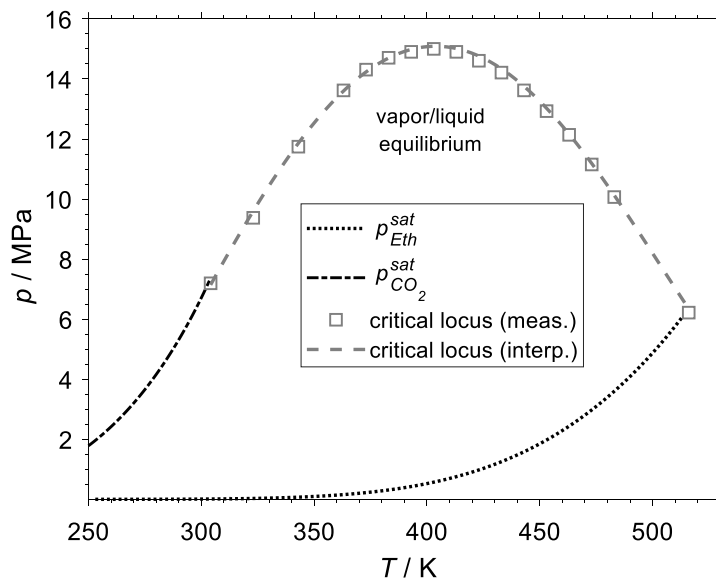


Figure 5: pT -phase envelop of ethanol/ CO_2 binary system; critical loci data from Ziegler and Dorsey [137]; the vapor pressure curves are calculated by the Wagner equation using data of Gmehling et al. [8] (see eqn. (32))

The latter consists of an infinite number of mixture critical pressures that depend not only on temperature, but also on the composition of the binary system. The critical locus curve does thus span the VLE for the ethanol/CO₂ system up to mixture's critical pressures $p_{crit,mix}$ that exceed p_{crit} of the pure compounds by far.

There are however a variety of possibilities regarding the shape of critical loci, due to large differences in mixtures' fluid phase behavior. For the complexity of this specific topic, a classification considering six different types has been provided by van Konynenburg and Scott which is based on the van der Waals EoS [134,135]. Deiters and Kraska carried out a deep review in the field of high pressure fluid phase equilibria [136]. The considerations and classifications regarding the critical locus described therein, are by far more detailed than the relatively simple one provided by van Konynenburg and Scott and are therefore not further discussed at this point.

The above illustrated pT -diagram of the binary system ethanol/CO₂ lacks however information on the composition. The VLE of binary systems are therefore visualized in isothermal pxy - and isobaric Txy -diagrams, that are here obtained by the PR-EoS (see Figure 6), showing the lines of the saturated liquid (bubble point curves) and saturated vapor phase (dew point curves) that define the vapor-liquid equilibrium regime.

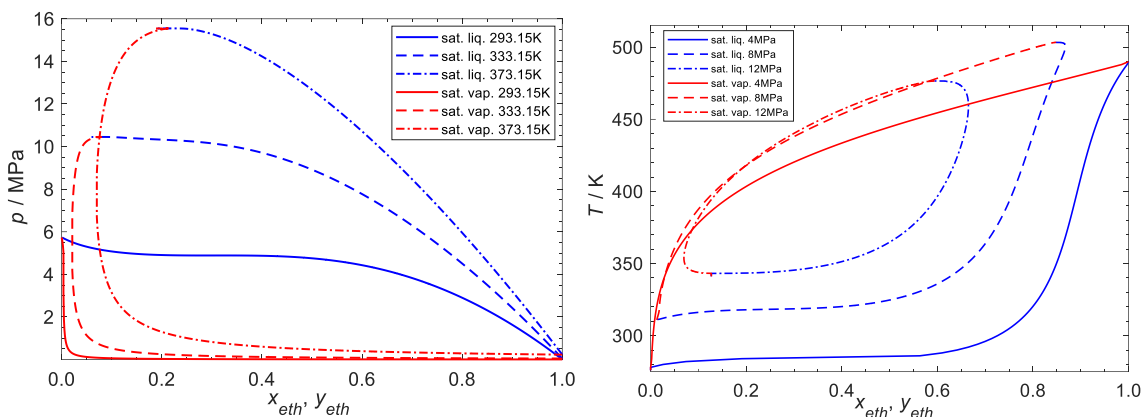


Figure 6: pxy - and Txy -diagram of the binary system ethanol/CO₂; calculated with the PR-EoS

The differences in the shape of the VLE can be explained, if the critical properties of ethanol ($T_{crit} = 514.6\text{K}$; $p_{crit} = 6.23\text{MPa}$) and CO₂ ($T_{crit} = 304.2\text{K}$; $p_{crit} = 7.38\text{MPa}$) are considered. While the isothermal VLE of $T = 293.15\text{K}$ and the isobaric VLE of $p = 4\text{MPa}$ reach both the vertical axis at $z_{eth} = 1$ and $z_{CO_2} = 1$ (equals $z_{eth} = 0$), the same does not count for the other shown VLE. Regarding the pxy -diagram, the VLE of $T = 333.15\text{K}$ and

$T = 373.15\text{K}$ exceed T_{crit,CO_2} and thus the pure compound ($z_{CO_2} = 1$) cannot exist in saturated liquid and vapor state for the given isotherms.

These mixture critical points define the beforementioned critical locus curve (compare Figure 5) and can be also seen in the Txy -diagram for the VLE of $p = 8\text{MPa}$ and $p = 12\text{MPa}$. Since both $p_{crit,eth}$ and p_{crit,CO_2} are below these pressures, both pure compounds can there not exist at saturated state and thus the VLE form and “island-like” shape in the Txy diagram. [8]

As for the illustration of the saturated composition of VLE before, density curves are furthermore of relevance in this thesis and are therefore discussed in the following. If pure compounds are regarded, the density curves of the saturated liquid and vapor phase merge in the critical density ρ_{crit} , which is visualized for ethanol and CO_2 in the left diagram of Figure 7.

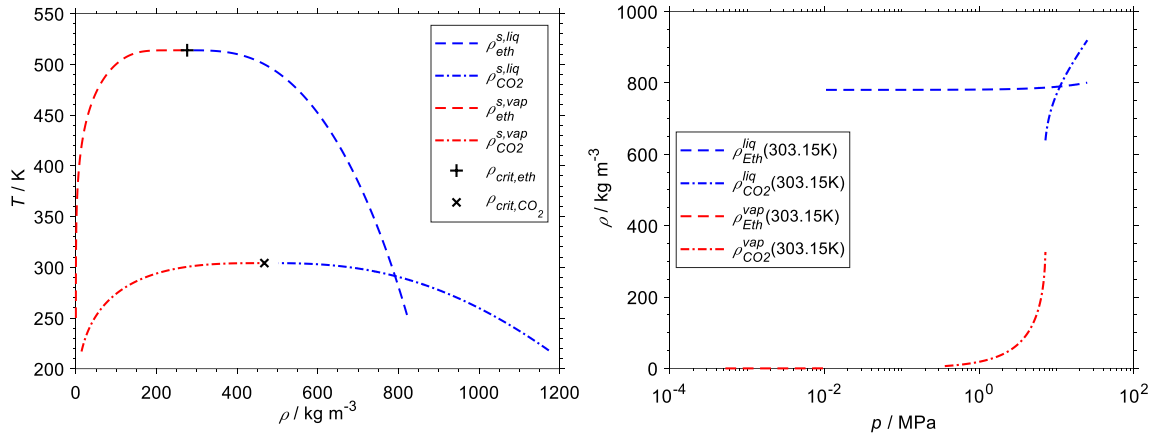


Figure 7: The saturated vapor and liquid phase densities and critical densities of the pure compounds ethanol and CO_2 (left); logarithmic illustration of the unsaturated liquid and vapor phase densities of ethanol and CO_2 along the 303.15K isotherm (right); data for CO_2 obtained by the Wagner and Span EoS; $\rho_{eth}^{s,liq}$ and ρ_{eth}^{liq} by Tait equation, $\rho_{eth}^{s,vap}$ by Dillon and Penoncello and ρ_{eth}^{vap} by PR-EoS

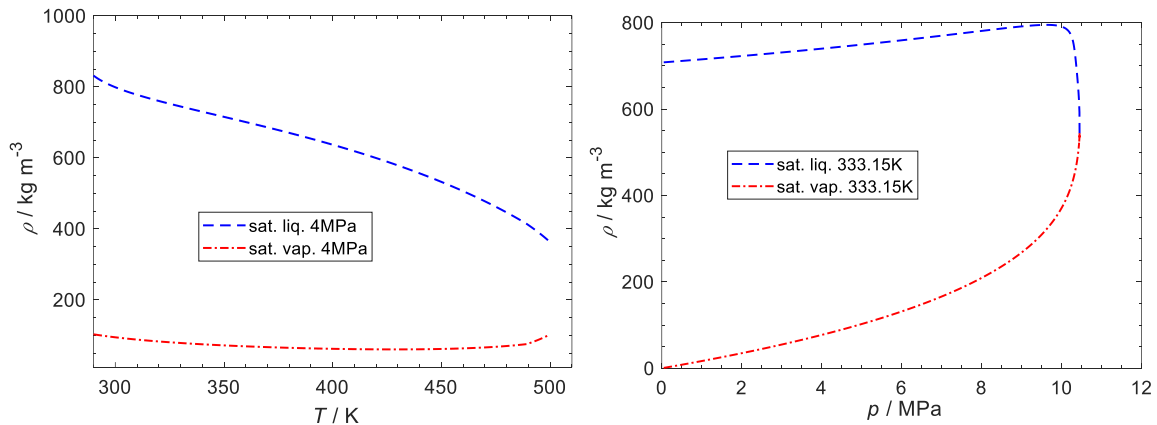


Figure 8: Saturated liquid and vapor phase mixture densities of binary system ethanol/ CO_2 along an isobar of 4MPa (left) and saturated liquid and vapor phase mixture densities along an isotherm of 333.15K (right); compare VLE diagrams in Figure 6; calculated by the PR-EoS (just for illustration)

Densities at unsaturated state, indicating the saturated state and vapor-liquid phase boundary by a strong density increase, are shown for the same compounds in the right logarithmic diagram of Figure 7. In Figure 8 the saturated liquid and vapor phase mixture densities of the binary system ethanol/CO₂ are illustrated. Hereby the earlier shown VLE diagrams can be considered for understanding the trend of the curves.

3.2 Microfluidics

Microfluidics is a relatively novel interdisciplinary field and can be defined according to Whitesides [138] as being “the science and technology of systems that process or manipulate small (10^{-9} to 10^{-18} liters) amounts of fluids, using channels with dimensions of tens to hundreds of micrometers.” Whitesides further points out that for instance, chemical analytical techniques belong to the parental group of microfluidics, as gas phase chromatography (GPC), high pressure liquid chromatography (HPLC) and capillary electrophoresis (CE) are carried out in capillary format. [138]

Microfluidics is of general interest in chemical engineering, due to enhanced heat and mass transfer and interfacial phenomena that cannot be observed usually in macroscale systems. This results from a high surface-to-volume ratio, as well as short characteristic lengths when multiphase flows in microfluidic systems are handled [9,10,139]. For the here used microcapillary setup, a characteristic flow of alternating liquid and vapor segments leads to a fast diffusion-based equilibration of both vapor and liquid phases. This is especially superior compared to pressure cells used for VLE studies where the phase boundary and thus the surface area to volume ratio is by magnitudes smaller compared to the same two-phase system flowing through a microfluidic device.

Even though there are publications on microfluidics that regard dimensionless numbers, such as the Reynolds, Capillary, Bond or Weber numbers, the study when an appropriate segmented flow is formed remains an empirical and mostly qualitative task. One example for this procedure is for instance the creation of a flow regime map, as provided by Martin et al. for the binary system ethanol/CO₂ [140] (see Figure 9). Therein different two-phase flows can be distinguished from each other. The formation tends to be restricted for that specific system on certain pressure and temperature conditions, but depends highly on the capillary diameters, flow rates and the mixing design. For that reason, a more academic consideration of Taylor Flows as such is here not provided.

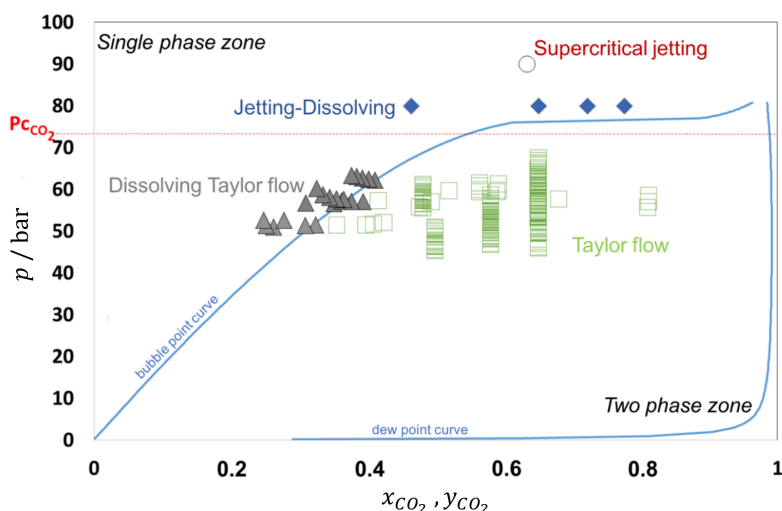


Figure 9: Flow regime map of Martin et al. for binary system of ethanol/CO₂ [140]

3.3 Raman spectroscopy

The exposition of matter to electromagnetic radiation yields a variety of measurable effects. The interactions between light and matter that are relevant for spectroscopic applications are absorption, absorption-emission and scattering. Infrared (IR) spectroscopy and ultraviolet/visible (UV-VIS) absorption spectroscopy share hereby the principle of being based on the absorption of incident light by a molecule, that releases the absorbed energy radiationless. The latter is in contrary to the absorption-emission process, where light is emitted when a molecule is falling back from the vibrational ground level of the excited electronic state to the electronic ground state.

According to Braeuer [141] scattering equals a collision between photon and molecule, which might help to better understand the differences to the other named processes. Scattering is generally different to the absorption-featured processes, since the molecule occupies at no time during the scattering process an excited electronic state. It must be generally distinguished between elastic scattering (also known as Rayleigh scattering), where there is no difference in wavelength between excitation light and scattered light, and inelastic scattering, where the wavelength of the scattered light is different to the wavelength of the excitation light. This is visualized in Figure 10, wherein these beforementioned scattering interaction mechanisms between light and molecules are illustrated. The working principle of Raman spectroscopy lies in the inelastic scattering, which can be also understood as the transfer of energy between the photon and the involved molecules.

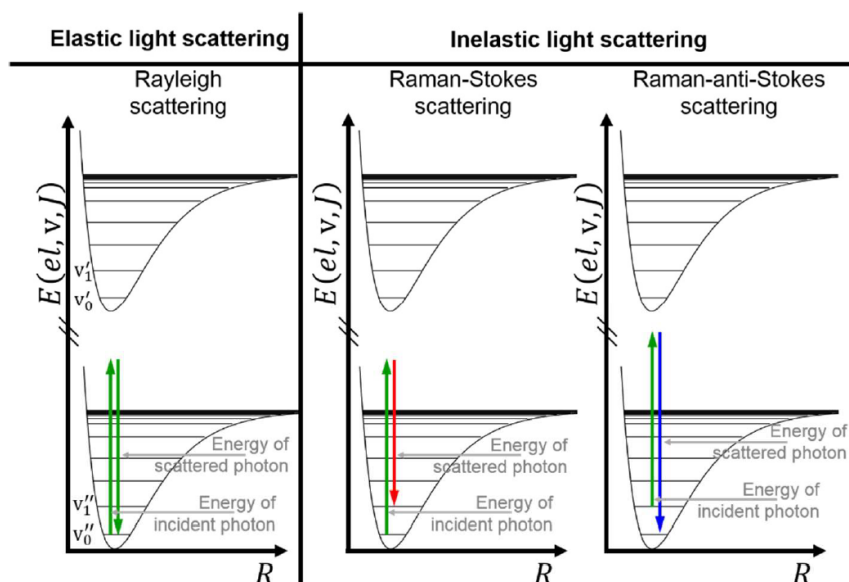


Figure 10: Interaction mechanisms between light and molecules relevant for Rayleigh scattering, Raman Stokes scattering and Raman anti-Stokes scattering; vibrational and no rotational levels are shown; graphic from Braeuer [141]

However, not all rotations and vibrations of a molecule are Raman active. Instead, only those which change the polarizability of the molecule within the external electric field, that oscillates with the frequency of the exciting quasi-monochromatic UV-, VIS- or NIR laser light, cause the inelastic Raman scattering effect.

Compared to the absorption-based infrared spectroscopy, homonuclear molecules such as oxygen, nitrogen or hydrogen are Raman-active but not IR-active, since the polarizability is affected but not the dipole moment [141] (compare Figure 11).

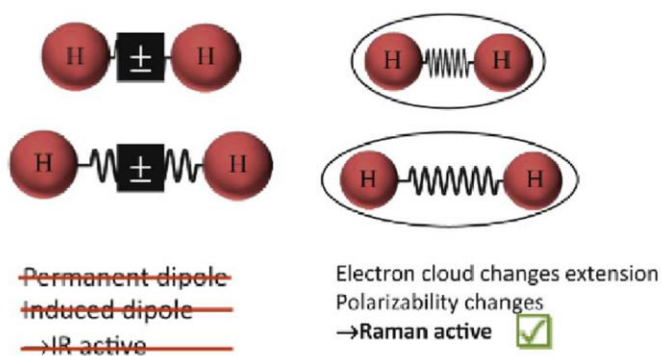


Figure 11: Comparison between IR and Raman activity regarding the vibration of the hydrogen molecule; graphics from Braeuer [141]

This is especially relevant for the amount of nitrogen or oxygen that is quantified by *in situ* Raman-stokes scattering in the VLE studies of this thesis, which could not be determined by IR-Spectroscopy.

Since the Raman-stokes signal intensities are by roughly 3-4 magnitudes weaker than the signal intensities from Rayleigh scattering, which in turn are 3-4 magnitudes weaker

compared to the incident excitation light [142], the separation of the Raman signal from the Rayleigh signal must be achieved by including suitable optical elements such as filters and dichroic mirrors (compare build-up of Raman probe head in 4.1.2).

3.3.1 Raman spectra

Due to the earlier mentioned shift in wavelength of the Raman-scattered light depending on the bonds or molecular structure of the scatterer (molecule), a Raman spectrum typically shows the intensity (or counted photons) over the Raman shift $\Delta\bar{\nu}$. The differences between Raman spectra that are based on either wavelength, wavenumber or the Raman shift, are visualized in Figure 12. Therein a liquid phase mixture spectrum of the binary system 1-octanol/ N_2 is shown, featuring the CH-stretch vibration band, as well as the OH-stretch and N_2 -stretch vibration bands.

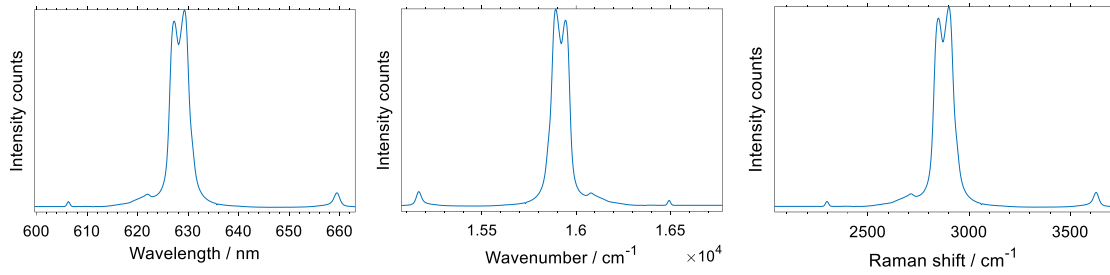


Figure 12: Raman spectrum of saturated liquid phase binary 1-octanol/ N_2 system at 613K and 9MPa; plotted over wavelength, wavenumber and Raman shift (compare Figure 26 in experimental section)

The Raman shift $\Delta\bar{\nu}$ in cm^{-1} can be obtained by the difference between the excitation wavenumber ν_0 and the wavenumber of the pixel on the detector chip of the spectrometer ν . The wavenumber is hereby the reciprocal value of the wavelength λ .

$$\Delta\bar{\nu} = \nu_0 - \nu = \left(\frac{1}{\lambda_0} - \frac{1}{\lambda} \right) \cdot 10^7 \quad (35)$$

3.3.2 Quantitative Raman spectroscopy

Physical sound relations for quantitative Raman spectroscopy of a binary system consisting of compounds i and j are visualized in Figure 13 and are provided by equations as follows,

$$r_{i,j} = \frac{I_i}{I_j} = K_{i,j} \cdot \frac{z_i}{z_j} = K_{i,j} \cdot R_{i,j} \quad (36)$$

$$z_j = \frac{1}{1 + (r_{i,j} \cdot K_{i,j})} \quad (37)$$

wherein r_{ij} is the binary ratio of Raman signals I . These signals I that must be clearly assignable to either compound i or j can be correlated with the mole fractions z (compare eqn. (10)) by the binary Raman calibration constant K_{ij} , which should not be mistaken for the minor-letter binary interaction coefficient of an EoS. The given equations, with eqn. (37) being a derived form of eqn. (36), can be considered valid no matter which substances at what conditions are studied [83,141]. The relations have to be gained through calibration, which marks the beforementioned sensible step in any quantitative Raman spectroscopic operation.

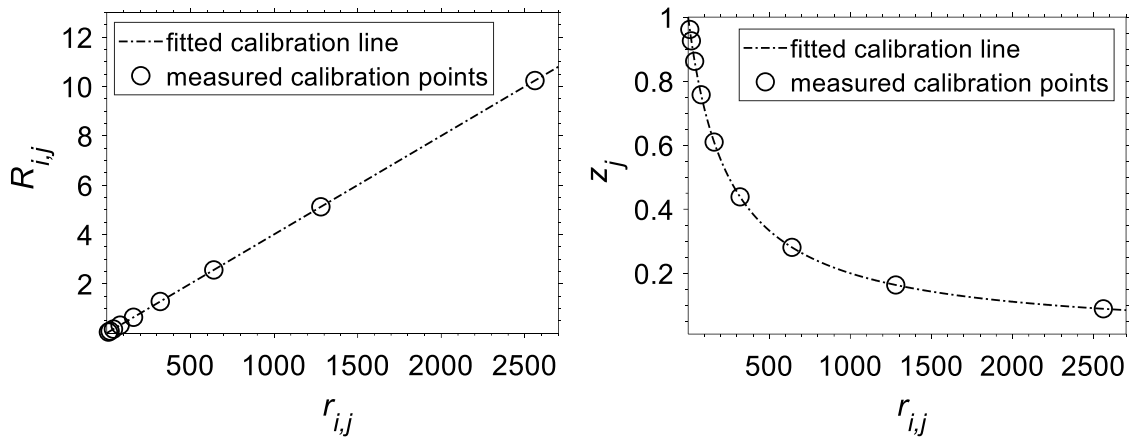


Figure 13: Linear and nonlinear Raman calibration for a binary system of compounds i and j

If a ternary system with compounds i, j and k is regarded, it is possible to calibrate two binary systems of the ternary system, since a third binary calibration factor can be obtained through division of the other two binary calibration factors, as shown by eqn. (38). The compositions of the ternary system can be calculated according to eqn. (39) and (40).

$$K_{i,k} = \frac{K_{i,j}}{K_{j,k}} \quad (38)$$

$$z_i = \frac{1}{1 + \left(\frac{1}{K_{i,j} \cdot r_{i,j}}\right) + \left(\frac{1}{K_{i,k} \cdot r_{i,k}}\right)} \quad (39)$$

$$z_j = \frac{1}{K_{i,j} \cdot r_{ij} + 1 + K_{k,j} \cdot r_{k,j}} \quad (40)$$

In several publications, calibrations are however performed that regard a correlation which differs significantly from the given relations, by correlating for instances molalities or concentrations with the Raman signal I . While interpolations and extrapolations of eqn. (36) and (37) are feasible due to their physical meaning, the same does not count for alternative calibration equations, which can finally lead to erroneous results.

The signal I can be quantified by different methods, that can be distinguished by considering either the peak height or the peak area. If spectra of a pure compound or for a constant mixture composition are evenly normalized within the same spectral range, the area and thus the Raman signal intensity remains constant. This is however not the case for the peak height approach, which can be proven in Figure 14, where evenly area-normalized spectra of pure 1-octanol at liquid state along the isobar of 3MPa are shown.

As it can be seen, the peak height of the CH stretching vibration can vary significantly over the regarded temperature range and could thus cause an erroneous Raman signal, while the Raman signal area I remains constant. Therefore in the works that are discussed in this thesis, only the Raman signal area is considered.

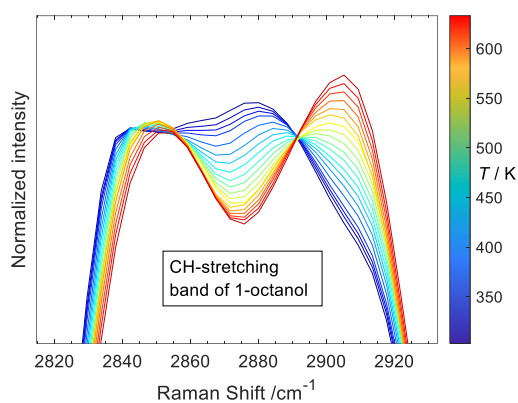


Figure 14: Evenly normalized Raman spectra of liquid 1-octanol in dependence of the temperature along the isobar of 3 MPa

4 Experimental

4.1 Experimental Setup

The microcapillary setup that is used in this work is shown in detail in Figure 15. The parts and devices are listed in detail in Table 3.

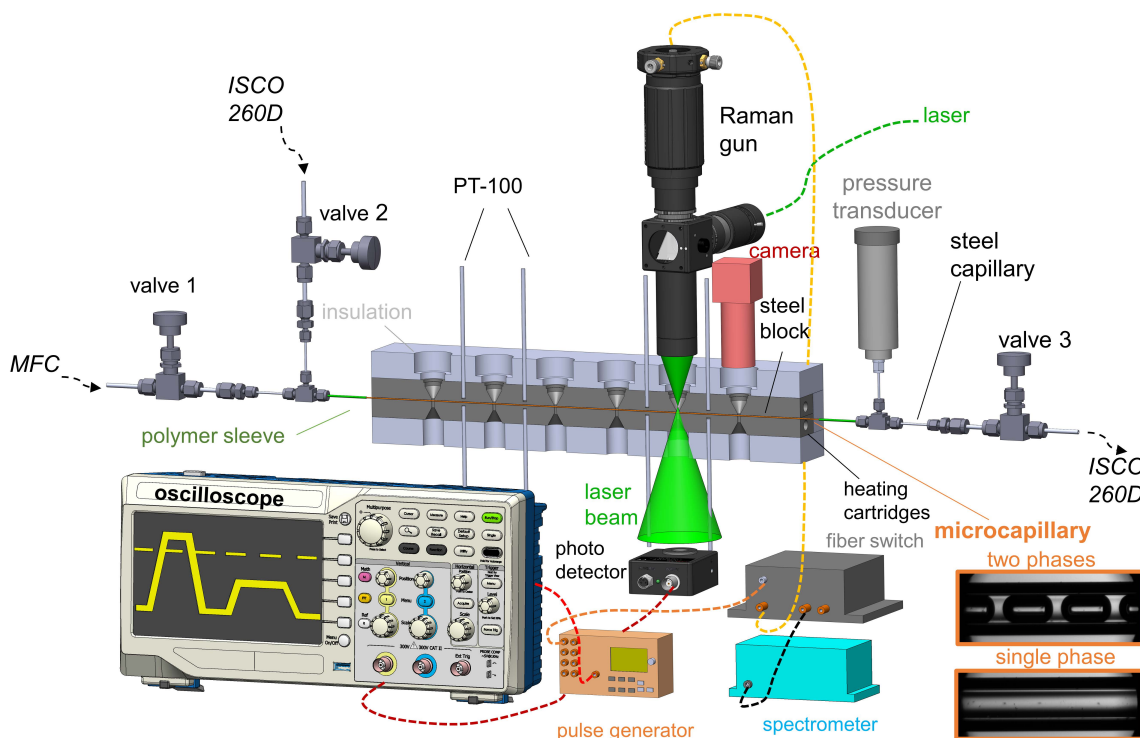


Figure 15: Microcapillary setup for determination of thermodynamic data; the left feed line is in the design for the VLE measurements; the feed line and mixing section can differ for other experiments (see Figure 16)

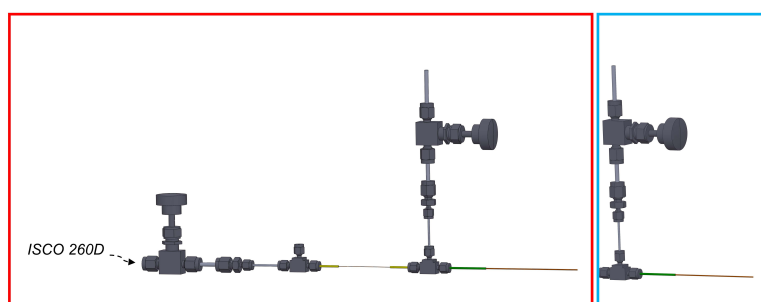


Figure 16: Configuration for liquid feeding of CO₂ regarding mixture phase density measurements (left); right: configuration for saturated vapor pressure measurements

The setup consists of two feed lines and one drain line. The upper feed line is connected to a high-pressure syringe pump (Teledyne ISCO 260D) and is used to feed the here regarded more-dense compounds (e.g.: OME_n, ethanol, 1-octanol, n-alkane) pulsation-free to a T-junction. The left feed line is used for the supply of the less-dense (regarding atmospheric conditions) compounds.

Table 3: List of devices and parts shown in the experimental setup (Figure 15)

description of part / device	Manufacturer and <i>model</i>	Features / details
High pressure syringe pump	Teledyne <i>Isco 260D</i>	-
pipes, connectors, T-junctions, valves	Swagelok, HPS, Fitok	size of 1/8'' and 1/16''; material: AISI 316
microcapillary	Molex Polymicro Technologies	Material: Fused silica with polyimide coating; outer diameter: 1/32''
PT-100	FuehlerSysteme eNET	four-wired PT-100 sensors
Pressure transducer	Keller <i>PA-33x</i>	-
Steel block	self-engineered	Material: Steel 1.1740
Heating cartridges	Friedr. Freek	Length of 160 mm
Raman gun	self-engineered	
Inorganic foam (insulation)	Techno Physik Group <i>Multitherm 550</i>	Material: silicate fibers, alkali oxides
Polymer sleeve	Idex H&S <i>different models</i>	Materials: PEEK, FEP
camera	Allied Vision <i>Guppy Pro</i> and <i>Alvium G1</i>	<i>Guppy Pro</i> : 656 x 492, 123 fps; <i>Alvium G1</i> : 728 x 544, 276 fps
cw laser	Hübner <i>Cobolt Samba</i>	Nd:YAG; $\lambda = 532$ nm, $P_{max} = 1000$ mW
Fiber switch	Piezzo System Jena	-
oscilloscope	Tektronix <i>TBS 2000</i>	-
Pulse generator	Quantum composer <i>9520 series</i>	-
spectrometer	Ocean optics <i>Qepro series</i>	-

It is thus not connected in case of the vapor pressure measurements of pure compounds, wherefore the T-junction is closed to that side by a blind plug. For the VLE measurements a gas (e.g.: O₂/N₂/synthetic air), is fed precisely by a Bronkhorst mass flow controller (EL-Flow Prestige) through the left feed line, while for the mixture density measurements another Teledyne Isco 260D is connected for the supply of CO₂ at liquid state.

All experimental procedures have in common that another Teledyne Isco 260D is used as a take-up pump, located at the downstream end of the setup. The take-up pump runs in reverse mode compared to the feeding pumps, collects the conveyed fluid and keeps thus the system pressure stable. The fused silica microcapillary is connected to the steel pipe system via polymer sleeves and is embedded in a 350 mm long steel heating block (latest version), that is insulated by an inorganic foam. The steel block is temperature conditioned through eight 160 mm long heating cartridges integrated from both sides on circular path around the capillary. The temperature at the regarded measurement spot is taken as the average of four surrounding PT-100 thermo-resists. The pressure is taken by a Keller pressure transducer

(Keller PA-33x) that is located shortly behind the microcapillary on another T-junction. Holes on top and on bottom of the insulation and steel block provide optical access for the allied vision camera, the self-engineered Raman sensor and the light barrier technology. The “Raman gun” (Raman sensor probe head) can focus 532 nm excitation light from a frequency-doubled Nd:YAG Hübner Cobolt Samba continuous wave laser into the microcapillary. The light barrier system that consists of an oscilloscope, a photo detector, a pulse generator, a fiber switch and a spectrometer is in detail discussed in the following section.

4.1.1 Light barrier system for phase-selective measurement

The light barrier system enables the phase-selective Raman measurement regarding the alternating/segmented flow (compare insert under “two phases” at the bottom right of Figure 15) of the VLE experiments. Due to the difference in refractive index between the vapor and the liquid phases, more or less green excitation light is collected by the photo detector that is positioned under the heating block. This causes a clearly differentiable signal which is visualized by the oscilloscope that is connected to the photo detector (compare oscillation shown in yellow in Figure 15). Therewith a pulse frequency can be obtained by the connected pulse generator with which the fiber switch, which has one input and two output channels, is precisely triggered that only Raman-Stokes scattered signal light (that is guided from the Raman gun to the fiber switch) of the investigated phase is transferred further from the fiber switch to the spectrometer. The Raman-Stokes scattered signal light of the other (not regarded) phase is guided to the second dead-ended channel. For the case of investigating the saturated liquid phase composition of a 5 Hz Taylor-Flow for example, the spectrometer accumulates Raman signal within the chosen integration time of 4 s of 20 liquid segments, while all the Raman signal of the 20 saturated vapor phase segments is filtered by the photoelectric guard of the fiber switch.

4.1.2 Raman probe head

The Raman probe that is used in this work is visualized in sectional view in Figure 17. It is a 1-inch type-system that is built in backscattering configuration mainly with components from the supplier Thorlabs. The laser light is guided by an optical fiber to the Raman probe. When the light beam exits the fiber through the coupling, it diverges and it's collimated by the first of in total three plano-convex lenses in the probe. The light passes then onto a

dichroic mirror that reflects light of wavelengths shorter than 550 nm and transmits light of wavelengths above. The second plano-convex lens focuses the light onto the measurement spot. Rayleigh-scattered light, Raman Stokes-scattered light and Raman anti-Stokes scattered light is collected through back-scattering and is collimated when passing through the second lens. However, only the Raman Stokes-scattered signal light can pass through the dichroic mirror, since its wavelength is mainly larger than the 550 nm cut-on wavelength.

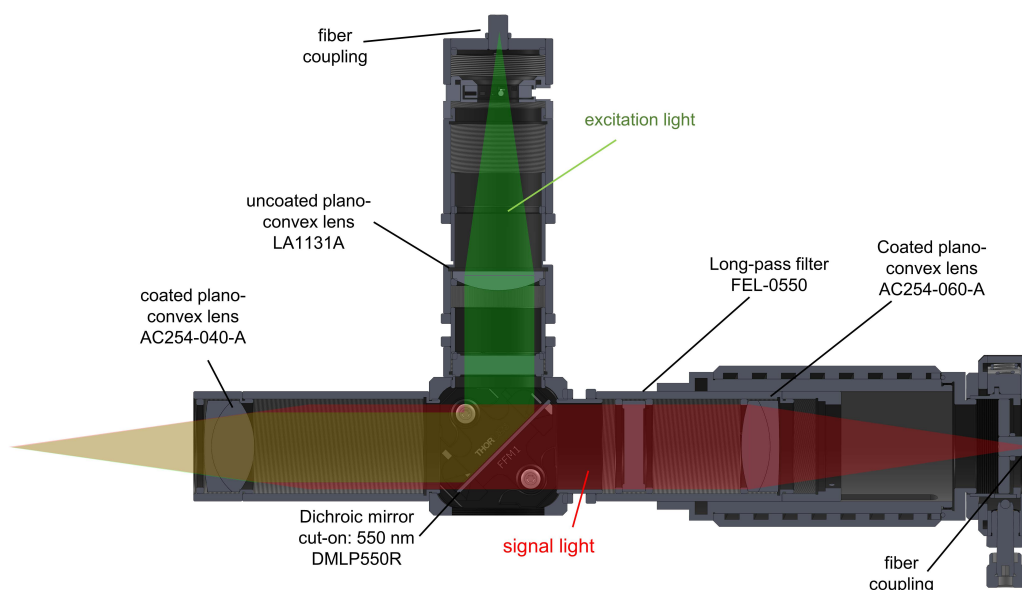


Figure 17: Sectional view of Raman probe head (“Raman gun”)

In order to ensure that all light of lower wavelengths is filtered, the Raman Stokes-scattered signal light further passes through a longpass filter with a cut-on wavelength of 550 nm, before it is focused by the third plano convex lens onto the fiber coupling. From there the signal light is guided through another fiber to the fiber switch and from there to the spectrometer.

4.1.3 Control of experimental setup

The system is controlled by a Matlab Graphical User Interface (GUI), that communicates with the thermostat, spectrometer and pressure transducers (one indicating the system pressure and one that is located prior to valve 1 of the left feed line). The communication with the laser, the oscilloscope, the allied vision cameras, as well as the pumps and the MFC is provided by synchronously running suppliers’ software.

Figure 18 shows the user interface for the last regarded system ethanol/CO₂. The Raman spectra and Raman backgrounds can be taken by pressing the respective buttons. The spectral range, as well as integration time (here: 4 s) and the number of spectra (here: 32) can be furthermore adjusted. Additional information, such as pressure, temperature, global composition, information on the phase state (here: saturated vapor phase) etc. are moreover stored in the spectral data. The steel block temperature can be controlled by assigning a value at “Current Setpoint”.

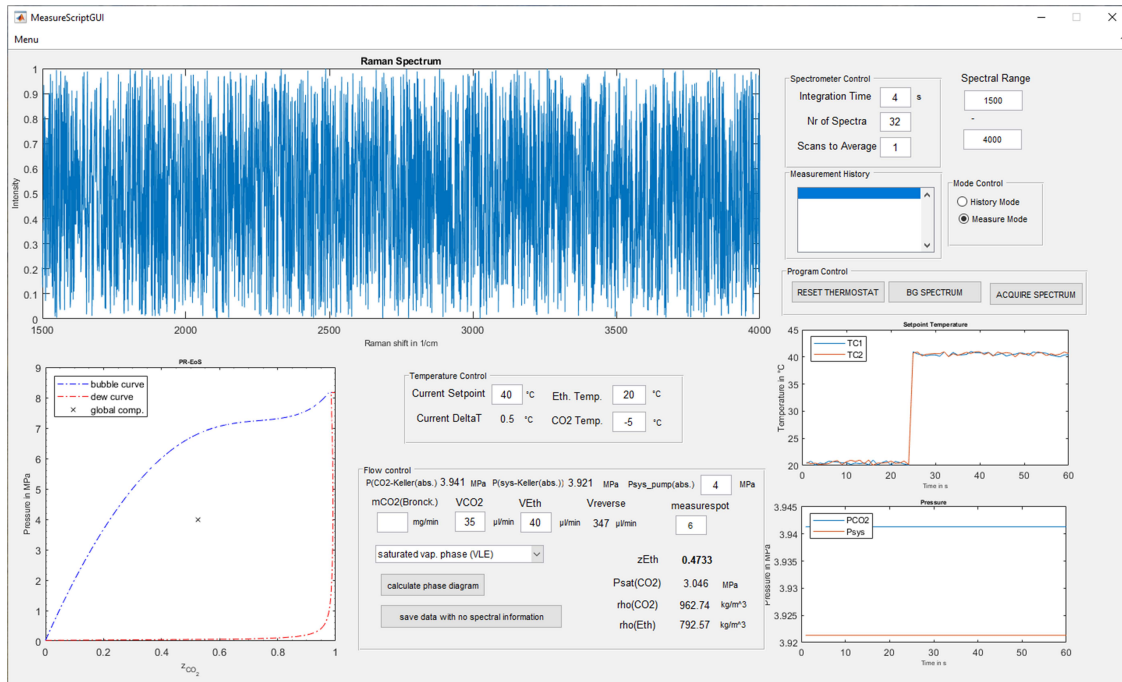


Figure 18: Matlab GUI for setup control (here: system of ethanol/CO₂).

For the feeding pumps it is of major importance to assign accurate density correlations in order to obtain a precise mass flow from the volume flows of the pump. For the here shown example, the Tait equation (see eqn. (26)) is used as a density correlation for ethanol, while the Wagner and Span EoS is used for CO₂. When a gas is fed (N₂, O₂, synthetic air) instead of CO₂ that is fed in the liquid state, a precise mass flow is already obtained by the Bronkhorst software. The GUI allows furthermore the prediction of the vapor/liquid two-phase regime by the in the program embedded PR-EoS and visualizes additionally the global composition.

4.1.4 Preparation of microcapillaries

The Molex Polymicro Technologies fused silica microcapillaries have to be prepared in order for being used in the microfluidic setup. The whole procedure is summarized by the flow chart in Figure 19 and is in detail described in the further.

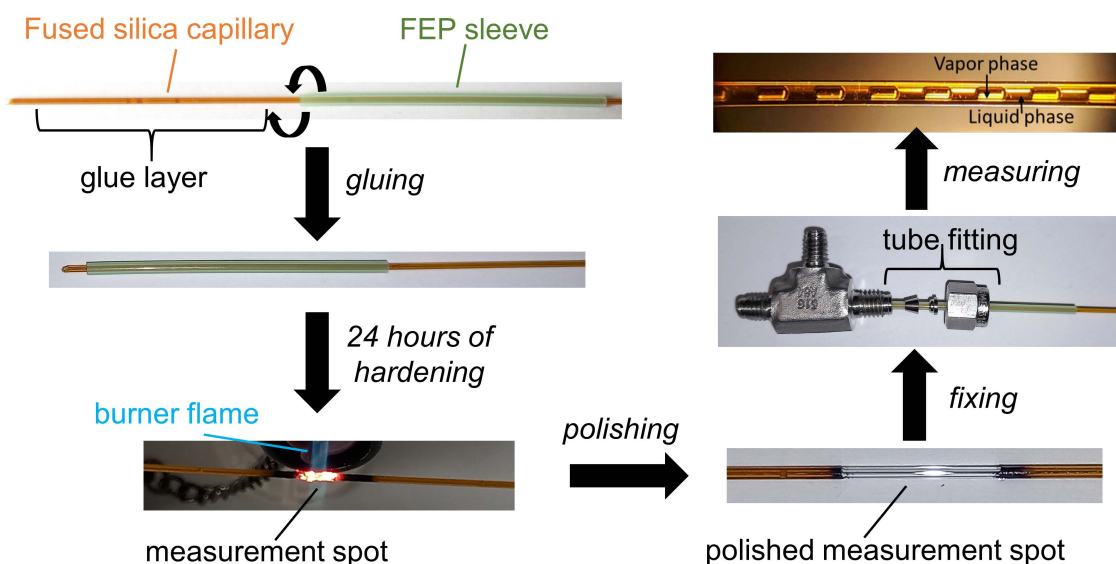


Figure 19: Flow chart describing the preparation of fused silica microcapillaries

In the first step the microcapillary is cut with a side cutter to match the correct size between the two T-junctions shown in Figure 15. Glass fragments that might remain from cutting on the ends of the capillary, can be carefully removed with a small pipe deburrer and a tweezer. IDEX H&S polymer sleeves with an inner diameter that matches the outer diameter of the microcapillary are then put over the cut ends of the microcapillary. The region where the sleeve sits in its final position is then covered with a fine layer of premixed UHU Plus Endfest 2-component glue, which can be but not has to be temperature-conditioned by a heat gun. The weight fraction of the hardener in the 2-compound glue can hereby vary between $w = 0.25 - 0.50$, in order to obtain a firm material in its final shape. The sleeve is then slowly pulled over the glue in rotary motion, stopping a few millimeters from the cut end. It must be taken care that glue neither plugs the open end of the capillary nor is left excessively on the top end of the sleeve. After a time of 24 hours the connection is hardened. In order to obtain optical accessibility for the Raman gun and the camera, the polyimide coating of the microcapillary has to be removed for roughly 10 millimeters at the measurement spots, by using a Rothenberger industrial burner (model: Gas Turbo). The coating-freed spots are then polished with an ethanol-soaked Kimtech cleaning paper. This step is especially crucial, since any rests of char cause a Raman signal that interferes with

the CH-bending vibration, as well as with the CH- and O₂-stretching vibrations, or could also disturb the photo-optical evaluation procedure. The capillary can then be connected to the T-junctions by 1/16-inch tube fittings and can then be assembled straight or curvy between the end of the steel block and the second T-junction. The latter can be advantageous especially when the capillary is under high mechanical and thermal stress.

The in this work prepared fused silica capillary lasted pressures of up to $p = 30$ MPa and has been experimentally tested at temperatures of $T = 673$ K with chemically harsh media like supercritical water. As proof, Raman spectra that were measured with the microfluidic setup showing the OH-stretching vibration band of liquid (for $T = \{473 - 623\}$ K) and supercritical water (for $T = 673$ K) along the isobar of 25MPa are provided in Figure 20.

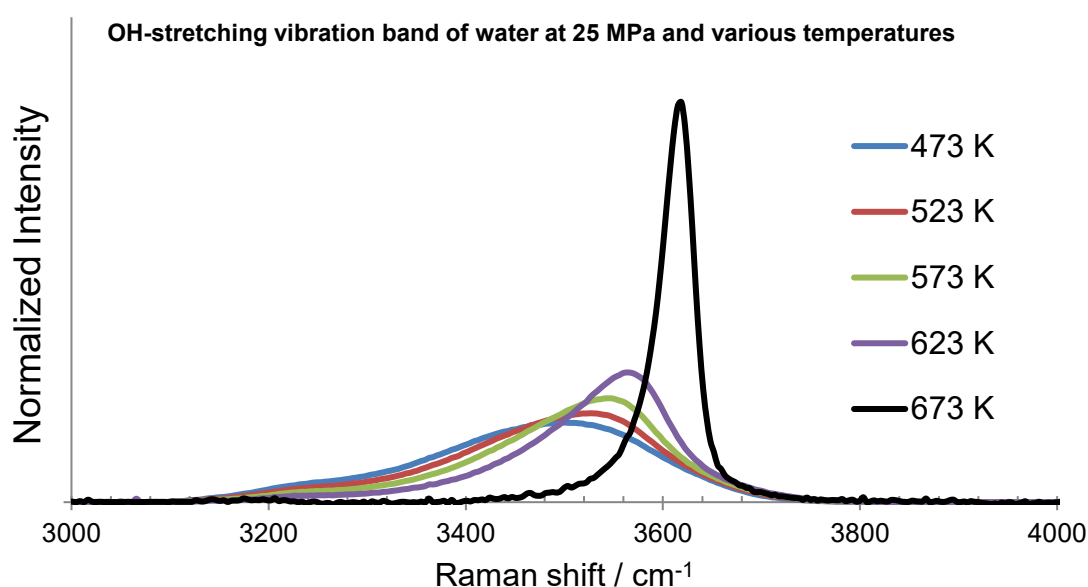


Figure 20: OH-stretching vibration band of water in the liquid ($T = \{473 - 623\}$ K) and supercritical state ($T = 673$ K) along the isobar of $p = 25$ MPa; measured with the microfluidic setup

4.1.5 Microfluidic behavior and segmented flow

The behavior and flow of a fluid in the fused silica microcapillary are of high importance for the measurement result per se. For the vapor pressure measurements, the fluid is at rest inside the microcapillary and the transition from vapor to liquid phase is optically detected by the formation of bubbles and liquid slugs. In contrary to that a segmented flow pattern is set for the VLE and saturated density measurements of binary or ternary systems, to which can be also referred to as “Taylor flow”.

As described earlier in section 4.1, the left feed line is closed for the measurements of the saturated vapor pressure of a pure compound, while the way of feeding of the less-dense

compounds (N_2 , O_2 , synthetic air, CO_2 ; less dense in respect to atmospheric conditions) is of decisive importance for the feasibility and the result of the experimental procedure. For the VLE measurements of the fuel/air systems, N_2 , O_2 or synthetic air (in the further: gas) are fed by the Bronkhorst MFC towards the T-junction. The mixing section between gas and fuel is located shortly before the fused silica microcapillary, as visualized in Figure 21. The fuel is flowing through the upper feed line of the setup through the upper part of the T-junction and around the steel pipe through which the gas is fed. The longitudinal channel of the T-junction is bored through, in order to move the gas-feeding pipe further over the point where the cross channel ends. At the mixing point, the characteristic flow of vapor and liquid segments is formed, since the gas which exits the pipe in a “jet-like” fashion, breaks up the fuel to form the described segments.

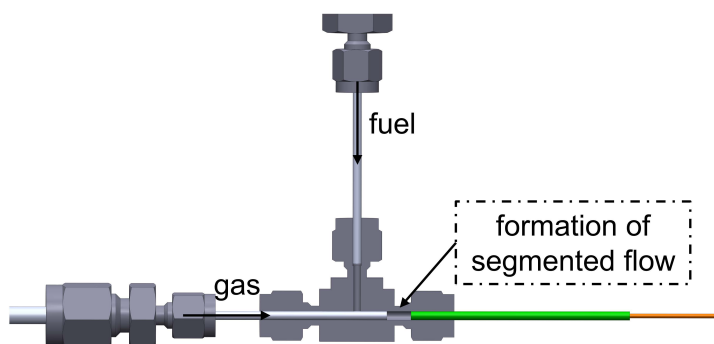


Figure 21: Mixing section design for VLE experiments; the 1/16-inch T-junction is presented in sectional view

This formation of a Taylor flow outside the heating section is fairly easy for the fuel/air systems, due to the large differences in viscosity and density of the regarded pure compounds, respectively the formed vapor and liquid mixture phases, as well as due to the large vapor/liquid two-phase regime at room-temperature where the mixing is performed. Even the global composition can vary over a relatively wide range for the fuel/air systems. This experimental ease does not necessarily count for the system ethanol/ CO_2 , also due to the special properties of carbon dioxide. The global composition is here also more decisive for obtaining a segmented flow suitable for measurement. The formation of a Taylor flow is also found to be significantly better when the two compounds are mixed at temperatures of at least $T > 303.15$ K. As a consequence, the mixing section is transferred into the heating block by inserting a smaller CO_2 -feeding fused silica microcapillary into the larger measurement fused silica microcapillary. It should be further mentioned that the mixing section has to be designed differently depending on the mixtures that are studied. For instance Luther et al. [143] fed CO_2 through the larger of two plugged in one another

capillaries, while water and ethyl acetate were fed through the smaller one. In a consecutive study in which this thesis' author was involved (not included in this thesis) regarding the ternary system n-dodecane/1-octanol/ CO_2 , n-dodecane and 1-octanol were fed together through the left feeding line (and thus through the smaller capillary), while CO_2 was added through the upper feeding line and thus through the larger capillary.

4.2 Experimental procedure

The experimental procedures are described as follows. More details are provided in the Results and Discussion section.

4.2.1 Vapor pressure measurements

A pure compound is fed at elevated pressure in liquid state through the microcapillary and is collected by the take-up pump. The temperature of the microcapillary's heating zone is then adjusted by the heating block and remains constant for the acquisition of one experimental point. The reverse volume flow of the feed pump is then increased in order to lower the system pressure so long until the liquid compound reaches the unsaturated vapor state. The take-up pump can then be stopped and valve 3 is closed. The fuel in the vapor state is thus at rest inside the heating zone of the microcapillary.

The isothermal compression is then started by conveying with the feed pump through the upper feed line against the closed valve 3 (compare Figure 15), while the left feed line is not connected as mentioned earlier. The rate of pressurization lies hereby within the range of $\{0.01 \text{ to } 0.02\} \text{ MPa min}^{-1}$.

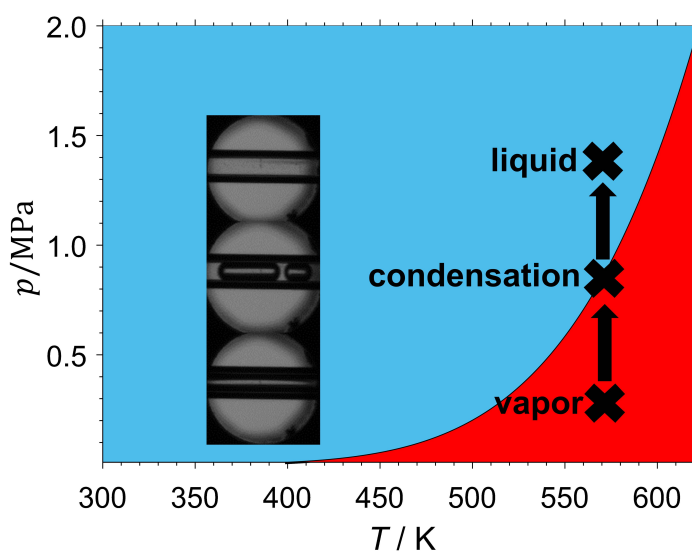


Figure 22: Principle of saturated vapor pressure measurements in microcapillary; graphic appeared as cover art in [116]

The Guppy Pro camera (Allied Vision F-046) records images from the heating zone of the microcapillary. The pressure, at which a phase change from vapor to liquid (condensation) is visible inside the capillary is taken as the vapor pressure for the measured temperature T . The vapor/liquid phase change is indicated by the formation of droplets or the formation of a film on the internal wall of the capillary. [116]

4.2.2 VLE measurements

The experimental procedure starts by taking a background Raman spectrum, by adjusting the system temperature and by choosing the system pressure, which remains constant over an experimental series (isobaric dataset). The system pressure is adjusted by the fuel feeding pump of the upper feed line and the take-up pump for constantly opened valves 2 and 3 (compare Figure 15). When the chosen pressure is reached, the volume flows of fuel pump and take-up pump are changed in order to equal each other. Fuel is thus flowing constantly at constant pressure through the microcapillary. Then the gas bottle pressure is set approximately {0.5 to 1}MPa above the chosen system pressure, in order to feed the regarded gas (N_2 , O_2 , synthetic air) through the MFC. When a pressure greater than the system pressure is reached in the left gas feeding line, valve 1 is opened. Depending on the set global composition, either a segmented two-phase flow can be observed in the heating zone of the microcapillary (VLE measurements) or a single-phase flow is visible (in the case of the calibration series). After the Raman spectra are taken the next higher temperature can be set following an isobar, since pressure changes require long-lasting readjustments of gas bottle pressure, system pressure and flow ratio.

For the determination of VLE, spectra of different thermodynamic regimes must be taken, as indicated by the example Txy -diagram in Figure 23. In order to link Raman signal ratios of saturated liquid and vapor phases to mole fractions, as visualized by the red and blue lines in Figure 23, calibration measurements have to be carried out for a precisely known homogeneous mixture (compare section 3.3.2). The calibration is therefore performed inside the unsaturated liquid or vapor phase, or if thermally possible in the homogeneous regime above the mixture critical temperature for the regarded pressure. Hereby it must be taken care of, that the mixture is homogeneous when it reaches the measurement spot, which might not occur if the fluid velocity is too high. The homogeneity is ensured by controlling the oscilloscope for any sign of oscillation or by observing the homogeneous flow via camera.

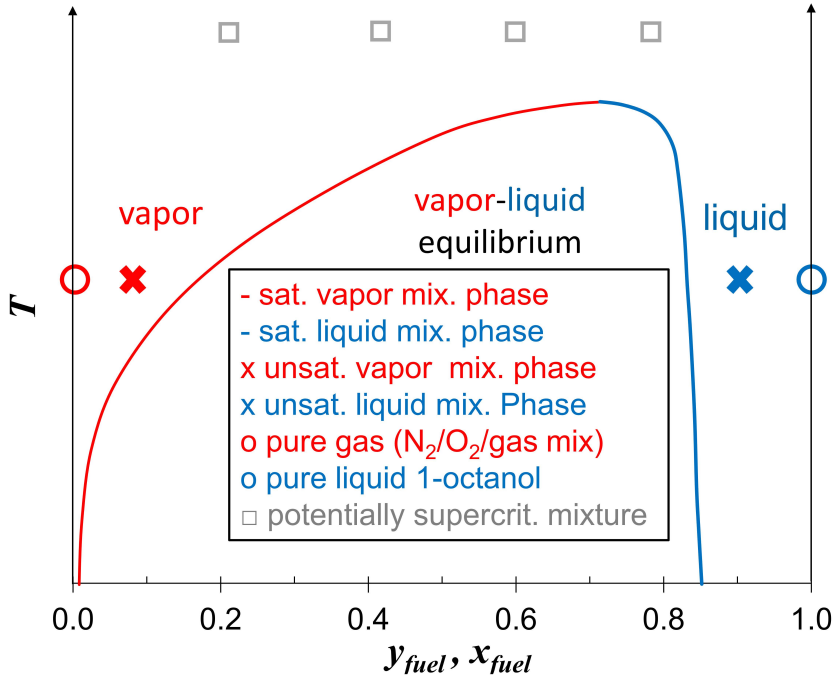


Figure 23: Example isobaric Txy -diagram of a fuel/gas system (here: 1-octanol/ O_2 and 1-octanol/ N_2) indicating different thermodynamic regimes for spectral data acquisition

Furthermore, the precision boundaries of the devices must be considered. The Isco 260D syringe pumps tend to start pulsating for volume flows below $8 \mu\text{L} \cdot \text{min}^{-1}$, while the precision of the Bronkhorst MFC is expressed by a “trumpet graph”. By the latter, the manufacturer indicates the increasing uncertainty of the device at the lowest flows in relation to the calibrated flow range. After well considering these obstacles, 32 single spectra are taken per calibration point. Within the calibration campaigns the pump volume flows were in the range of $\dot{V} = \{8 \text{ to } 110\} \mu\text{L} \cdot \text{min}^{-1}$, while the mass flow set for the MFC was ranging within $\dot{m} = \{0.4 \text{ to } 7.5\} \text{mg} \cdot \text{min}^{-1}$.

For the VLE measurements a global composition inside the vapor/liquid two-phase regime is set and a Taylor flow of alternating vapor and liquid segments is formed. Then the light barrier technology is adjusted to acquire either 32 single spectra from the saturated liquid or the saturated vapor phase, while the spectra of the corresponding non-investigated phase are not saved. Typical flows during the VLE experiments were $\dot{V} = \{15 \text{ to } 60\} \mu\text{L} \cdot \text{min}^{-1}$ for the feed pump and $\dot{m} = \{0.6 \text{ to } 3\} \text{mg} \cdot \text{min}^{-1}$ for the MFC. The whole Raman spectral evaluation was programmed as a procedural code in Matlab and is summarized by the flowchart given in Figure 24 for binary systems fuel/ N_2 and fuel/ O_2 .

For a ternary system fuel/ N_2/O_2 the evaluation procedure is applied at once with no difference to the binary systems. The principle and the evaluation procedure as such are

identical for all fuel/gas systems, except for the liquid film correction, where different methods were applied. In the first step, the single Raman spectra are analyzed in order to locate the relevant Raman signals (compare Figure 25). The single spectra are area-normalized (regarding the CH stretch vibration band) and single spectra as well as the from the single spectra obtained mean spectrum are baseline-corrected (see Figure 26).

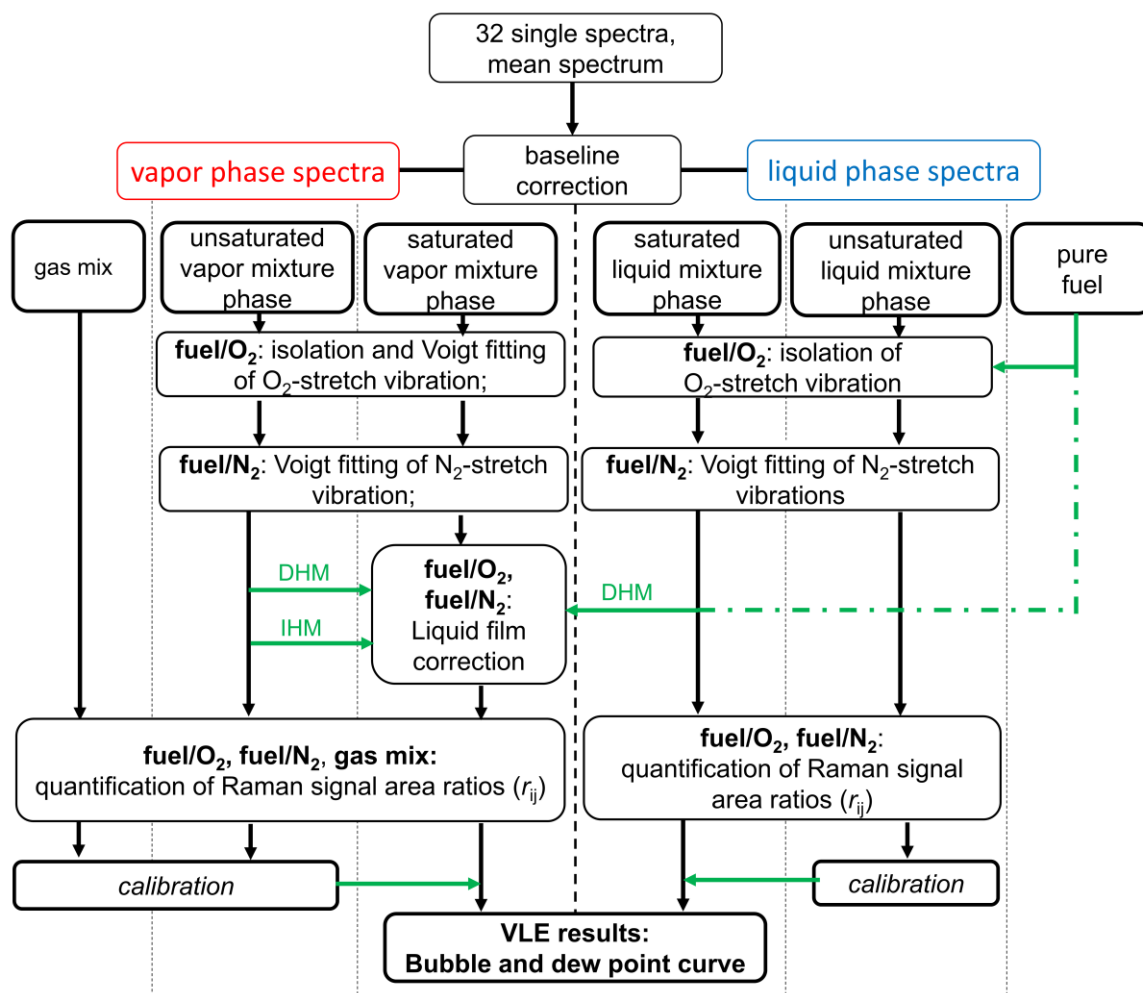


Figure 24: Flowchart of Raman spectral evaluation procedure (programmed in Matlab); the difference lies in the liquid film correction

The baseline consists of chosen node points, which are located in the spectra at positions where the molecules of the system do not feature any Raman signal. The node points are connected by cubic piecewise interpolation, except in the range of the O₂-stretch and N₂-stretch vibration bands, where slightly better results were obtained for linear connections between the node points.

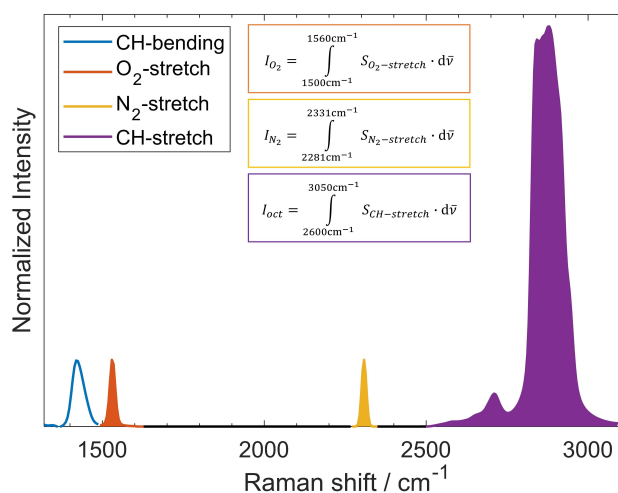


Figure 25: Model spectrum showing the relevant Raman bands and Raman signals I for the evaluation of the systems 1-octanol/ N_2 and 1-octanol/ O_2 [67]

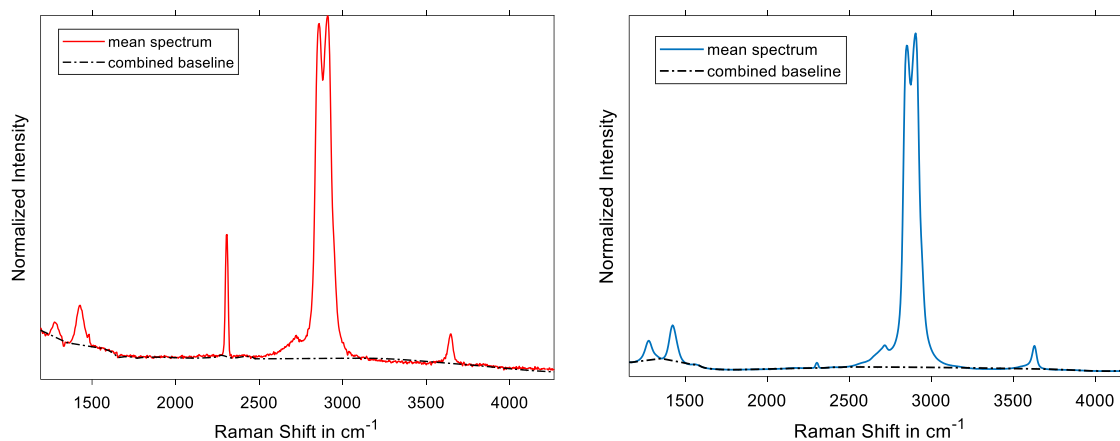


Figure 26: Baseline correction of saturated vapor phase spectra (left) and saturated liquid phase spectra (right) of binary system 1-octanol/ N_2 at $p = 8$ MPa and $T = 573$ K

Spectra of systems containing oxygen, such as 1-octanol/ O_2 , have to be deconvoluted since the O_2 -stretching vibration band is overlapped by the CH-bending vibration band, as visualized in Figure 27. As shown above in the flowchart (compare Figure 24), spectra of the pure unsaturated liquid fuel are necessary for the direct hard modeling of the saturated liquid phase spectra, while indirect hard modeling using pseudo-Voigt profiles is applied for the saturated vapor phase spectra. Regarding the deconvolution of the saturated liquid phase spectra of fuel/ O_2 systems, it is of utmost importance that the spectrum of the pure unsaturated liquid fuel is taken at the same temperature as the saturated liquid phase spectrum, due to the temperature sensitivity of the Raman bands (compare Figure 14). The effect of the pressure on the shape of Raman bands in a liquid phase spectrum was however found to be marginal for the bands and pressure range regarded in this work.

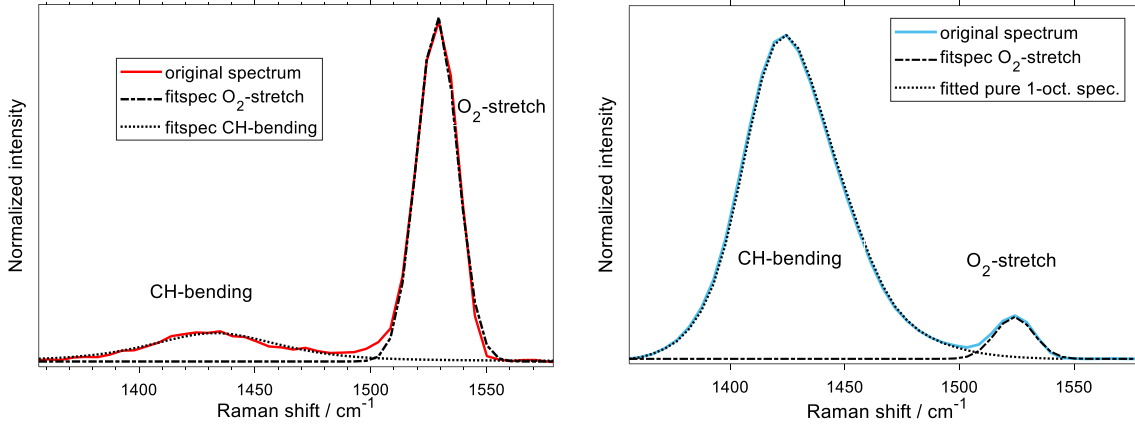


Figure 27: Deconvolution in order to isolate the O_2 -stretch vibration band of saturated vapor phase (left) and saturated liquid phase spectra (right) of the binary system 1-octanol/ O_2 at $p = 8$ MPa and $T = 573$ K

In the following step the saturated vapor phase spectra $S^{vap,s}$ have to be corrected from a signal contribution that stems from the liquid film $S^{liq,s}$ that surrounds the vapor phase slug (or bubble) in the microcapillary (see Figure 28). Not considering this film contribution would lead to an overrepresentation of the amount of fuel in the saturated vapor phase. Hereby different methods are applied to correct $S^{vap,s,film}$ from the liquid film contribution $S^{liq,s}$, that are listed as follows. The first method that is based on the OH-stretch vibration band was already introduced in section 2.2.2.

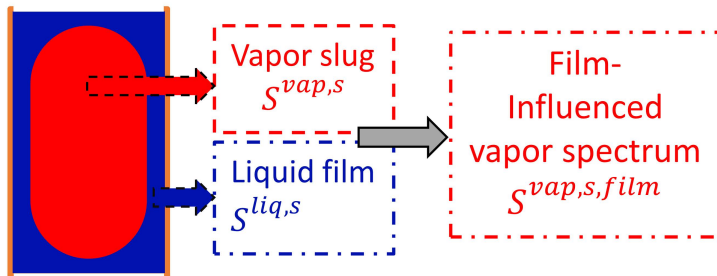


Figure 28: Liquid film contribution

Direct hard modeling (DHM) CH-stretching band approach

Another film correction is based on a similarity comparison of the CH-stretch vibration band by direct hard modeling (DHM), utilizing slight changes according to the phase state. This method was applied for the binary systems 1-octanol/ N_2 and 1-octanol/ O_2 [67]. In this approach the film influence is quantified by fitting in least-squares-sense the sum of the CH-stretch vibrations of liquid and vapor phase spectra to the CH-stretch-vibration of the original, film-influenced spectrum of the saturated vapor mixture phase ($S_{CH-str}^{vap,film}$). Therein the parameters t are varied (see eqn. (41)). The final film-corrected spectrum of the saturated

vapor phase is then described by $t_2 \cdot S_{CH-str}^{vap,mean}$ inside the CH-stretch region, as well as by the original (uncorrected) spectrum of the saturated vapor phase outside of the CH-stretch region. For the liquid film contribution spectra of pure liquid 1-octanol at same temperature ($S_{CH-str}^{liq,*}$) or of the corresponding saturated liquid phase can be used ($S_{CH-str}^{liq,s}$). Hereby no difference in the final result was found between these two options.

The expression of the true vapor phase contribution however is more challenging. Due to the high atmospheric boiling temperature of 1-octanol ($T_{oct}^{s,b}(0.1013 \text{ MPa}) = 468.3 \text{ K}$) spectra of pure vapor 1-octanol for lower temperatures would have to be taken at vacuum conditions, making Raman Spectroscopy difficult due to the low density of scattering molecules. Spectra were taken from the unsaturated vapor mixture phase (S_{CH-str}^{vap}) of the system 1-octanol/ N_2 for temperatures ranging from 553K to 613K. Therefrom a mean of the CH-stretch vibration ($S_{CH-str}^{vap,mean}$) was taken that can be considered to assume the CH-stretch vibration of vapor 1-octanol, independent from pressure and temperature.

$$S_{CH-str}^{vap,s,filim} = t_1 \cdot S_{CH-str}^{liq,*} + t_2 \cdot S_{CH-str}^{vap,mean} \quad (41)$$

In the considered temperature range from 553K to 613K the therefrom obtained results were identical to an approach, wherein the contribution of the CH-stretch vibration of vapor 1-octanol was assigned temperature-dependently by the respective unsaturated vapor phase spectra (S_{CH-str}^{vap}). The spectral differences of the CH-stretch vibration are indicated in the left spectrum of Figure 29.

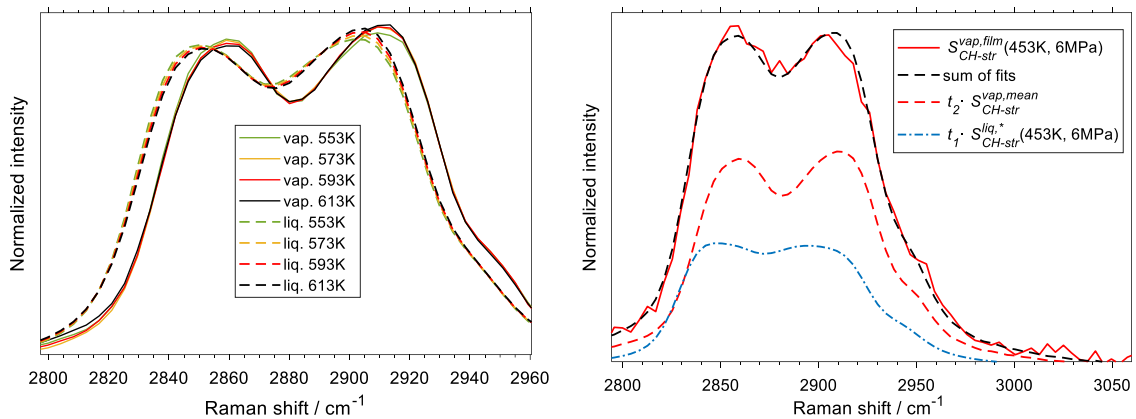


Figure 29: Comparison of CH-stretch vibration in dependence of temperature; stemming from unsaturated vapor mixture phase (1-octanol/ N_2) or pure liquid 1-octanol (left); liquid film correction of saturated vapor mixture phase spectrum for system 1-octanol/ N_2 at 6 MPa and 453 K (right) [67]

Both, a shift and difference in shape are visible, while the temperature tends to have a more significant effect on the liquid phase spectra, as the notch between left and right peak shoulders change slightly more. This justifies the use of a mean vapor phase spectrum in the liquid film correction, which is visualized in the right spectrum of Figure 29.

Indirect and direct hard modeling (IHM-DHM) CH-stretching band approach

While the liquid phase contribution is described by direct hard modeling (DHM), as in the method described above, the vapor phase contribution to the film-influenced vapor phase spectrum is found within this method by indirect hard modeling (IHM) using pseudo-Voigt profiles, as given by eqn. (42),

$$S_{CH-str,mix}^{vap,s,film} = t \cdot S_{CH-str}^{liq,s} + S_{CH-str,mix}^{vap,mod}; \quad (42)$$

$$\text{with } S_{CH-str,mix}^{vap,mod} = \sum_k^n S_{Voigt} \left\{ \sum_l^4 g_{kl} \right\}$$

wherein S_{Voigt} are the pseudo-Voigt profiles with 4 input parameters g_{kl} per profile. The profiles need to be however pre-parameterized by spectra taken from the unsaturated vapor mixture phase (S_{CH-str}^{vap}). As visualized by Figure 30 the corresponding spectrum of the saturated liquid phase $S_{CH-str}^{liq,s}$, as well as the modeled vapor phase spectrum $S_{CH-str}^{vap,mod}$, are fitted in least-squares sense to the original film-influenced spectrum $S_{CH-str}^{vap,s,film}$ in the CH-stretching vibration region, by iterating the global fit parameter t and the pseudo-Voigt parameters g_{kl} .

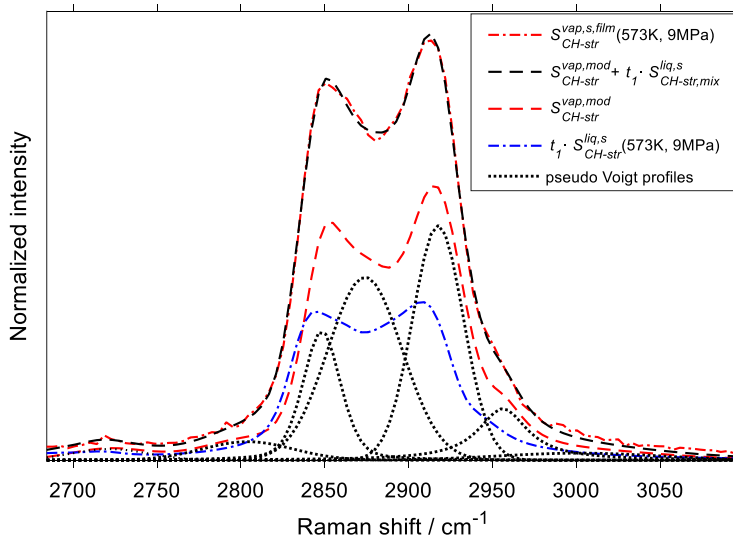


Figure 30: Correction of liquid film contribution in saturated vapor phase spectra for the binary system of n-pentadecane/ N_2 at $T = 573$ K and $p = 9$ MPa

After all evaluation steps (including the liquid film correction in case the saturated vapor phase is regarded) are carried out, the signal ratios of the spectra from both saturated and unsaturated phases can be calculated according to eqn. (36) to (40). Evaluated saturated liquid phase spectra for the binary system n-pentadecane/N₂ are as an example visualized for an isobar of 6.5 MPa and with rising temperature by Figure 31.

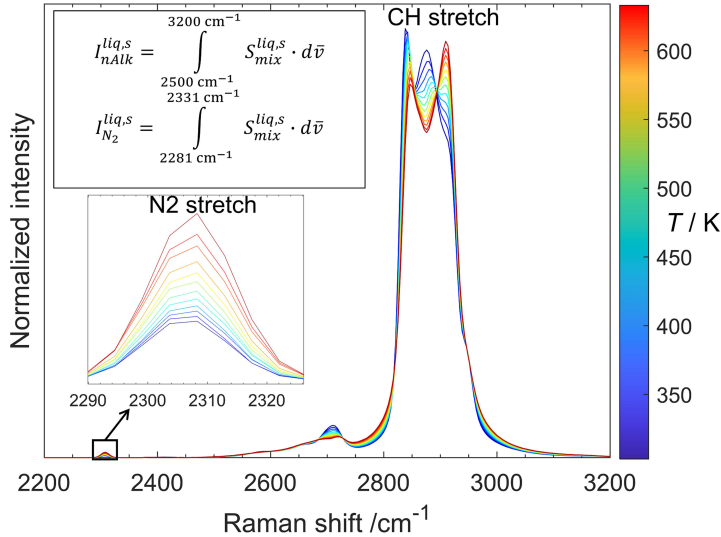


Figure 31: Evaluated saturated liquid phase spectra of binary system n-pentadecane/N₂ along the isobar of $p = 6.5$ MPa; spectra are area-normalized to the CH-stretch vibration band

In order to obtain the saturated liquid and vapor phase composition, the calibration constants K_{ij} must be known, which can be obtained according to the experimental procedure by the fits shown in Figure 13. The calibration spectra must be hereby treated as described above and visualized by the flowchart in Figure 24. Since for the calibration experiments single phase flows are obtained, there is logically no liquid film-correction necessary for the spectra of the unsaturated vapor phase.

4.2.3 Mixture density measurements

The experimental procedure starts similarly as in the before described VLE procedure. The system is pressurized while valves 2 and 3 are opened (compare Figure 15), by feeding ethanol through the upper feed line. Once the system pressure is reached for a before adjusted temperature, a blank picture of ethanol in the microcapillary is taken. CO₂, which is temperature conditioned in the pump of the left feeding line to $T = 268.15$ K and thus at unsaturated liquid state, is pressurized against closed valve 1 until the pressure is greater than the system pressure before valve 1 is then opened. The global composition can then be

adjusted in order to obtain the best suitable Taylor flow. Images and the frequency are then recorded over a time of at least 5 minutes.

The derivation of the equations with which mixture densities can be calculated are provided as follows. Considering a microfluidic flow at vapor-liquid equilibrium, the total mass passing through the microcapillary is calculated by the sum of both phases' masses. The mass flow of both vapor and liquid phases can be also expressed by the volume flows and the saturated mixture densities.

$$\dot{m} = \dot{m}^{vap} + \dot{m}^{liq} \quad (43)$$

$$\dot{m} = \rho_{mix}^{vap,s} \cdot \dot{V}^{vap,s} + \rho_{mix}^{liq,s} \cdot \dot{V}^{liq,s} \quad (44)$$

Eqn. (44) can then be also written in terms of a compound i of the binary system by including the mass fraction w . w_i refers to the global composition and $w_i^{vap,s}$ to the saturated vapor phase mass fraction of compound i .

$$w_i \cdot \dot{m} = w_i^{vap,s} \cdot \rho_{mix}^{vap,s} \cdot \dot{V}^{vap,s} + w_i^{liq,s} \cdot \rho_{mix}^{liq,s} \cdot \dot{V}^{liq,s} \quad (45)$$

Eqn. (44) and (46) can be equated (see eqn. (47)) and further simplified to yield eqn. (48). If the liquid phase is regarded instead of the vapor phase, eqn. (49) can be obtained.

$$w_i \cdot \dot{m} = w_i^{vap,s} \cdot \rho_{mix}^{vap,s} \cdot \dot{V}^{vap,s} + w_i^{liq,s} \cdot (\dot{m} - \rho_{mix}^{vap,s} \cdot \dot{V}^{vap,s}) \quad (46)$$

$$\dot{m}(w_i - w_i^{liq,s}) = \rho_{mix}^{vap,s} (w_i^{vap,s} \cdot \dot{V}^{vap,s} - w_i^{liq,s} \cdot \dot{V}^{vap,s}) \quad (47)$$

$$\rho_{mix}^{vap,s} = \frac{\dot{m}(w_i - w_i^{liq,s})}{\dot{V}^{vap,s} (w_i^{vap,s} - w_i^{liq,s})} \quad (48)$$

$$\rho_{mix}^{liq,s} = \frac{\dot{m}(w_i - w_i^{vap,s})}{\dot{V}^{liq,s} (w_i^{liq,s} - w_i^{vap,s})} \quad (49)$$

The total mass flow \dot{m} and the global composition w_i are computed by using liquid density correlations in order to convert the volume flows of the ISCO feeding pumps. These are for ethanol the Tait equation and for CO₂ the Wagner-Span EoS. The saturated weight compositions $w_i^{vap,s}$ and $w_i^{liq,s}$ could be experimentally determined (compare section 4.2.2) but are however in this study taken from the PR-EoS by considering a large experimental

VLE dataset. The only unknown variables are the volume flows of both saturated phases, or more precisely the bubble volume flow $\dot{V}^{vap,s}$ and the liquid segment volume flow $\dot{V}^{liq,s}$. The vapor bubble volume could be in theory optically determined by computing cylindrical bodies from the 2D pictures.

This is however prone to error, due to the change in the index of refraction of the media the light is passing through before it is collected by the CMOS chip, as well as due to the round shape of the microcapillary. The taken picture is thus optically distorted in the inner parts of the microcapillary. The 2D projections of the bubbles, are for instance expanded compared to the real unaffected projection.

As described earlier in 2.3, a bubble is in this work assumed to consist of two hemispherical caps and a middle cylindrical part. Furthermore, the liquid film that surrounds the vapor bubbles is neglected, since the film thickness is expected to be in the range of $< 1\mu\text{m}$. The sphere's diameter d_{sph} is identical to the inner diameter of the microcapillary, which is known from the manufacturer. The only geometrical information that are necessary in order to compute the bubble volume are thus the length of the bubble l_{bub} , the length of the unit cell l_{unit} and the outer diameter d_{out} of the microcapillary. The latter is not optically distorted and can be obtained from the information sheet given by the manufacturer. The bubble length l_{bub} can then be converted from pixels to meters. The calculations that lead to the bubble and liquid segment volumes are summarized by eqn. (50) and (51).

$$V^{vap,s} = V_{sph} + V_{cyl} = \frac{\pi}{6} \cdot d_{sph}^3 + \frac{\pi}{4} \cdot d_{sph}^2 \cdot (l_{bub} - d_{sph}) \quad (50)$$

$$V^{liq,s} = V_{unit} - V^{vap,s} = \frac{\pi}{4} \cdot d_{sph}^2 \cdot l_{unit} - V^{vap,s} \quad (51)$$

If the bubble frequency fr is accurately determined by the oscilloscope-coupled photo-detector (compare Figure 15), the volume flows can be obtained by equation (52).

$$\dot{V}^{vap,s} = V^{vap,s} \cdot fr; \dot{V}^{liq,s} = V^{liq,s} \cdot fr \quad (52)$$

The evaluation procedure was programmed in Matlab and consists in short of binarization, bubble and unit cell detection as well as length measurement and is briefly summarized in Figure 32. Therein the top left picture is taken from a segmented flow, while the top right picture is a blank picture (pure liquid ethanol inside capillary). The binarized pictures processed therefrom are shown below. In the case of the blank picture the central axis and

the capillary's outer diameter are found by selecting a region of interest for analysis (compare red circles in top right picture of Figure 32). For the pictures taken from the segmented flow the bubbles can be detected and the lengths of units and bubbles are being determined. By the equations introduced before $\rho_{mix}^{vap,s}$ and $\rho_{mix}^{liq,s}$ can be calculated.

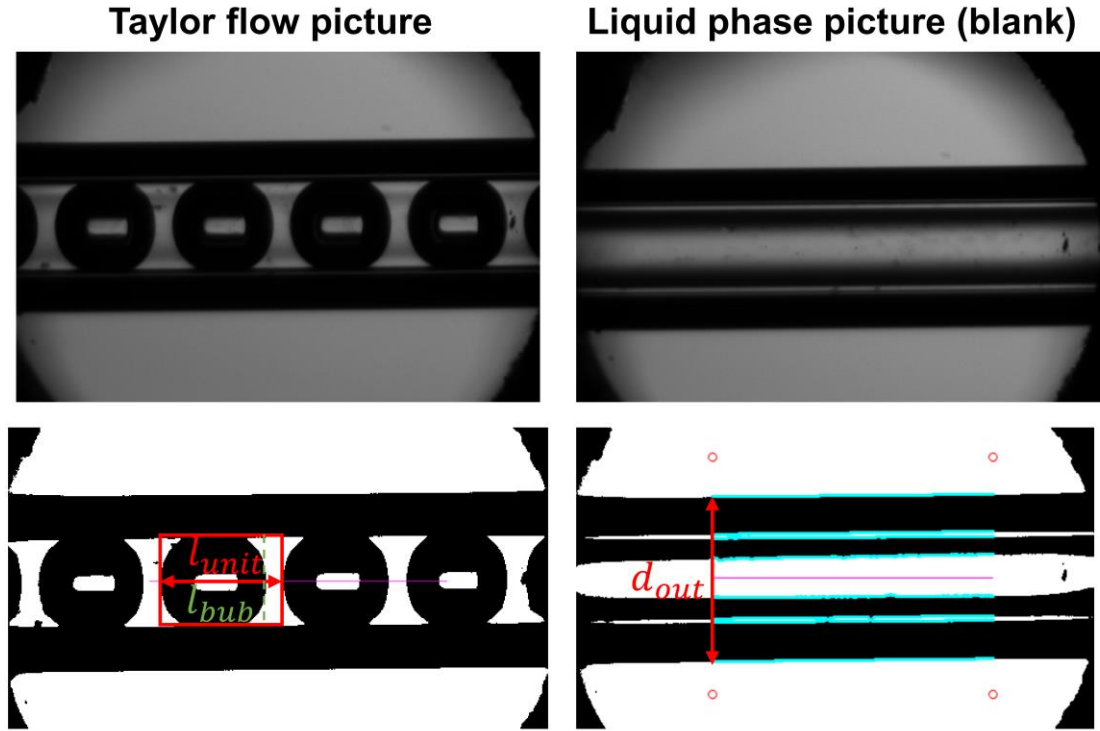


Figure 32: Evaluation procedure for the determination of mixture densities of ethanol/CO₂; the top left picture is taken from a segmented flow; the top right picture is from pure ethanol in the microcapillary

4.3 Deviation and measurement uncertainty

The experimentally obtained results can be compared to thermodynamic correlations or equations of state by the average absolute deviation *AAD*,

$$AAD(prop) = \frac{1}{np} \sum_{i=1}^{np} \left| \frac{prop_i^{exp} - prop_i^{lit}}{prop_i^{exp}} \right| \cdot 100 \% \quad (53)$$

$$AAD(prop) = \frac{1}{np} \sum_{l=1}^{np} \sum_{i=1}^{nc} \left| \frac{prop_{i,l}^{exp} - prop_{i,l}^{cal}}{prop_{i,l}^{exp}} \right| \cdot 0.5 \cdot 100 \% \quad (54)$$

wherein *prop* denotes the regarded experimentally obtained, calculated or in literature given thermodynamic property, *np* the number of data points and *nc* the number of compounds. Eqn. (53) regards hereby the *AAD* for a composition-independent property (e. g. p^s or H),

while eqn. (54) regards AAD for the saturated liquid or vapor phase. Regarding a single experimental point, eqn. (53) can be further derived to yield the absolute deviation AD for $np = 1$ in eqn. (e. g. p_{crit}, T_{crit}). The uncertainty of the experimental results in this work is furthermore evaluated by the guide to the expression of uncertainty in measurement (short: GUM) [144]. Due to the difference in measurements regarded, notes on how the uncertainties are calculated, are provided in the results sections.

5 Results and discussion

In this section the results are presented. These are for the majority only shown graphically. The main experimental data can be found in tabular form in the respective published works or in section 8. Each chapter starts with the section “materials and methods”, followed by the presentation of the experimental results, modeling and a discussion.

5.1 Saturated vapor pressure measurements

The here presented results and discussion are part of the recently published article in the Elsevier journal Fuel [116].

5.1.1 Materials and methods

The fuels that were used in the experiments are listed in Table 4. The main impurities of the OME_{3,4} are from other OME_n. Before every experimental run, the OME_{3,4} were degassed by vacuum-assisted pulsed sonication with a frequency of 0.3 Hz for 10 minutes before they were fed into the feed pump. The used fused silica microcapillary that is embedded in the microfluidic setup (described in detail in the measurement configuration in section 4.1) has the internal and external diameter of $d = \{300 \text{ and } 800\} \mu\text{m}$.

Table 4: Compounds with purities stated by the suppliers

compound	CAS	Supplier	Purity
ethanol for spectroscopy	64-17-5	Merck KGaA	> 99.9 % _w
1-octanol (spectro-photometric grade)	111-87-5	Riedel de Haen	> 99 % _w
OME ₃ (2,4,6,8-tetraoxanonane)	13353-03-2	ASG Analytik Service Gesellschaft	98.07 % _w
OME ₄ (2,4,6,8,10-pentaoxaundecane)	13352-75-5	ASG Analytik Service Gesellschaft	97.93 % _w

5.1.2 Results

Every carried out experimental run follows the experimental procedure provided in detail in section 4.2.1 The alcohols ethanol and 1-octanol are considered as validation compounds since the microfluidic setup has not been tested before for the determination of vapor pressure data. Pictures taken before, during and after condensation for the validation experiments with 1-octanol are provided by Figure 33.

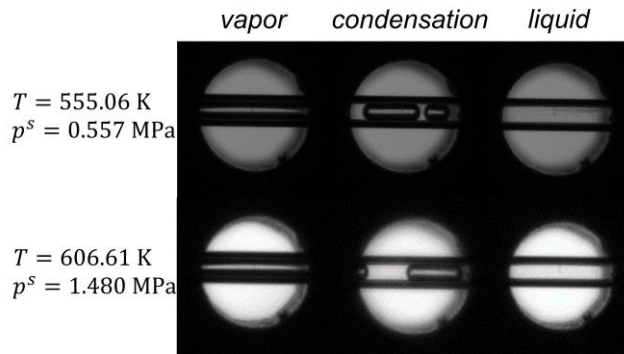


Figure 33: Experiments at two different temperatures with 1-octanol [116]

For ethanol a variety of vapor pressure data sets up to the critical point can be found in the archival literature [15,16,18,145]. For 1-octanol vapor pressures at temperatures between 500 K and T_{crit} were only reported by Ambrose et al. [15] ($T_{max} = 554$ K), as well as by Shakhverdiev et al. [146] ($T_{max} = 573.15$ K). The Chebyshev polynomial correlations provided by Ambrose et al. [15] are considered for comparison with the obtained experimental vapor pressure data (shown in Figure 34; tabulated data can be found in publication [116]) in terms of average absolute deviation (AAD) by eqn. (53).

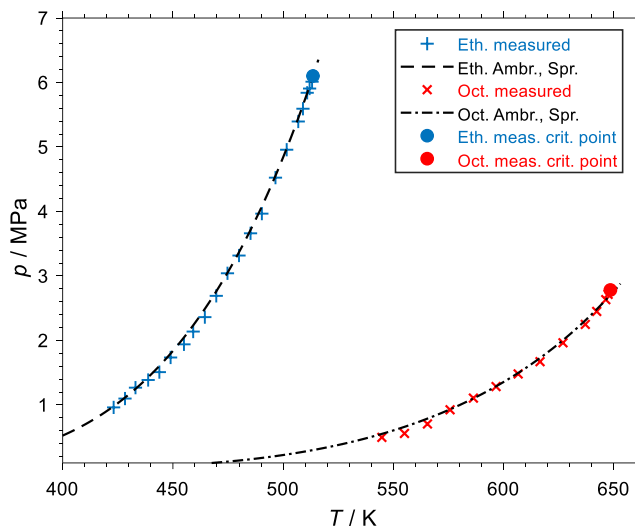


Figure 34: Measured vapor pressures and critical points of ethanol (Eth) and 1-octanol (Oct) compared to the Chebyshev polynomial correlations of Ambrose et al. [15] (Ambr., Spr.); [116]

For 1-octanol Ambrose's function was however only correlated to vapor pressure data up to 554 K and to T_{crit} . The AAD of the experimentally obtained vapor pressures is 2.1 % for ethanol and 4.1 % for 1-octanol. The critical temperatures and pressures that are found experimentally are furthermore compared to other literature data in Table 5, indicating relatively small absolute deviations (AD ; for $N = 1$ in eqn. (53)) for both T_{crit} and p_{crit} .

Table 5: Comparison of experimental critical temperature and pressure of ethanol and 1-octanol with literature data (AD : absolute deviation for the considered single data point) [116]

compound	p_{crit}^{exp} /MPa	T_{crit}^{exp} /K	p_{crit}^{lit} /MPa	T_{crit}^{lit} /K	$AD(p_{crit})$ / %	$AD(T_{crit})$ / %	reference
ethanol	6.101	513.54	6.148	513.92	0.77	0.07	Ambrose et al.[16]
“	“	“	6.14	514.1	0.64	0.11	Rosenthal and Teja[145]
“	“	“	6.17	515	1.13	0.28	Lydersen and Tsochev[18]
1-octanol	2.782	648.45	2.86	652.5	2.80	0.62	Ambrose et al.[16]
“	“	“	2.777	652.4	0.18	0.61	Rosenthal and Teja[145]
“	“	“	2.85	652.2	2.44	0.58	Quadri et al.[147]

The experimentally obtained vapor pressure data of the OME_n are visualized in Figure 35 and can be found in tabular form in the published article [116], as well as in section 8. There are visible deviations to the Antoine fit of Boyd [32] for both OME_3 and OME_4 , which indicates the potential error which can result from the extrapolation of vapor pressure curves that have been only fitted to data for temperatures up to the atmospheric boiling point. The force field data of Kulkarni et al. [33] supports the trend of the measured vapor pressures of OME_3 , but deviates from the here obtained experimental data of OME_4 . The critical points of both OME_3 and OME_4 could be however not reached, unlike in the validation experiments for ethanol and 1-octanol. This is due to the formation of a solid char-like substance which was found to be formed during experiments at $T > 605$ K for OME_3 and at $T > 610$ K for OME_4 and which might be a result of thermal decomposition and repolymerization. This substance plugged the microcapillary, which had to be replaced by a new capillary for further experimentation.

The vapor pressure data are fitted by the extended Antoine equation (compare fits in Figure 35 and see eqn. (31)), since the extended version tends to give more accurate correlations over a wide temperature range than the simple Antoine equation (would equal L_3 to $L_7 = 0$ in eqn. (31)). In order to achieve an appropriate fit for the full temperature range, the data of Boyd [32] were added to our experimental data. The AAD between fit and measured data (including Boyd's data) are 1.77 % (OME_3) and 1.58 % (OME_4). The obtained Antoine parameters are provided in Table 6.

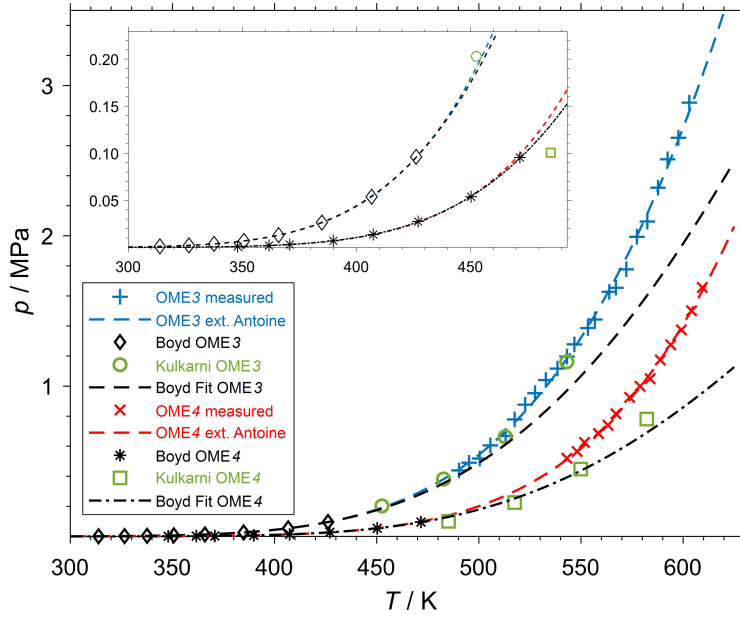


Figure 35: Measured vapor pressures and extended Antoine fits (fitted to both measured and Boyd’s data [32]); comparison with simulated data (Kulkarni [33]) and to an extrapolation of Boyd’s fits (only for illustration; validity up to atmospheric boiling temperatures) [116]

Table 6: Parameters of the extended Antoine equation for OME_n ; compare eqn. (31) and see plotted data in Figure 35

Compound	L_0	L_1	L_2	L_3
OME_3	-39.2943	-385.525	-190.729	-0.014676
OME_4	-21.1755	-969.144	-164.351	$-8.1936 \cdot 10^{-3}$
	L_4	L_5	L_6	
OME_3	15.136	-44.955	$-1.6671 \cdot 10^{-3}$	
OME_4	11.529	-42.749	$-1.4270 \cdot 10^{-4}$	

The molar latent heat of vaporization $\Delta_{\text{vap}}h$ of both OME_3 and OME_4 , are approximated by the equation of Clapeyron (see eqn. (29)). Therein the slope ($\frac{dp}{dT}$) and the molar volume of the saturated vapor phase ($v^{\text{vap},s}$) are computed with the Peng-Robinson EoS [115] by eqn. (14) to (19)). The molar volumes of the saturated liquid phase ($v^{\text{liq},s}$) are obtained by the Rackett, Spencer and Danner equation (RSD) that is given by eqn. (25).

The critical properties p_{crit} , T_{crit} and ω that are input values for the PR-EoS could not be determined experimentally as mentioned before. As a consequence, a numerical approach similar to the one introduced by Moine et al. [148] is used for the determination. Unlike in the publication of Moine et al. [148], where there are no boundaries for p_{crit} and T_{crit} , different group contribution methods (GC-methods) are regarded in order to obtain a possible range for the critical properties’ values by the predicted maxima and minima

values. The maxima and minima critical properties of all used GC-methods are underlined in Table 7.

Table 7: Critical properties predicted by different group contribution methods [116]

method	compound	T_{crit} / K	p_{crit} / MPa
Nannoolal et al. (Na) [149]	OME ₃	608.22	3.227
“	OME ₄	657.69	<u>2.878</u>
Joback and Reid (JR) [150]	OME ₃	605.87	3.206
“	OME ₄	649.97	2.832
Wilson and Jaspersen (WJ) [151]	OME ₃	606.99	<u>3.240</u>
“	OME ₄	652.81	2.843
Marrero and Pardillo (MP) [152]	OME ₃	<u>603.44</u>	3.114
“	OME ₄	<u>646.88</u>	2.701
Marrero and Gani (MG) [153]	OME ₃	612.61	<u>3.025</u>
“	OME ₄	649.16	<u>2.646</u>
Li et al. (Li) [154]	OME ₃	<u>614.73</u>	3.185
“	OME ₄	<u>659.70</u>	2.763

As visualized in Figure 36, T_{crit} and p_{crit} are directly iterated within these upper and lower extremes. The final critical properties (given in Table 8) are determined by comparing the vapor pressure line of the PR-EoS with the reference vapor pressure curve expressed by the extended Antoine equation in least-squares sense.

Group contribution methods in general depend on simple input information, such as the chemical structure and a few thermodynamic data points such as atmospheric boiling temperature. The here considered GC-methods can predict in acceptable accuracy the behavior of similar compounds such as mono-ethers, but there are to the author’s knowledge no available GC-methods that can predict accurately the behavior of poly-ethers such as OME_{*n*}. The straightforward approach of Burger et al. [26,27] (Marrero and Pardillo [152]) or of Li and Jia [155] (Joback), who predicted the critical points of OME_{*n*} solely by a randomly chosen method, can be considered critically.

With the determined critical temperatures T_{crit} the simplified RSD equation was adjusted to reproduce measured data, which was in the time of the publication unpublished, but which has been recently released by Beutler et al. [156]. The saturated liquid density $\rho^{liq,s}$ can be obtained by eqn. (12) using the molar masses of the OME_{*n*} ($M_{OME_3} = 0.13614$ kg mol⁻¹, $M_{OME_4} = 0.16617$ kg mol⁻¹).

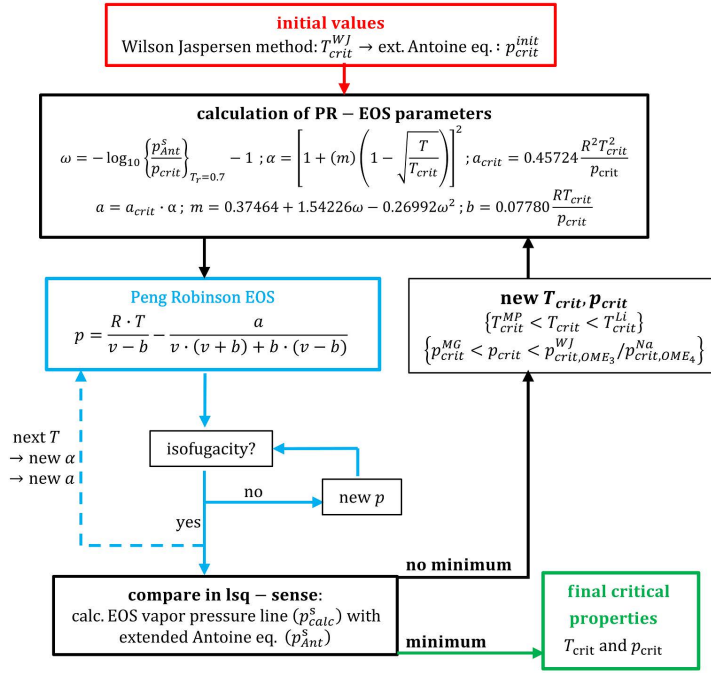


Figure 36: Estimation of the critical properties for OME₃ and OME₄ by least-squares-approach; use of GC-predicted values as boundaries [116]

Table 8: Final critical properties obtained by the approach visualized in Figure 36 [116]

compound	T_{crit}/K	p_{crit}/MPa	ω
OME ₃	609.00	3.083	0.5066
OME ₄	649.03	2.818	0.6589

Table 9: Adjusted parameters of the simplified RSD equation (compare eqn. (25)); the necessary critical temperature T_{crit} for the calculation of the reduced temperature T_r is taken from the by iteration obtained critical properties given in Table 8

compound	L_0	L_1	L_2
OME ₃	1642.24	3.9771	0.28571
OME ₄	1914.29	3.9221	0.28571

PR-EoS modifications such as a different α -function (e. g. of Stryjek and Vera [114,157,158]) were not used, in order not to affect $v^{vap,s}$ which is relevant for the Clapeyron equation. The fitted saturated liquid phase densities of the Rackett Spencer and Danner (RSD) equation, the measured liquid densities of Beutler et al. [156], the force-field simulated saturated vapor and liquid densities of Kulkarni et al. [33], as well as the saturated vapor phase PR-EoS densities are shown in Figure 37. The RSD equation gives almost identical results compared to an older correlation provided by Burger et al. [26,27] (not

shown for graphical clarity). Deviations in the shape of Kulkarni's simulated density data rows compared to the RSD and PR-EoS-curves can be seen.

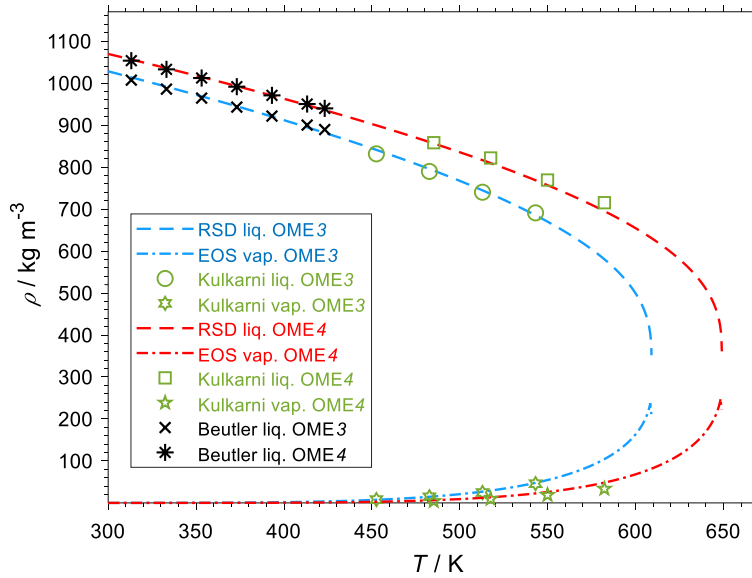


Figure 37: Saturated liquid and vapor phase densities of RSD equation and PR-EoS compared with data from Beutler et al. [156] and Kulkarni et al. [33] [116]

With all properties in the Clapeyron equation validated and defined, the latent heat of vaporization can be calculated. It has to be taken care however, that the Clapeyron-predicted heats of vaporization can be erroneous in the near-critical region. This can be avoided if $\Delta_{vap}h$ are fitted by the PPDS equation (here for $T_r < 0.975$), which then can be extrapolated up to T_{crit} . The by the PPDS equation (see eqn. (33) and (34)) obtained $\Delta_{vap}h$ are listed in Table 10 and shown in Figure 38 compared to extrapolated data of Boyd [32]. The PPDS equation reproduces the results of the Clapeyron equation exactly, with only a small difference in the temperature region for $T_r > 0.975$. [116]

Table 10: Fitted parameters of the PPDS latent heat of vaporization equation for both OME_n; T_{crit} for calculation of T_r from Table 8; compare eqn. (33) and (34)

Compound	L_0	L_1	L_2	L_3	L_4
OME ₃	6.5570	15.1778	-10.1624	-0.83436	14.6898
OME ₄	6.2838	21.6155	-16.8720	2.7104	11.7358

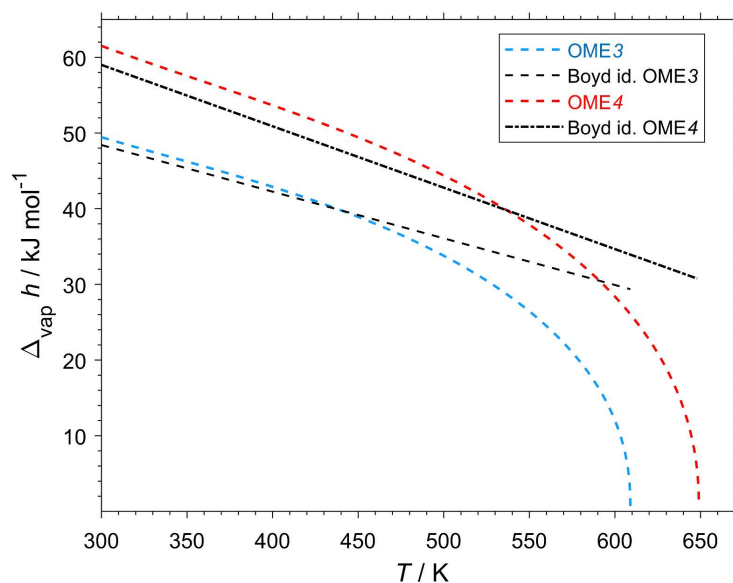


Figure 38: By PPDS equation computed latent heats of vaporization for OME₃ and OME₄ in comparison to extrapolated data of Boyd [32] [116]

5.1.3 Conclusion

Vapor pressures of OME₃ and OME₄ have been measured for the first time for temperatures exceeding the atmospheric boiling point. The Clapeyron equation was used to approximate the heats of vaporization of OME₃ and OME₄ up to the critical temperatures. Both properties are necessary input for spray modeling, as described earlier.

The microcapillary setup's capacity to measure accurately saturated vapor pressures has been tested and validated for the first time. Hereby the saturated vapor pressures and critical points of ethanol and 1-octanol could be precisely reproduced. The applied experimental method shows however the weakness that the vapor pressure cannot be measured by detecting the transition from liquid to vapor phase. This is due to boiling retardation, resulting from the liquid being at rest inside the microcapillary. The saturated vapor pressure measurements are furthermore limited to pressures significantly higher than one atmosphere (approximately $p > 0.4$ MPa). The standard uncertainties that were approximated by considering literature critical points of the validation compounds using the guide to the expression of uncertainty in measurement (GUM [144]), are at maximum $u(T) = 2.51$ K and $u(p) = 0.12$ MPa. This is less precise compared to setups, where the temperature is directly determined inside the vessel that contains the fluid. The latter is the case for classical pressure cell setups, as reported by Quadri et al. [147] and Rosenthal and Teja [145] for the critical temperature of 1-octanol ($u(T) = 0.6$ K in both studies).

Vapor pressure curves can be measured however up to the critical point as proven by the precise validation. An advantage of the described method lies in the small consumption of material, low experimentation time, as well as in the relatively precise measurement of system pressure. [116]

5.2 VLE measurements

The here presented results and discussions are part of the published articles [67,93,120] Regarding the full data sets including the combined standard uncertainties of the vapor/liquid equilibria in tabular form, the reader is also referred to section 8.

5.2.1 Materials and Methods

The chemicals that were used in the experiments are listed in Table 11. Prior to each experimental run, the fuel was degassed under pulsed sonication (frequency of 0.2 Hz; pulse duration of 0.5 s) for 5 minutes before it was sucked into the feed pump. In order to remove residual air from the feed pump, a small amount of the degassed fuel was fed through a valve-controlled bypass, located prior to valve 2 (compare Figure 15).

Table 11: Compounds/chemicals used for the VLE experiments; 1-octanol and ethanol from the identical suppliers were also used in vapor pressure studies (compare Table 4)

compound	CAS	Supplier	purity
1-octanol (spectro-photometric grade)	111-87-5	Riedel de Haen	> 99 % _w
ethanol for spectroscopy	64-17-5	Merck KGaA	> 99.9 % _w
nitrogen 5.0	7727-37-9	Nippon Gas	99.999 % _v
oxygen 5.0	7782-44-7	Nippon Gas	99.999 % _v
gas mix ^{*.a} (79.7 % _v O ₂ , 20.3 % _v N ₂)	7727-37-9, 7782-44-7	Nippon Gas	99.999 % _v
ethanol (for spectroscopy)	64-17-5	Merck KGaA	> 99.9 % _w
gas mix 1 ^{*.b} (20 % O ₂ , 80 % N ₂) [*]	7782-44-7 / 7727-37-9	Nippon Gas	> 99.999 % _v
gas mix 2 ^{*.b} (80 % O ₂ , 20 % N ₂) [*]	7782-44-7 / 7727-37-9	Nippon Gas	> 99.999 % _v
n-tridecane	629-50-5	Riedel de Haen	> 99 % _w
n-pentadecane	629-62-9	Riedel de Haen	> 99 % _w
n-hexadecane	544-76-3	Riedel de Haen	> 99 % _w
n-heptadecane	629-78-7	Riedel de Haen	> 99 % _w

*: the composition of the gas mix refers to a condition of 288.15 K and 0.1013 MPa; difference between volume and mole fractions is negligible; ^a: used for VLE study 1-octanol/N₂/O₂; ^b: used for VLE study ethanol/N₂/O₂

The used type of fused silica microcapillaries (Molex-Polymicro Technologies) has the internal and external diameter of {300 and 800} μm . The experimental procedure is in detail described in section 4.2.2.

5.2.2 Results

This section begins with the determination of the calibration constants K_{ij} , as discussed earlier in sections 3.3.2 and 4.2.2, followed by the presentation of the VLE results in phase diagrams that are shown together with modeled data from the regarded EoS and closes with the validation against available literature data. The critical properties and PC-SAFT parameters that are necessary model input, are given in Table 12 and Table 13.

Table 12: Critical properties necessary for PR-EoS

compound	T_{crit}/K	p_{crit}/MPa	ω	reference
1-octanol	652.5	2.777	0.5897	[159,160]
nitrogen	126.21	3.398	0.0369	[160]
oxygen	154.65	5.043	0.0213	[160]
ethanol	514.56	6.226	0.6430	[160]
n-tridecane	675.67	1.685	0.6006	[160]
n-pentadecane	722.39	1.448	0.7355	[160]
n-hexadecane	735.71	1.321	0.7500	[160]
n-heptadecane	722.39	1.448	0.7355	[160]

Table 13: PC-SAFT parameters

compound	m	$\sigma/10^{-10}\text{m}$	$\varepsilon/k_b/\text{K}$	$\varepsilon^{A_i B_i}/k_b/\text{K}$	$\kappa^{A_i B_i}$	reference
1-octanol	4.3555	3.7145	262.75	2754.8	$2.197 \cdot 10^{-3}$	[122]
nitrogen	1.2053	3.3130	90.96	-	-	[121]
oxygen	1.1217	3.210	114.96	-	-	[161]
n-tridecane	5.6877	3.9143	249.78	-	-	[121]
n-pentadecane	6.2855	3.9531	254.14	-	-	[121]
n-hexadecane	6.6485	3.9552	254.70	-	-	[121]
n-heptadecane	6.9809	3.9675	255.65	-	-	[121]

Calibration

In the case of ethanol/ N_2/O_2 the calibration measurements are performed inside the unsaturated vapor phase (for $p < p_{crit,eth}$) and the partially supercritical regime. For the 1-octanol/ N_2/O_2 study, as well as for the n-alkane/ N_2 systems, the critical loci are located at pressures that exceed those of ethanol/ N_2 or ethanol/ O_2 by far (compare sketch in Figure 23). Various temperatures, pressures and different precise global compositions were

however set throughout the calibration campaign of all studied systems. The calibration experiments for the ternary system ethanol/ N_2 / O_2 were carried out by feeding gas mix 1 (compare Table 11) through the left feed line and ethanol through the upper feed line. The molar flux of the gas can be obtained from the set mass flow of the MFC, while the feed volume flow of the ISCO 260 D can be converted using the Tait density correlation (compare eqn. (26) to (28)) of Cibulka and Zikova [162,163]. Since mole fractions across the full composition range could be set, the binary calibration constants were computed by the linear equation (36), with the linear fits having the forced interception of 0 (compare Figure 39).

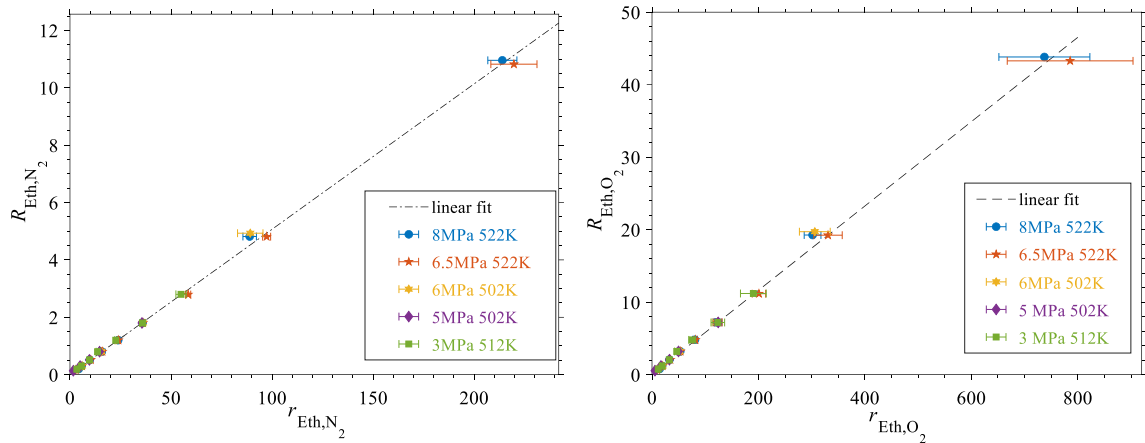


Figure 39: Calibration for ethanol/ N_2 (left diagram) and ethanol/ O_2 (right diagram) at different pressures and temperatures; obtained for experiments with system ethanol/gas mix 1 [93]

The binary calibration constants obtained from the fits shown in Figure 39 are given in Table 14. The constant K_{O_2,N_2} could be obtained by division of the two other calibration constants K_{eth,O_2} and K_{eth,N_2} according to eqn. (38). For this specific case however, a straight line with the intercept of 0 is fitted against the determined intensity ratios r_{O_2,N_2} that all match the same molar ratio of $R_{O_2,N_2} = 0.25$ (compare gas mix 1 in Table 11). By the following Figure 40, the evaluated signal ratios r_{O_2,N_2} are plotted vs. the mole fractions of ethanol that were set for the calibration experiments. With the decrease in the contents of N_2 and O_2 and with the increasing amount of ethanol in the unsaturated ternary mixture, only a slight change of r_{O_2,N_2} is visible. In respect of this figure, the described spectral evaluation procedure regarding the isolation of the O_2 -stretching vibration, can be considered accurate for the full composition range.

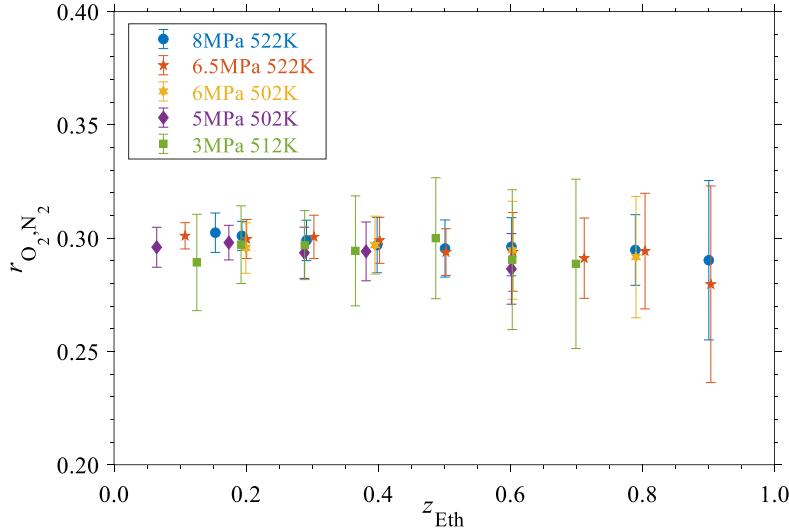


Figure 40: Determined signal ratios r_{O_2, N_2} vs. set ethanol mole fraction for calibration experiments of ethanol/gas mix 1

Table 14: Binary calibration constants found by linear fits for the studied ternary system ethanol/ N_2/O_2 [93]

i	j	K_{ij}
ethanol	oxygen	0.05816
ethanol	nitrogen	0.05067
oxygen	nitrogen	0.84737

The molar flux that is necessary for the calibration experiments, was obtained for 1-octanol as for ethanol by the Tait density correlation (compare eqn. (26) to (28)) of Cibulka and Zikova [162,163], while for the n-alkanes the same correlation with the parameters given in another work of Cibulka and Hnědkovský [164] was considered. Unlike ethanol, 1-octanol or the other n-alkanes, n-heptadecane was fed at $T = 303.15$ K due to its high atmospheric melting point of $T_{nC_{17}}^m(0.1013 \text{ MPa}) = 295.1$ K [165]. A correlation for the unsaturated liquid density of n-heptadecane covering the feeding temperature is however not given in the work of Cibulka and Hnědkovský [164]. As a consequence, a Tait correlation was obtained for the isotherm of $T = 303.15$ by considering available literature data of Bazile et al.[166], Luning Prak et al.[167], Brostow et al.[168], Würflinger et al.[169] and Audsley et al.[170]. The parameters obtained therefrom are provided in Table 15. The unsaturated liquid density is shown graphically in Figure 41. For the binary systems 1-octanol/ N_2 and 1-octanol/ O_2 , as well as for the n-alkane/ N_2 systems the nonlinear calibration approach according to eqn. (37) was chosen (compare right graphic in Figure 13), as a result that calibration measurements could not be carried out throughout the full composition range.

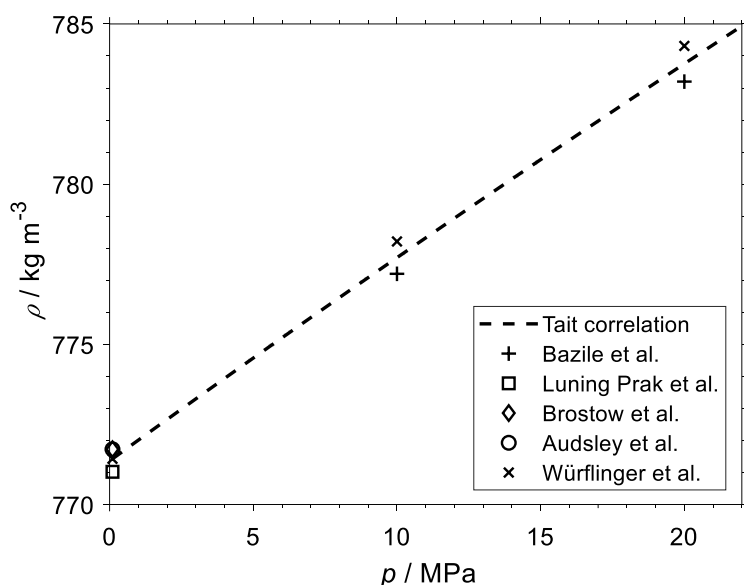


Figure 41: Adjusted Tait density correlation of n-heptadecane for the isotherm of $T = 303.15$ K; adjusted by considering available literature data [166–170]; [120]

Table 15: N-heptadecane Tait equation parameters, fitted for an isotherm of $T = 303.15$ (compare Figure 41); [120]

c_0	c_1	b_0	b_1	b_2	b_3	T_0
0.1249	-0.00035	101.43	-62.46	22.86	23.40	373.32

For the binary system 1-octanol/ O_2 , calibration results could not be obtained within the unsaturated vapor phase, due to repeatedly ignition and rupture of the microcapillary. In order to quantify the saturated liquid and vapor phase compositions for the 1-octanol/ O_2 system, the calibration factor was finally obtained by the division of K_{Oct,N_2} and K_{O_2,N_2} . The experimental calibration data that was measured and the respective fitted nonlinear calibration lines are presented in Figure 42. The results of the calibration for the binary systems 1-octanol/ N_2 and 1-octanol/ O_2 are given in Table 16. A scattering plot which is shown in Figure 43 indicates the goodness of the nonlinear calibration fits, by the small deviations between experimentally set and predicted (respectively calculated) N_2 mole fraction and furthermore by the given coefficients of determination R^2 .

The results for the binary n-alkane/ N_2 systems are only visualized in a scattering plot (see Figure 44), since the data points of the different systems and the calibration lines are visually only hardly differentiable. The calibration factors are given in Table 17 and are furthermore plotted against the chain length of the n-alkane in Figure 45. Hereby it is interesting to note, that a linear trend is visible.

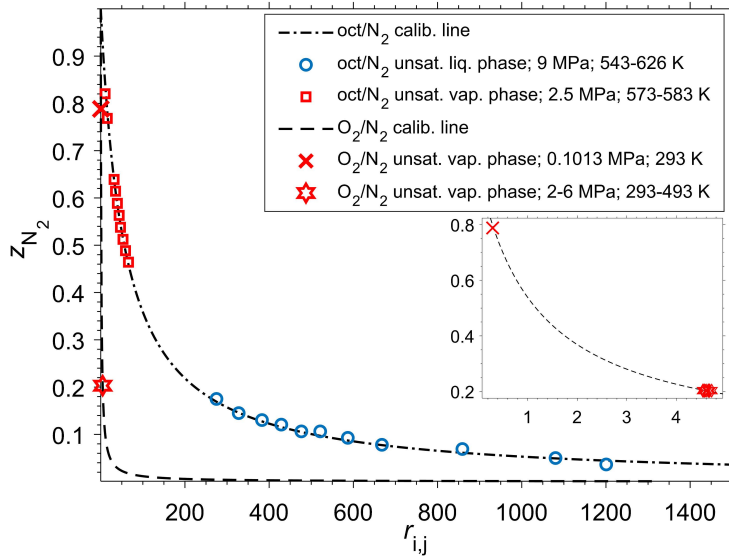


Figure 42: Calibration within unsaturated liquid and vapor phase regimes at various pressures and temperatures for the binary systems 1-octanol/ N_2 and O_2 / N_2 (furthermore given as zoom in the bottom right corner) [67]

Table 16: Calibration results for the binary systems 1-octanol/ N_2 and 1-octanol/ O_2

i	j	K_{ij}
1-octanol	nitrogen	0.01792
oxygen	nitrogen	0.85586
1-octanol	oxygen	0.02094

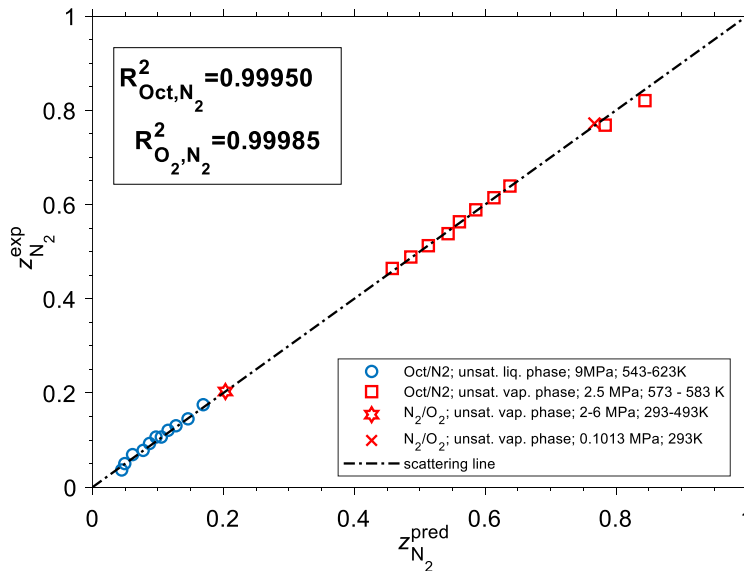


Figure 43: Scattering plot for the calibration of 1-octanol/ N_2 and O_2 / N_2 with coefficients of determination for predicted and experimental mole fractions of N_2 ; compare the calibration results in Figure 42 [67]

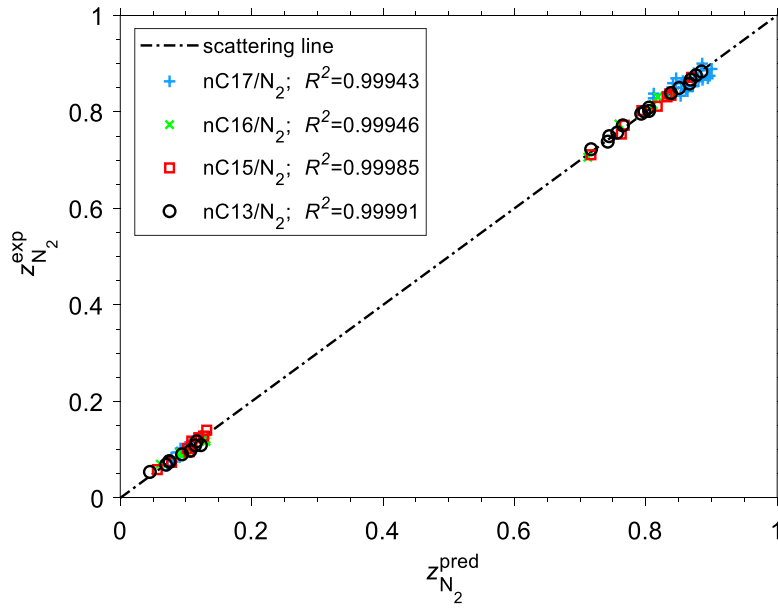


Figure 44: Calibration scattering plot for the binary n-alkane/N₂ systems; [120]

Table 17: Calibration results for binary n-alkane/N₂ systems (compare Figure 44)

i	j	K_{ij}
n-tridecane	nitrogen	0.01004
n-pentadecane	nitrogen	0.00900
n-hexadecane	nitrogen	0.08527
n-heptadecane	nitrogen	0.08001

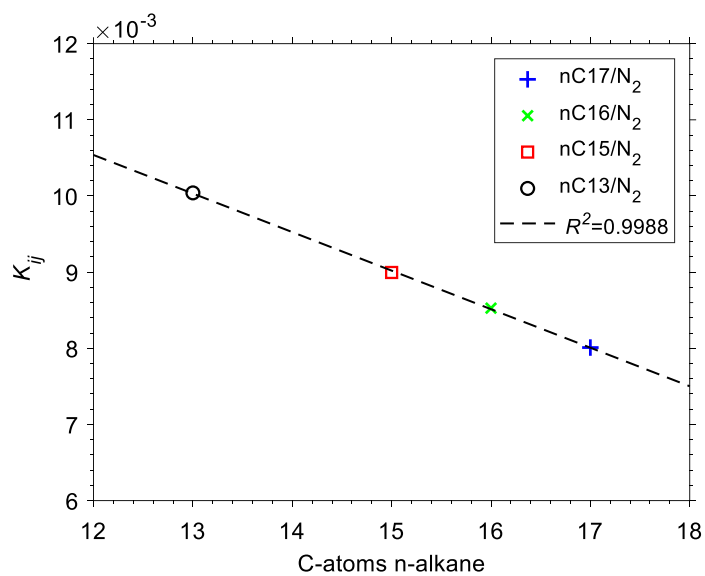


Figure 45: Linear fit of binary Raman calibration constants over number of carbon atoms in n-alkane [120]

VLE results and EoS modeling

With the calibration constants determined, the compositions of the saturated liquid and vapor phases can be calculated according to eqn. (36) for a binary system, or according to eqn. (39) and (40) in the case of a ternary system. For the VLE experiments of ethanol/N₂/O₂, ethanol was mixed with gas mix 1, gas mix 2 and with pure oxygen, meaning that two ternary systems and one binary system were studied. By including the measured data of Klima and Braeuer[60] for the binary system of ethanol/N₂, saturated liquid and vapor phase compositions along the full composition range for the system ethanol/N₂/O₂ could be obtained. Two types of ternary diagrams are shown as follows: with rising pressure along the isotherm of 423 K (see Figure 46) and for various temperatures along the isobar of 6.5 MPa (see Figure 47). A *Txy*-diagram of the binary system ethanol/O₂ is furthermore given in Figure 48.

When analyzing the ternary VLE diagrams in general, a higher solubility of O₂ compared to N₂ in the ethanol-rich liquid phase can be observed which tends to increase with rising pressure and temperature. The measured compositions of the saturated vapor phase show an increasing amount of ethanol with rising temperature and constant pressure, as well as a decreasing amount of ethanol with rising pressure at constant temperature. The ethanol mole fraction in the saturated vapor phase tends however to be almost unaffected by the gas. The dashed lines in Figure 46 and Figure 47 show the bubble and dew point curves calculated by the Peng-Robinson EoS with the classical α -function (compare eqn. (19)). For the regarded system ethanol/N₂/O₂, the binary interaction coefficients were considered to be dependent on temperature. As a consequence they are fitted against the isothermal data points by minimizing the bubble point pressures as shown by the objective function in eqn. (55). Interactions between N₂ and O₂ were not considered ($k_{ij} = 0$).

$$F_1 = \sum_{l=1}^{np} \left[\frac{p_l^{s,exp} - p_l^{s,cal}}{p_l^{s,exp}} \right]^2 \quad (55)$$

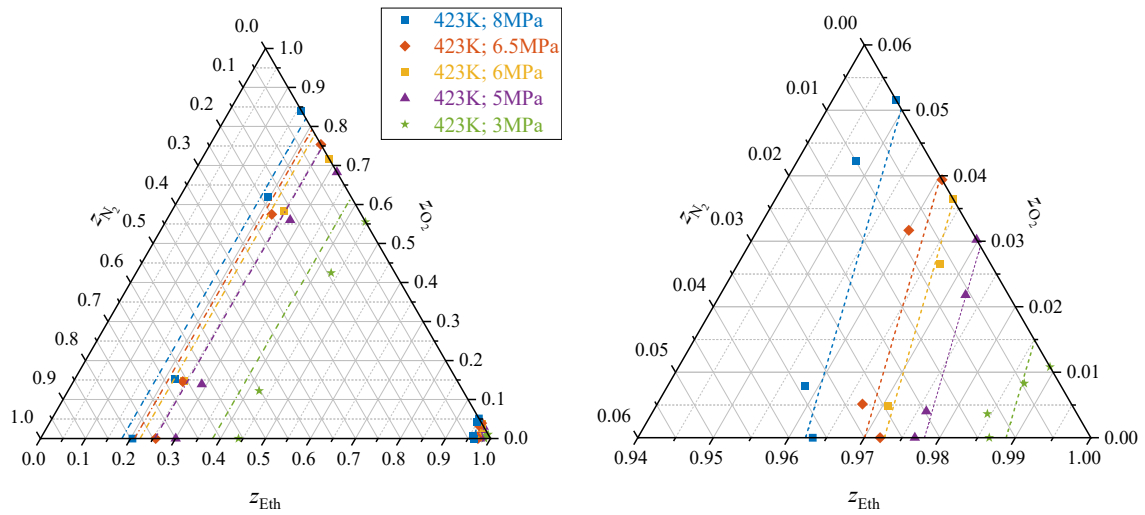


Figure 46: Ternary diagram of ethanol, oxygen and nitrogen (including data of Klima and Braeuer [60]) along the isotherm of $T = 423$ K and for various pressures (left); zoom into saturated liquid phase regime (right); dashed lines are from the PR-EoS [93]

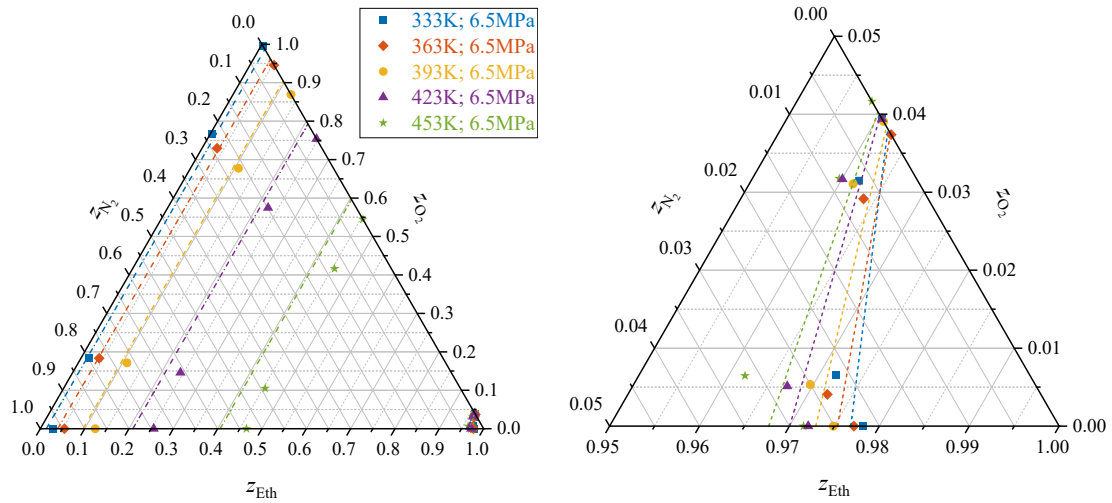


Figure 47: Ternary diagram of ethanol, oxygen and nitrogen (including data of Klima and Braeuer [60]) along the isobar of $p = 6.5$ MPa and for various temperatures (left); zoom into saturated liquid phase regime (right); dashed lines: PR-EoS with $k_{ij,Td}^{PR}$ [93]

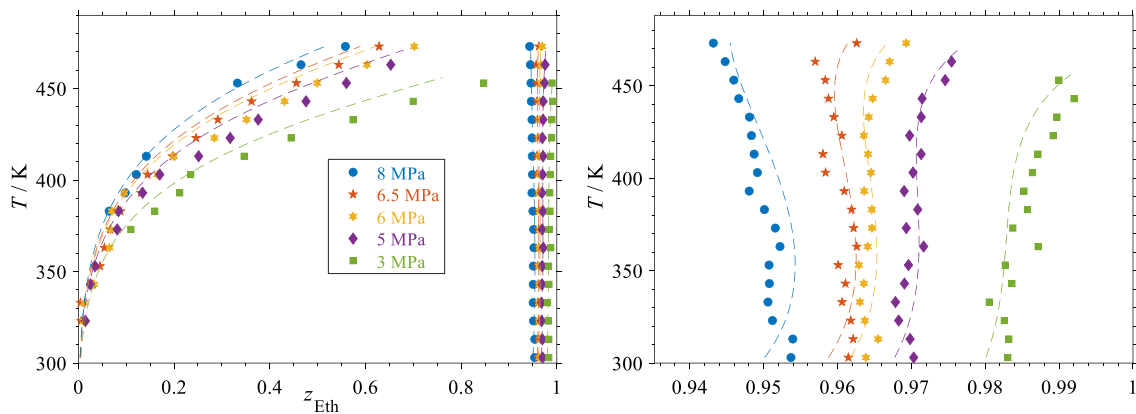


Figure 48: Txy -diagram of binary system ethanol/ O_2 ; several data points of the saturated vapor phase are left out compared to the publication [93], due to the reassessment of measurement uncertainty; dashed lines: PR-EoS with $k_{ij,Td}^{PR}$

The adjusted $k_{ij,Td}^{PR}$ can in return be fitted by straight lines for the binary systems ethanol/N₂ (data of Klima and Braeuer [60]) and ethanol/O₂. In eqn. (56) L_0 is the intercept and L_1 is the slope. The results of the fits are given in Table 18 and are shown in Figure 49.

Table 18: Intercepts, slopes and the coefficients of determination for the temperature dependents fits of the PR-EoS binary interaction coefficients [93]

i	j	R_{ij}^2	$L_{0,ij}^{PR}$	$L_{1,ij}^{PR}$
ethanol	oxygen	0.9841	-0.4830	$1.789 \cdot 10^{-3}$
ethanol	nitrogen	0.9587	-0.6562	$1.976 \cdot 10^{-3}$
oxygen	nitrogen	-	0	0

$$k_{ij,Td}^{PR} = L_{0,ij}^{PR} + L_{1,ij}^{PR} \cdot T \quad (56)$$

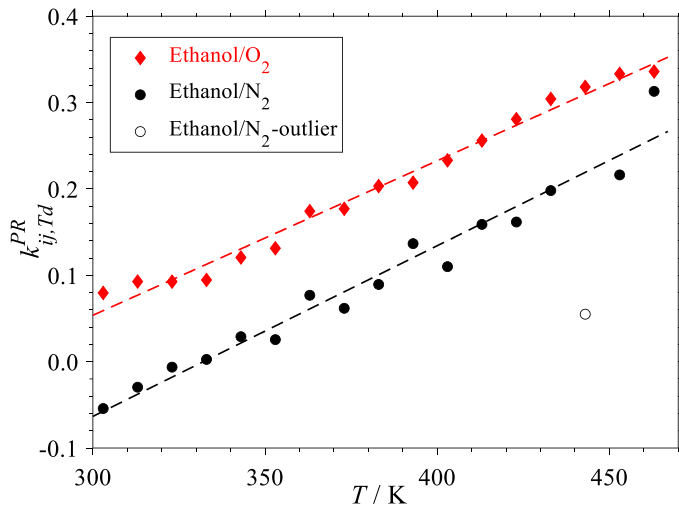


Figure 49: Fits of PR-EoS interaction coefficients for binary systems ethanol/O₂ and ethanol/N₂ [93]

When comparing the data of the model with the experimental results in terms of the AAD (see eqn. (54)) for the binary system ethanol/O₂, the PR-EoS is in the widest ranges in good agreement with the measured data. The temperature-dependent consideration yields hereby significantly better results in terms of AAD (compare Table 19) than the temperature-independent one with $k_{eth,O_2}^{PR} = 0.2001$.

Table 19: AAD between experimental results and PR-EoS with temperature-dependent and temperature-independent consideration (only data points are considered that are shown in Figure 48)

System	$AAD_{Td}^{PR}(y)/\%$	$AAD_{Td}^{PR}(x)/\%$	$AAD^{PR}(y)/\%$	$AAD^{PR}(x)/\%$
ethanol/O ₂	11.8	3.3	11.7	10.1

The VLE results of the two binary systems 1-octanol/ N_2 and 1-octanol/ O_2 are shown as follows in Txy -diagrams (see Figure 50 for 1-octanol/ N_2 and Figure 51 for 1-octanol/ O_2) and pxy -diagrams (see comparison between two binary systems in Figure 52). When comparing the two binary systems with each other the higher solubility of O_2 in the 1-octanol-rich liquid phase becomes obvious, while the saturated vapor phase compositions are however only hardly differentiable (as for the system ethanol/ N_2/O_2). Also, the beforementioned trends of rising N_2 - and O_2 - solubility with increasing system pressure and temperature are visible. The trend of a higher 1-octanol mole fraction in the saturated vapor phase with an increase in temperature is furthermore obvious, as a direct result of the increasing vapor pressure of 1-octanol. Modeled data of the PR-EoS and the PC-SAFT are moreover plotted in the diagrams shown in Figure 50, Figure 51 and Figure 52. For the PR-EoS, the classical α -function was used, as for the system ethanol/ N_2/O_2 .

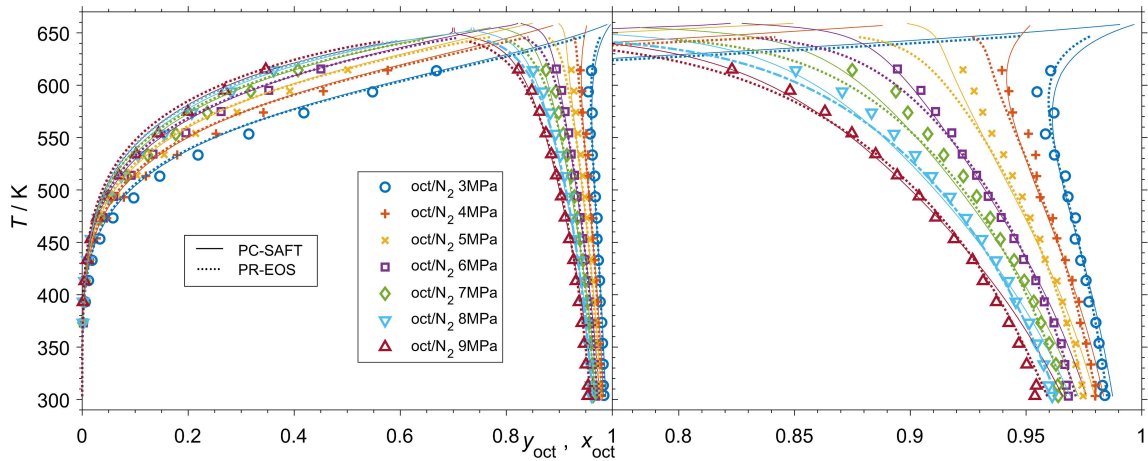


Figure 50: Txy -diagram of binary system 1-octanol/ N_2 with PC-SAFT with k_{ij}^{PCS} (continuous lines) and PR-EoS (dotted lines) with zoom of saturated liquid phase [67]

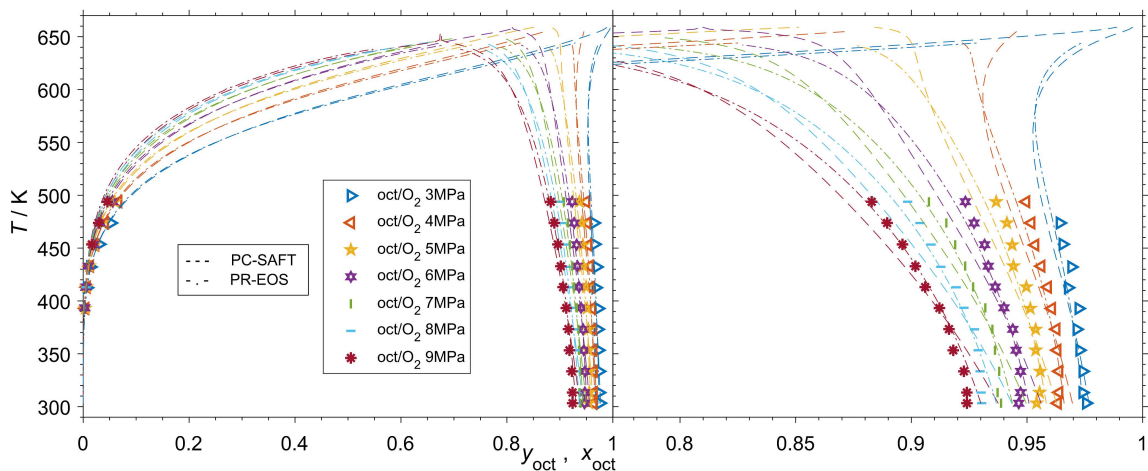


Figure 51: Txy -diagram of binary system 1-octanol/ O_2 with PC-SAFT with k_{ij}^{PCS} (dashed lines) and PR-EoS (dashed dotted lines) with zoom of saturated liquid phase [67]

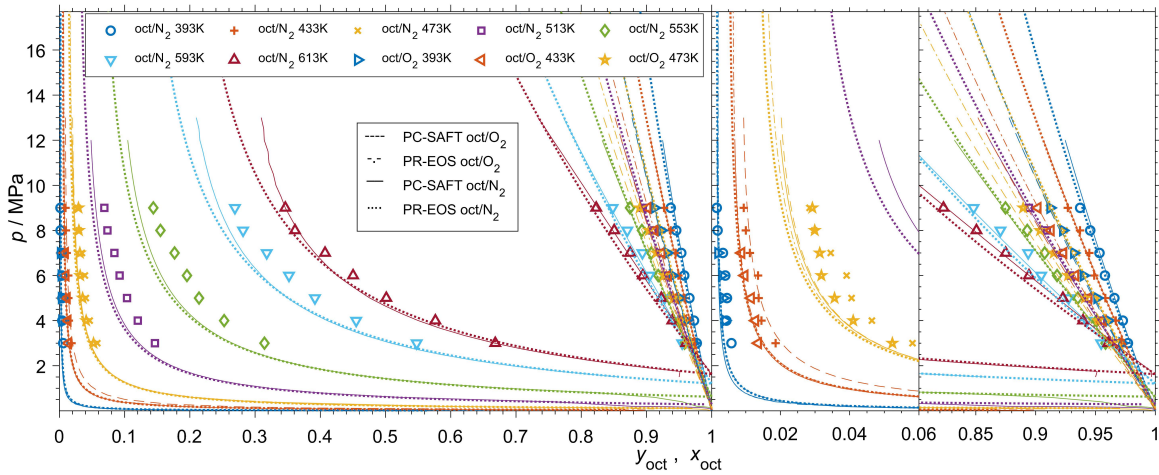


Figure 52: pxy -diagram (left graphic) and zoom of saturated vapor (middle) and liquid phases (right); comparison of 1-octanol/ N_2 and 1-octanol/ O_2 ; compare Figure 50 and Figure 51 [67]

The binary interaction coefficient was considered both, dependent as well as independent of temperature, when minimizing the objective function (57). Another objective function that was tested is given in eqn. (58), including the saturated vapor phase composition y . This 2nd term in eqn. (58) was however only considered for experimental points where vapor phase compositions could be measured (compare missing data points of saturated vapor phase in Figure 50 and Figure 51). F_3 leads logically to a lower $AAD(y)$, but the sum of $AAD(x)$ and $AAD(y)$ turns out to be higher compared to F_2 (compare definition of AAD in eqn. (54)). As a consequence, F_2 was chosen as the objective function.

$$F_2 = \sum_{l=1}^{np} \sum_{i=1}^{nc} \left[\frac{x_{i,l}^{exp} - x_{i,l}^{cal}}{x_{i,l}^{exp}} \right]^2 \quad (57)$$

$$F_2 = \sum_{l=1}^{np} \sum_{i=1}^{nc} \left[\frac{x_{i,l}^{exp} - x_{i,l}^{cal}}{x_{i,l}^{exp}} \right]^2 + \left[\frac{y_{i,l}^{exp} - y_{i,l}^{cal}}{y_{i,l}^{exp}} \right]^2 \quad (58)$$

The temperature-dependent fit yields moreover only a slightly enhanced model accuracy for both the PC-SAFT and the PR-EoS. This is why in the diagrams shown above (Figure 50, Figure 51 and Figure 52), only modeled data are plotted that are obtained by using the temperature-independent k_{ij} . In the following the final temperature-independent k_{ij} are listed in Table 20, with the AAD given in Table 21. The 3rd-order polynomial parameters (compare eqn. (59)) of the temperature-dependent k_{ij} are given for completeness in Table 22, while the corresponding AAD are provided in Table 23.

Table 20: Obtained temperature-independent PR-EoS and PC-SAFT binary interaction coefficients of the binary systems 1-octanol/N₂ and 1-octanol/O₂ [67]

System	k_{ij}^{PCS}	k_{ij}^{PR}
1-octanol/N ₂	0.1551	0.2943
1-octanol/O ₂	0.1681	0.2936

Table 21: AAD of temperature-independent consideration of k_{ij} for binary systems 1-octanol/N₂ and 1-octanol/O₂ [67]

System	$AAD^{PCS}(y)/\%$	$AAD^{PCS}(x)/\%$	$AAD^{PR}(y)/\%$	$AAD^{PR}(x)/\%$
1-octanol/N ₂	8.85	3.23	9.53	2.04
1-octanol/O ₂	6.32	4.23	6.74	1.95

$$k_{ij,Td} = L_3 \cdot \frac{T^3}{T_0^3} + L_2 \cdot \frac{T^2}{T_0^2} + L_1 \cdot \frac{T}{T_0} + L_0 \quad (59)$$

Table 22: 3rd order polynomial parameters for the description of temperature-dependent binary interaction coefficients for binary systems 1-octanol/N₂ and 1-octanol/O₂ [67]

system	L_0^{PCS}	L_1^{PCS}	L_2^{PCS}	L_3^{PCS}
1-octanol/N ₂	$-2.4709 \cdot 10^{-3}$	$2.8664 \cdot 10^{-4}$	$6.8094 \cdot 10^{-7}$	$-1.1313 \cdot 10^{-9}$
1-octanol/O ₂	-0.23407	$2.1572 \cdot 10^{-3}$	$-3.8797 \cdot 10^{-6}$	$2.7181 \cdot 10^{-9}$
	L_0^{PR}	L_1^{PR}	L_2^{PR}	L_3^{PR}
1-octanol/N ₂	-1.1438	0.010444	$-2.5257 \cdot 10^{-5}$	$2.0404 \cdot 10^{-8}$
1-octanol/O ₂	-1.0817	$9.9136 \cdot 10^{-3}$	$-2.4060 \cdot 10^{-5}$	$1.9871 \cdot 10^{-8}$

Table 23: AAD of temperature-dependent consideration of k_{ij} for binary systems 1-octanol/N₂ and 1-octanol/O₂ [67]

system	$AAD_{Td}^{PCS}(y)/\%$	$AAD_{Td}^{PCS}(x)/\%$	$AAD_{Td}^{PR}(y)/\%$	$AAD_{Td}^{PR}(x)/\%$
1-octanol/N ₂	8.97	1.38	9.77	1.35
1-octanol/O ₂	7.19	1.21	7.20	1.08

Last but not least the VLE data of the n-alkane/N₂ systems are presented as Txy -diagrams in Figure 53 and a comparison between the different systems is provided in Figure 54. When comparing the bubble point curves of the different binary systems, hardly any differences of the N₂-solubility can be observed. The binary systems are however clearly differentiable by their saturated vapor phase compositions, as a result of the decreasing volatility of n-alkanes with rising chain length.

In the phase diagrams shown here the solely predictive Peng-Robinson EoS with a temperature dependent interaction coefficient (PPR78) is used. The differences of the model

which has been introduced by Jaubert, Mutelet and Privat [117,118], compared to the original PR-EoS are discussed in section 3.1.2 (compare eqn. (20)). The binary interaction coefficients of the PC-SAFT are obtained analog as for the systems 1-octanol/ N_2 and 1-octanol/ O_2 by minimizing the objective function F_2 given in eqn. (57).

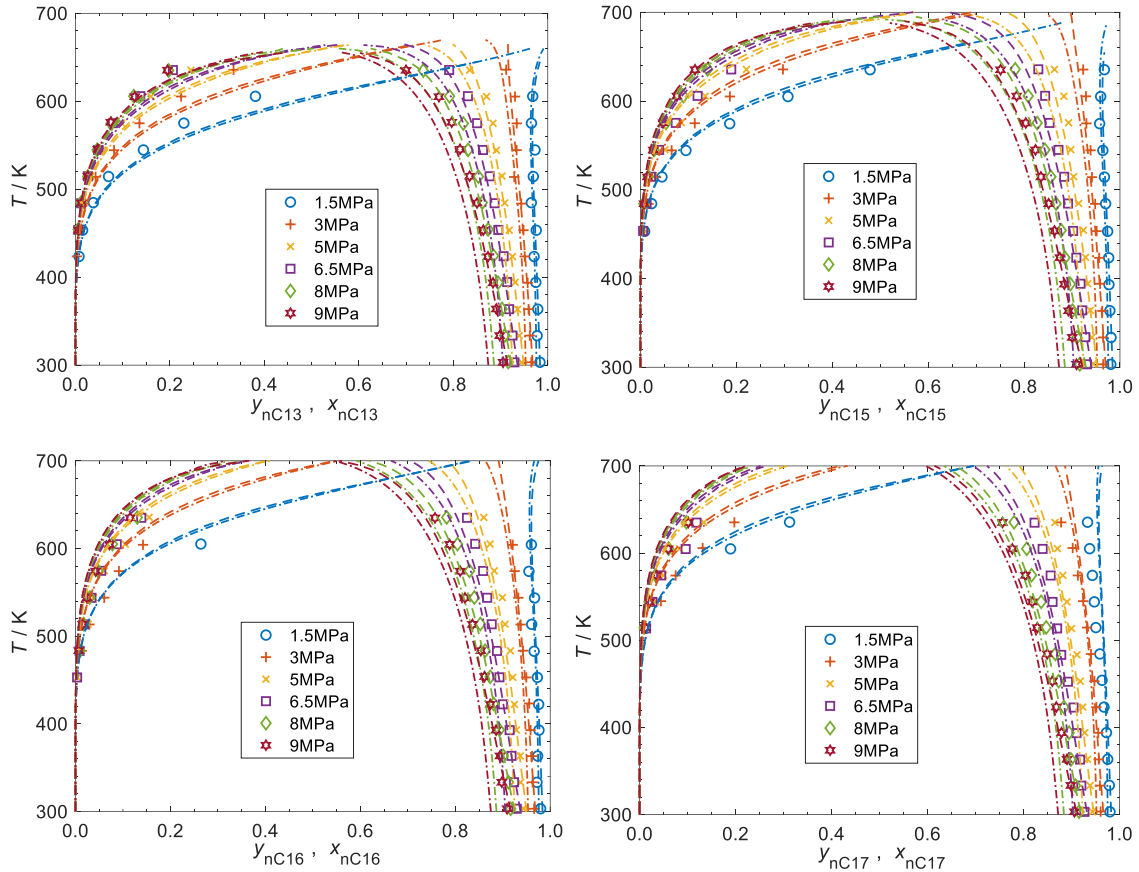


Figure 53: Txy -diagrams of the regarded binary n-alkane/ N_2 systems; PPR78: dashed-dotted lines; PC-SAFT with k_{ij}^{PCS} : dashed lines; [120]

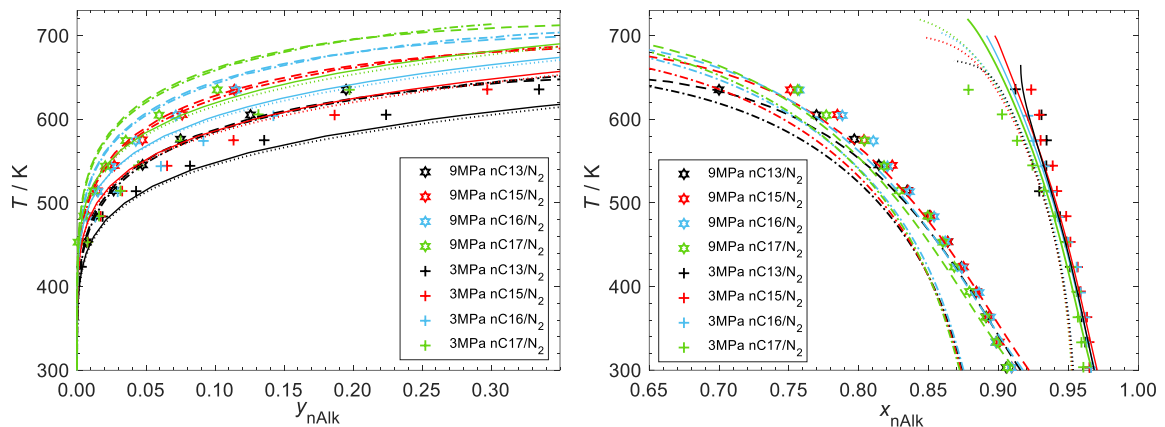


Figure 54: Txy -diagrams for comparison between different n-alkane/ N_2 systems; PPR78 at 3MPa dotted lines and at 9 MPa dashed-dotted lines, PC-SAFT with k_{ij}^{PCS} at 3 MPa continuous lines and at 9 MPa dashed lines; [120]

The results are also given in Table 24. Therein are also listed the polynomial parameters for the calculation of $k_{ij,Td}^{PCS}$, that are however not relevant for the n-alkane/N₂ phase diagrams.

The AAD between model and experimental data are given in

Table 25.

Table 24: Binary interaction of PC-SAFT for n-alkane/N₂ systems; temperature-dependent parameters for computation of $k_{ij,Td}^{PCS}$ (compare eqn. (59)) and temperature-independent k_{ij}^{PCS} obtained from minimizing F_2 in eqn. (57)

system	k_{ij}^{PCS}	$L_{ij,0}^{PCS}$	$L_{ij,1}^{PCS}$	$L_{ij,2}^{PCS}$	$L_{ij,3}^{PCS}$
n-tridecane/N ₂	0.1782	-0.0458	$1.411 \cdot 10^{-3}$	$-3.167 \cdot 10^{-6}$	$2.596 \cdot 10^{-9}$
n-pentadecane/N ₂	0.1963	-0.0582	$4.987 \cdot 10^{-3}$	$-1.064 \cdot 10^{-5}$	$7.678 \cdot 10^{-9}$
n-hexadecane/N ₂	0.1872	-0.3536	$3.371 \cdot 10^{-3}$	$-7.019 \cdot 10^{-6}$	$5.003 \cdot 10^{-9}$
n-heptadecane/N ₂	0.1784	-0.4726	$4.198 \cdot 10^{-3}$	$-8.748 \cdot 10^{-6}$	$5.944 \cdot 10^{-9}$

Table 25: AAD between models (PPR78 and PC-SAFT) and experimental data for regarded binary n-alkane/N₂ systems

system	AAD_{Td}^{PCS}	AAD_{Td}^{PCS}	AAD^{PCS}	AAD^{PCS}	AAD_{Td}^{PR}	AAD_{Td}^{PR}
	(x)/%	(y)/%	(x)/%	(y)/%	(x)/%	(y)/%
n-tridecane/N ₂	1.75	6.08	2.52	6.57	9.06	9.22
n-pentadecane/N ₂	1.44	15.20	3.02	14.63	11.04	12.36
n-hexadecane/N ₂	1.97	21.11	3.00	20.59	8.25	19.30
n-heptadecane/N ₂	3.69	19.87	4.13	19.82	7.98	17.97

Validation

Since no comparable VLE data for the ternary system ethanol/N₂/O₂ or the binary system ethanol/O₂ are available in the archival literature, Henry coefficients from the works of Schnabel et al. [61] (adjusted and predictive modes) and Malviya et al. [62] were regarded for validation (compare Table 1). The literature data are shown in Figure 55 together with the Henry coefficients obtained in this work by eqn. (24), for which the PR-EoS using the fitted $k_{ij,Td}^{PR}$ was applied. When comparing the obtained Henry coefficients with the literature data, generally good agreement can be seen, with the biggest deviation in the lower temperature range. As it can be seen by the right diagram of Figure 56, the obtained saturated liquid phase data for the binary system of 1-octanol/N₂ show good agreement with the experimental data of Weng et al. [65], while the data of Lu et al. [66] tend to diverge from Weng's and the here obtained data. Good agreement can be also seen for the saturated vapor phase compositions (left diagram of Figure 56), where two isotherms can be compared with the data of Weng et al.

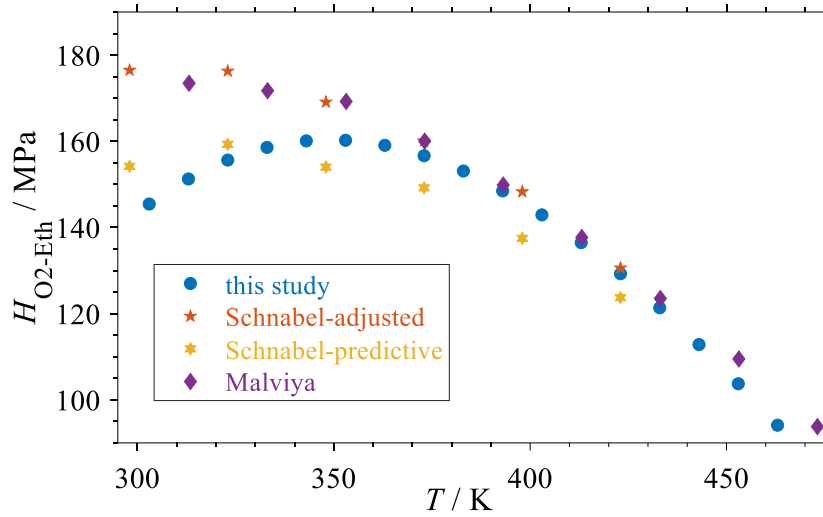


Figure 55: Comparison of the Henry coefficients for the binary system ethanol/O₂ with literature data from the works of Schnabel et al. [61] and Malviya et al. [62]; [93]

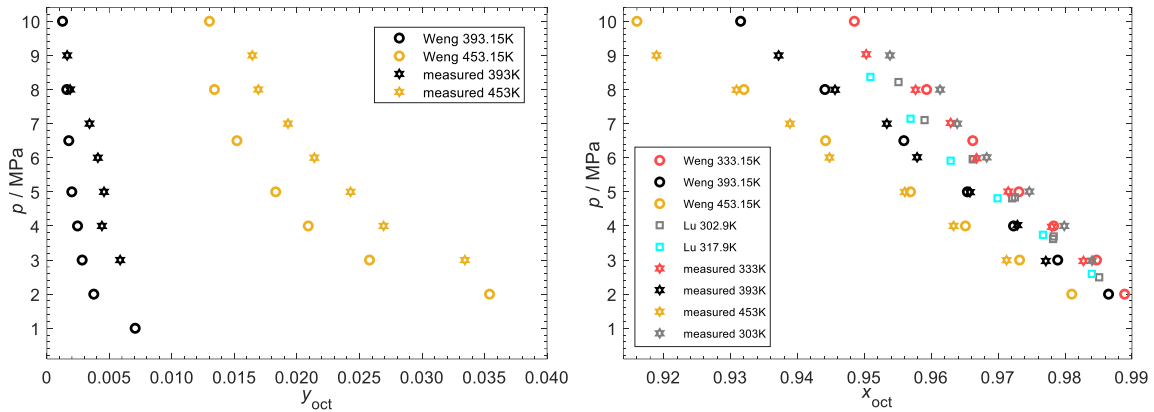


Figure 56: Validation of VLE data for binary system 1-octanol/N₂ with available literature data of Weng et al. [65] and Lu et al. [66]; [67]

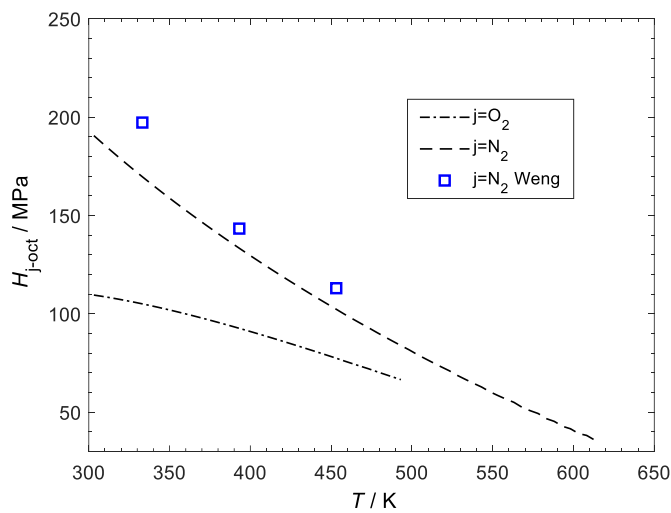


Figure 57: Henry's law coefficients obtained by the PR-EoS in comparison with the data published by Weng et al. [65]; [67]

Henry’s law coefficients for the binary system 1-octanol/N₂ are also in good agreement with Henry’s law coefficients given by Weng et al. [65] (obtained by the Krichevsky-Ilinskaya equation [171]; see Figure 57). Figure 57 indicates further the beforementioned higher solubility of O₂ compared to N₂ in the 1-octanol-rich liquid phase.

The experimentally obtained VLE data of the binary system n-hexadecane/N₂ are compared to literature data of three publications in Figure 58. As stated earlier for the other binary systems, the obtained data for n-hexadecane/N₂ agree also well with the available literature data. PC-SAFT modeling for the binary system n-hexadecane/N₂ has been also done by Madani et al. [172], Rowane et al. [34] and García-Sánchez et al. [173]. Madani et al.[172] do however not tabulate any k_{ij}^{PCS} obtained by a machine-learning algorithm, while the k_{ij}^{PCS} of Rowane et al.[34] is not comparable to our fitted k_{ij}^{PCS} , since the pure compound parameters m, σ and ε stem from a group contribution method. García-Sánchez et al.[173] included the VLE data of only Lin et al.[68] for their fit. They report values of $k_{ij}^{PCS} = 0.1816$ and $k_{ij}^{PCS} = 0.1860$, obtained by two different objective functions. Those are well comparable to the obtained $k_{ij}^{PCS} = 0.1872$ of this study. [120]

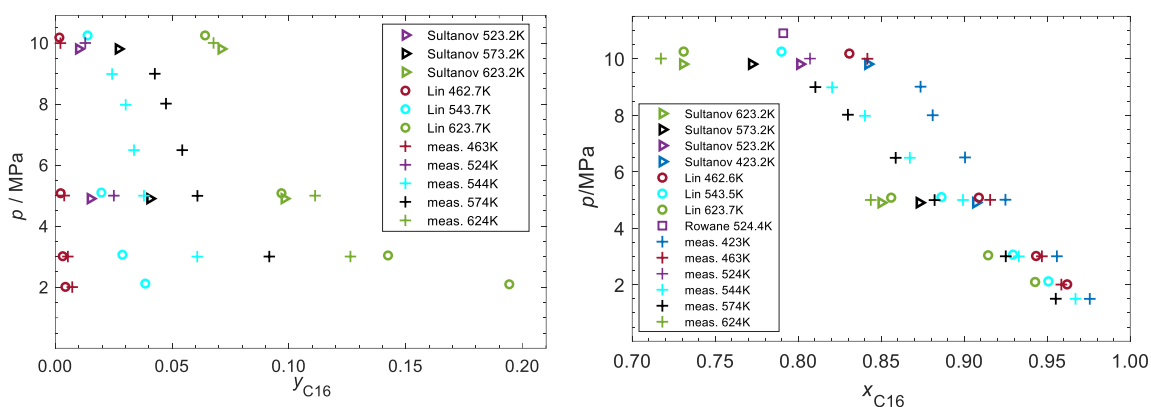


Figure 58: Validation of VLE data for binary system n-hexadecane/N₂ with available literature data [34,68,69]; [120]

Uncertainties

As stated earlier, the guide to the expression of uncertainty in measurement (GUM) was considered, in order to determine combined standard uncertainties of the experimentally obtained equilibrium molar compositions z . “Type a” uncertainties stem from measurement repetitions, while “type b” uncertainties are measurement uncertainties of the used measurement devices (and which don’t have a repetitive character). Among other uncertainties, contributions from the measurement of pressure and temperature are included. The combined pressure uncertainty ($u_c(p)$; see eqn. (60)) combines the uncertainty interval

of the device ($u_b(p) = 0.05\% \cdot p$; Keller PA-33x) with the deviation between set and measured pressure ($u_a(p)$). The combined temperature uncertainty ($u_c(T)$; see eqn.(60)) includes the manufacturer's uncertainty ($u_b(T) = 0.1\text{K} + 0.0017 \cdot T$) and the standard deviation of the temperature values that come from 4 different PT-100 resists ($u_a(T)$). For the VLE study of ethanol/N₂/O₂ type K thermocouples were used instead of PT-100 resists ($u_b(T) = 1.1\text{K}$ or $u_b(T) = 0.4\% \cdot T$; whatever is greater) and the pressure was measured by the pressure transducer of the Isco reverse pump ($u_b(p) = 0.5\% \cdot p$).

$$u_c(p) = \sqrt{(u_a(p))^2 + (u_b(p))^2} ; u_c(T) = \sqrt{(u_a(T))^2 + (u_b(T))^2} \quad (60)$$

In order to state databank-requested combined uncertainties in the unit of the experimental result ($\text{mol} \cdot \text{mol}^{-1}$), the partial derivatives $\left(\frac{\partial z}{\partial T}\right)_p$ and $\left(\frac{\partial z}{\partial p}\right)_T$ were determined numerically by using the Peng-Robinson EoS (using k_{ij}^{PR} in publication [67]) and the PPR78 (in publication [120]). The combined uncertainties of temperature $u_{c,T}(z)$ and pressure $u_{c,p}(z)$ in the unit of $\text{mol} \cdot \text{mol}^{-1}$ can then be obtained by a Gaussian-type error propagation (see following eqn. (61)).

$$u_{c,p}(z) = \left(\frac{\partial z}{\partial p}\right)_T \cdot u_c(p); u_{c,T}(z) = \left(\frac{\partial z}{\partial T}\right)_p \cdot u_c(T) \quad (61)$$

Uncertainties of the Raman analysis are also included. In detail from the calibration ($u_{a,cal}(z)$), by regarding the standard deviation of all differences between experimental and predicted values (compare validation section; e. g. Figure 44) as well as from the combined uncertainty regarding the Raman measurement and spectral evaluation at each experimental point ($u_{c,rep}(z)$). The latter can be obtained by eqn. (62). Therein $u_{a,sing}$ is the standard deviation of the 32 mole fractions of the single spectra obtained at each experimental point. $u_{a,glob}$ marks the averaged standard deviation of global experimental repetitions performed for various temperatures and pressures of 3 MPa and 9 MPa for the VLE study of the 1-octanol/N₂ system. For $u_{a,sing}$ a weight μ is included, that was found by comparing $u_{a,sing}$ with $u_{a,glob}$ at the same pressure and temperature conditions. Therefrom it could be derived that on average 5.2 single spectra are representative for the liquid phase ($\mu_{liq} = 0.19$), while 8.3 single spectra are representative for the vapor phase ($\mu_{vap} = 0.12$).

$$u_{c,rep}(z) = \sqrt{\left(\mu \cdot u_{a,sing}(z)\right)^2 + \left(u_{a,glob}(z)\right)^2} \quad (62)$$

By the calculated uncertainties $u_{c,p}(z)$, $u_{c,T}(z)$, $u_{a,cal}(z)$ and $u_{c,rep}(z)$ the final combined standard uncertainties $u_c(z)$ can be obtained by eqn. (63) as the root-sum of different squared uncertainties. This principle of calculating combined standard uncertainties is also used in other methods, such as in the guidelines for evaluating and expressing the uncertainty of NIST measurement results [174]. In eqn. (63) z stands for the saturated liquid or vapor phase mole fraction.

$$u_c(z) = \sqrt{(u_{c,p}(z))^2 + (u_{c,T}(z))^2 + (u_{a,cal}(z))^2 + (u_{c,rep}(z))^2} \quad (63)$$

For the precise values of $u_c(z)$ per measurement point, the reader is referred to the publications [67,120]. The uncertainties for the VLE study of ethanol/O₂ [93] were however reassessed for this thesis and the maxima and minima obtained therefrom are included in Table 26.

Table 26: minima and maxima combined uncertainties of temperature, pressure and saturated liquid x_i and vapor phase mole fractions y_i ; obtained by the uncertainty evaluation for different fuel(*i*)/gas systems

system	$u_c(T)/K$	$u_c(p)/kPa$	$u_c(x_i)/\text{mol} \cdot \text{mol}^{-1}$	$u_c(y_i)/\text{mol} \cdot \text{mol}^{-1}$
n-tridecane/N ₂	0.62–2.28	0.77–8.15	0.0036–0.0078	0.0046–0.0716
n-pentadecane/N ₂	0.63–2.26	1.10–9.72	0.0036–0.0065	0.0048–0.0668
n-hexadecane/N ₂	0.62–2.13	0.90–22.16	0.0037–0.0121	0.0055–0.0692
n-heptadecane/N ₂	0.62–2.28	0.75–7.72	0.0036–0.0140	0.0076–0.0802
1-octanol/N ₂	0.63–1.95	2.00–20.40	0.0028–0.0046	0.0030–0.0273
1-octanol/O ₂	0.63–1.43	2.24–31.14	0.0028–0.0045	0.0028–0.0034
ethanol/O ₂	1.36–1.98	29.15–47.17	0.0010–0.0016	0.0078–0.0452

5.2.3 Conclusion

In this section, VLE data that were obtained experimentally by the microcapillary setup were presented. Calibration measurements were performed, in order to obtain the final saturated liquid and saturated vapor phase compositions. The PR-EoS and PC-SAFT were used to model the VLE. Good agreement was generally found between experimental results and model data using fitted temperature-dependent or temperature-independent binary interaction coefficients, as well as data available from the literature. During the spectral evaluation procedure (compare 4.2.2), the earlier introduced correction methods regarding

the liquid film contribution, were applied. For future works regarding VLE studies with the microcapillary setup, the author suggests to only consider correction methods that use the CH-stretching vibration band. The DHM approach including the OH-stretching vibration band tends not to be suitable for systems including alcohols that have a higher chain length than ethanol. This results directly from the low signal-to-noise ratio.

The combined standard uncertainties for the VLE data obtained by the microcapillary setup can only be compared partially with the available literature data, since the majority of the authors didn't follow an uncertainty evaluation method. For instance Lin et al. [65] state a "reproducibility" for the saturated liquid phase of $u(x_i) = 0.01$ and for the saturated vapor phase of $u(y_i) = 0.01 - 0.03$ (for the n-hexadecane(*i*)/N₂ system). Rowane et al. [34] (only *px*-data) state for the same system a "maximum mole fraction expanded uncertainty" of $u(x_i) = 0.001$, while uncertainties of Sultanov et al. [69] could not be accessed. The values of Lin et al. and Rowane et al. tend to be however lower than the combined uncertainties obtained here, even though they are not directly comparable. From the publications of Weng et al. [65] and Lu et al. [66] regarding the binary system 1-octanol/N₂ an uncertainty cannot be directly extracted.

5.3 Mixture density measurements

5.3.1 Materials and Methods

CO₂ used in the experiments was purchased from Nippon Gas with a purity of 99.999 %_v, ethanol is listed in Table 11. The microcapillary used in the study is also identical to the one used in the VLE and vapor pressure experiments.

5.3.2 Results

By following the experimental procedure in section 4.2.3 the mixture densities of the saturated liquid and vapor phases were obtained for different pressure and temperature conditions. The therefrom latest obtained results are graphically shown in Figure 59. As it can be seen, the densities lie at some conditions close to the comparable literature values (for instance saturated vapor phase data at $T = 303.15\text{K}$), but do diverge significantly for the majority of the obtained data points. It can be therefrom extracted, that the proposed experimental procedure does not yet qualify for the determination of saturated mixture densities.

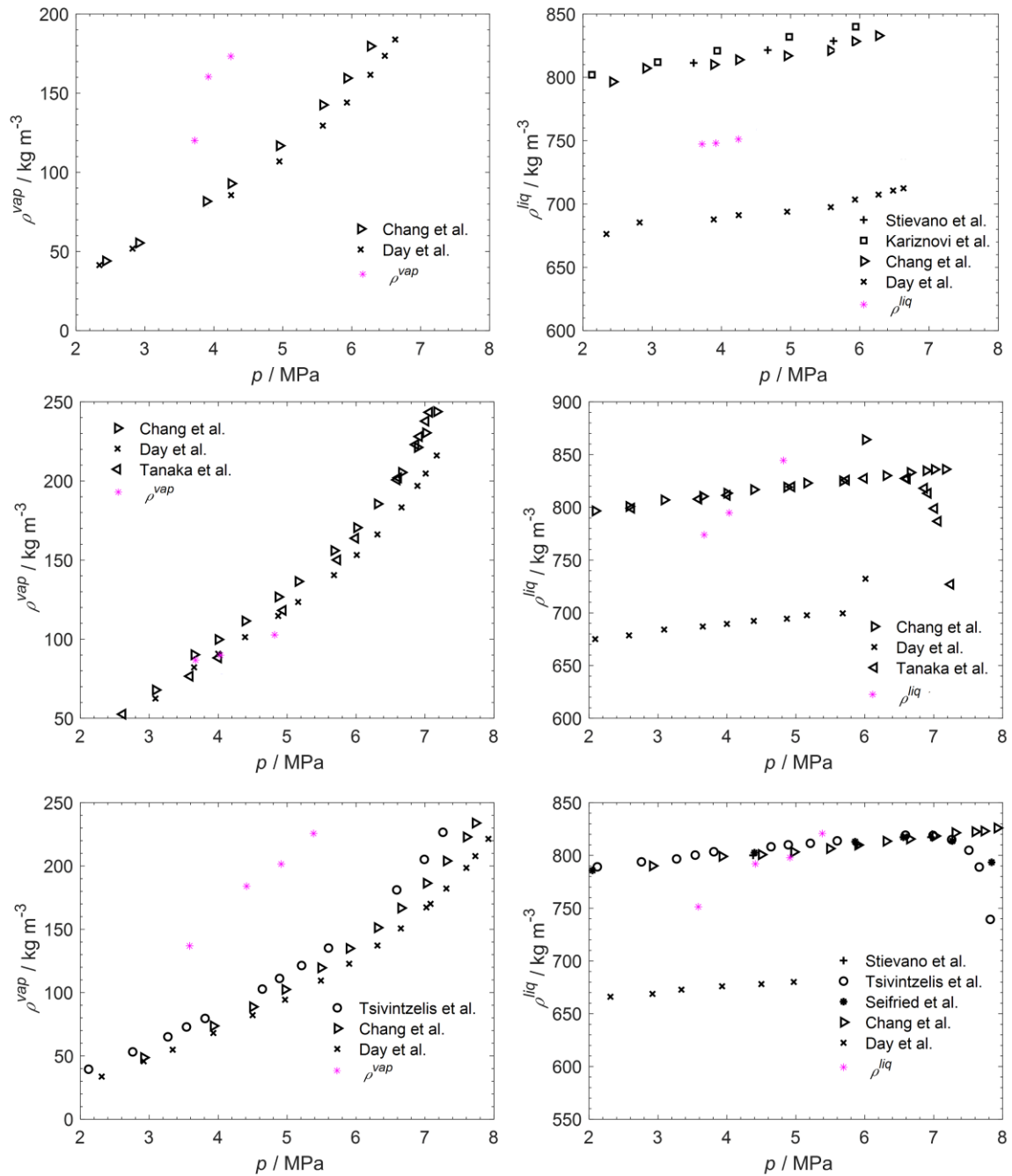


Figure 59: Experimentally obtained mixture densities for saturated vapor (left side) and liquid phases (right side) compared to literature data (compare Table 2) for 3 isotherms; top: 303.15 K, middle: 308.15 K and down: 313.15 K

5.3.3 Conclusion

It was further analyzed, where the strong deviations between the experimental data compared to the literature data might stem from. It can be seen by plotting the obtained bubble volumes and frequencies over the number of pictures of an experimental run (see Figure 60) that both frequency and volume show relatively high fluctuations. It is assumed that these fluctuations come from instationarities that are possibly a result of an uneven

bubble formation in the mixing section. The image treatment procedure itself might be furthermore problematic. Hereby the assumption of considering a bubble as a body consisting of a cylinder and two hemispheres might be not correct, due to the highly non-ideal behavior of the ethanol/CO₂ system regarding density, viscosity etc., especially at elevated pressure conditions, compared to flows of e. g. water/air at atmospheric conditions. It is therefore currently still being analyzed which measures to take in order to obtain more satisfactory experimental results.

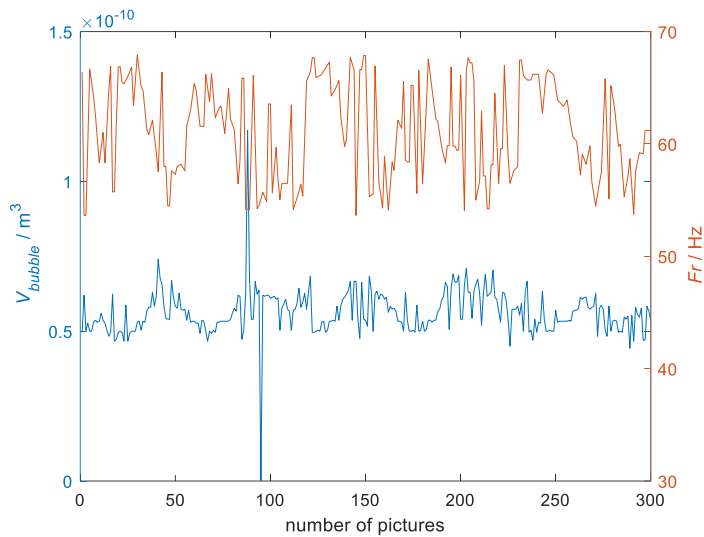


Figure 60: Obtained bubble volume and frequency over an experimental run

6 Summary

I presented experimental procedures for the determination of saturated vapor pressures, vapor/liquid equilibria and saturated liquid and vapor phase mixture densities by the use of a microfluidic setup. The data that were acquired are especially interesting since they cover elevated temperature and pressure conditions, for which the majority of experimental setups in use are not designed for.

The employed photo-optical methods as well as *in situ* Raman Spectroscopy are hereby suitable tools for the determination of the beforementioned properties. Regarding the latter, new evaluation techniques regarding the correction of the film-influence on the saturated vapor phase spectra, as well as general procedures regarding the isolation of the O₂-stretching band from the CH-bending vibration were developed. By the use of Raman spectroscopy, I moreover achieved to determine vapor/liquid equilibria of systems including oxygen. This is especially worth mentioning, when knowing of the potentially ignitable mixture compositions at which I operated, for what such studies were only carried out by a limited number of researchers in the field.

Throughout the thesis different equations of state and thermodynamic correlations have been employed. Especially the adjusted binary interaction coefficients for the EoS are of relevance, since VLE can be calculated for conditions that exceed those that were studied in this work.

7 Perspective

E-fuels will remain important for transport processes in aviation, seafaring, mining and other heavy-duty applications, where electric-battery drives are ruled out in near future. In the passenger car sector however, public interest in e-fuels might decrease due to the already available electric alternatives. The microfluidic setup should therefore also be used in order to determine the properties of compounds and mixtures that are especially relevant for other promising future applications. Those might be the investigation into thermodynamic data of novel cooling agents in heat pumps, or for example relevant phase equilibria for CO₂-storage or hydrogen applications. The microfluidic setup could be in the further also equipped by a Coriolis densometer, in order to measure unsaturated liquid and vapor phase densities, both of mixtures and pure compounds. It remains however of high interest, to obtain mixture densities at saturated conditions at high pressure and temperature and especially of asymmetric thermodynamic systems.

8 Tabulated experimental data

Table 27: measured vapor pressures of ethanol and 1-octanol (for validation) with maximum standard uncertainty of $u(T) = 2.51$ K and $u(p) = 0.12$ MPa

compound	T /K	p^s /MPa	compound	T /K	p^s /MPa
ethanol	423.12	0.961	ethanol	510.92	5.840
“	428.28	1.098	“	512.01	5.906
“	433.03	1.267	“	513.13	6.012
“	438.78	1.386	“	513.54	6.101
“	443.86	1.508	1-octanol	544.79	0.496
“	448.95	1.735	“	555.06	0.557
“	455.02	1.939	“	565.47	0.704
“	459.20	2.137	“	575.73	0.924
“	464.50	2.361	“	586.31	1.105
“	469.68	2.691	“	596.59	1.284
“	474.76	3.041	“	606.61	1.480
“	479.99	3.316	“	616.54	1.670
“	485.22	3.661	“	626.95	1.963
“	490.36	3.966	“	637.07	2.248
“	496.53	4.524	“	642.25	2.449
“	501.62	4.957	“	646.36	2.632
“	506.87	5.395	“	647.41	2.714
“	509.00	5.593	“	648.45	2.782

Table 28: measured vapor pressures of OME₃ and OME₄ with maximum standard uncertainty of $u(T) = 2.51$ K and $u(p) = 0.12$ MPa

compound	T /K	p^s /MPa	compound	T /K	p^s /MPa
OME ₃	490.26	0.439	OME ₃	587.72	2.320
“	495.22	0.490	“	592.39	2.509
“	500.43	0.518	“	597.68	2.652
“	505.66	0.606	“	603.01	2.886
“	513.11	0.668	OME ₄	543.09	0.520
“	517.53	0.778	“	548.12	0.565
“	522.67	0.876	“	551.72	0.625
“	527.50	0.953	“	558.58	0.684
“	532.78	1.041	“	563.22	0.740
“	538.48	1.117	“	567.11	0.816
“	543.13	1.197	“	573.82	0.925
“	546.78	1.278	“	578.91	0.999
“	553.39	1.386	“	583.86	1.049
“	556.80	1.443	“	588.82	1.174
“	563.86	1.627	“	593.92	1.275
“	567.11	1.654	“	599.15	1.374
“	572.18	1.777	“	604.14	1.501
“	577.37	1.993	“	609.40	1.656
“	582.47	2.095			

Table 29: revised vapor-liquid equilibrium data and combined standard uncertainties for binary system ethanol/oxygen; with $u_c(p) = \{0.029 - 0.047\}$ MPa and $u_c(T) = \{1.36 - 1.98\}$ K; for ternary VLE data of ethanol/nitrogen/oxygen see publication

p /MPa	T /K	x_{eth}	y_{eth}	$u_c(x_{eth})$	$u_c(y_{eth})$
3	303	0.9831	-	0.0011	-
5	303	0.9703	-	0.0011	-
6	303	0.9638	-	0.0011	-

6.5	303	0.9615	-	0.0011	-
8	303	0.9537	-	0.0012	-
3	313	0.9832	-	0.0012	-
5	313	0.9698	-	0.0012	-
6	313	0.9655	-	0.0010	-
6.5	313	0.9621	-	0.0012	-
8	313	0.9540	-	0.0012	-
3	323	0.9826	-	0.0012	-
5	323	0.9683	0.0148	0.0012	0.0078
6	323	0.9637	0.0113	0.0011	0.0080
6.5	323	0.9618	0.0058	0.0011	0.0176
8	323	0.9512	0.0079	0.0012	0.0148
3	333	0.9806	-	0.0011	-
5	333	0.9679	-	0.0011	-
6	333	0.9630	0.0126	0.0011	0.0088
6.5	333	0.9606	-	0.0011	-
8	333	0.9506	0.0078	0.0012	0.0146
3	343	0.9836	-	0.0011	-
5	343	0.9691	0.0252	0.0011	0.0111
6	343	0.9636	0.0326	0.0010	0.0075
6.5	343	0.9611	0.0305	0.0011	0.0097
8	343	0.9508	-	0.0012	-
3	353	0.9827	-	0.0011	-
5	353	0.9696	0.0347	0.0011	0.0137
6	353	0.9629	-	0.0011	-
6.5	353	0.9601	0.0452	0.0012	0.0071
8	353	0.9507	-	0.0012	-
3	363	0.9872	-	0.0011	-
5	363	0.9717	0.0682	0.0012	0.0125
6	363	0.9641	0.0652	0.0011	0.0090
6.5	363	0.9626	0.0544	0.0012	0.0128
8	363	0.9522	0.0014	0.0011	0.0150
3	373	0.9837	0.1097	0.0016	0.0276
5	373	0.9693	0.0811	0.0012	0.0124
6	373	0.9647	0.0671	0.0010	0.0087
6.5	373	0.9622	0.0667	0.0011	0.0110
8	373	0.9516	-	0.0012	-
3	383	0.9857	0.1596	0.0011	0.0116
5	383	0.9709	0.0839	0.0012	0.0175
6	383	0.9646	0.0701	0.0011	0.0099
6.5	383	0.9619	0.0881	0.0012	0.0111
8	383	0.9501	0.0643	0.0011	0.0098
3	393	0.9852	0.2118	0.0013	0.0156
5	393	0.9690	0.1343	0.0012	0.0160
6	393	0.9636	0.0958	0.0011	0.0098
6.5	393	0.9609	0.1308	0.0011	0.0144
8	393	0.9481	0.0981	0.0012	0.0217
3	403	0.9864	0.2346	0.0011	0.0182
5	403	0.9702	0.1701	0.0012	0.0188
6	403	0.9645	0.1654	0.0011	0.0120
6.5	403	0.9584	0.1447	0.0016	0.0142
8	403	0.9492	0.1212	0.0011	0.0140
3	413	0.9871	0.3466	0.0015	0.0234
5	413	0.9713	0.2515	0.0014	0.0369
6	413	0.9641	0.1991	0.0011	0.0134
6.5	413	0.9580	0.1968	0.0014	0.0139
8	413	0.9487	0.1420	0.0012	0.0131
3	423	0.9892	0.4448	0.0014	0.0296
5	423	0.9698	0.3173	0.0013	0.0202
6	423	0.9636	0.2843	0.0011	0.0151
6.5	423	0.9606	0.2461	0.0013	0.0117
8	423	0.9484	-	0.0012	-
3	433	0.9897	0.5741	0.0015	0.0297
5	433	0.9713	0.3758	0.0012	0.0202
6	433	0.9642	0.3515	0.0011	0.0168
6.5	433	0.9595	0.2916	0.0014	0.0293
8	433	0.9481	-	0.0012	-
3	443	0.9920	0.6999	0.0014	0.0452
5	443	0.9715	0.4758	0.0016	0.0256
6	443	0.9648	0.4310	0.0011	0.0271
6.5	443	0.9588	0.3620	0.0015	0.0313
8	443	0.9466	-	0.0016	-
3	453	0.9900	0.8471	0.0040	0.0320
5	453	0.9746	0.5602	0.0016	0.0456
6	453	0.9665	0.4992	0.0013	0.0297
6.5	453	0.9584	0.4556	0.0013	0.0237
8	453	0.9460	0.3324	0.0016	0.0286
5	463	0.9754	0.6530	0.0023	0.0331
6	463	0.9671	0.6029	0.0015	0.0264

6.5	463	0.9570	0.5442	0.0015	0.0229
8	463	0.9448	0.4654	0.0014	0.0488
6	473	0.9693	0.7021	0.0025	0.0337
6.5	473	0.9626	0.6286	0.0021	0.0232
8	473	0.9432	0.5581	0.0013	0.0464

Table 30: obtained vapor-liquid equilibrium data and combined standard uncertainties of binary system 1-octanol/nitrogen; the combined standard uncertainties of pressure and temperature range between $u_c(p) = \{0.002 - 0.020\}$ MPa and $u_c(T) = \{0.63 - 1.95\}$ K

T/K	x_{oct}	y_{oct}	$u_c(x_{oct})$	$u_c(y_{oct})$	T/K	x_{oct}	y_{oct}	$u_c(x_{oct})$	$u_c(y_{oct})$
3 MPa					6 MPa (continued)				
303.88	0.9840	-	0.0029	-	473.70	0.9393	0.0391	0.0030	0.0048
313.41	0.9830	-	0.0030	-	493.88	0.9337	0.0595	0.0029	0.0044
333.64	0.9827	-	0.0029	-	514.01	0.9286	0.0923	0.0029	0.0059
353.61	0.9815	-	0.0029	-	534.23	0.9224	0.1336	0.0034	0.0088
373.47	0.9802	-	0.0030	-	554.49	0.9179	0.1956	0.0030	0.0075
393.14	0.9771	0.0059	0.0030	0.0050	574.84	0.9109	0.2620	0.0030	0.0100
413.58	0.9759	0.0120	0.0030	0.0063	595.08	0.9046	0.3520	0.0032	0.0143
432.81	0.9736	0.0186	0.0030	0.0068	615.49	0.8944	0.4502	0.0037	0.0255
453.20	0.9712	0.0334	0.0030	0.0083	7 MPa				
473.30	0.9713	0.0581	0.0030	0.0063	303.39	0.9639	-	0.0029	-
493.43	0.9681	0.0974	0.0030	0.0080	313.35	0.9637	-	0.0030	-
513.30	0.9670	0.1465	0.0030	0.0084	333.46	0.9629	-	0.0028	-
533.41	0.9623	0.2185	0.0031	0.0131	353.39	0.9599	-	0.0029	-
553.44	0.9584	0.3144	0.0032	0.0147	373.16	0.9564	0.0012	0.0028	0.0031
573.59	0.9621	0.4181	0.0034	0.0164	393.30	0.9534	0.0034	0.0028	0.0035
593.67	0.9548	0.5477	0.0035	0.0211	413.24	0.9492	0.0058	0.0028	0.0037
613.89	0.9607	0.6682	0.0046	0.0273	432.80	0.9448	0.0112	0.0029	0.0038
4 MPa					452.94	0.9389	0.0193	0.0029	0.0040
303.30	0.9799	-	0.0029	-	473.31	0.9345	0.0345	0.0029	0.0037
313.40	0.9800	-	0.0029	-	493.76	0.9287	0.0550	0.0029	0.0041
333.39	0.9780	-	0.0029	-	513.17	0.9229	0.0843	0.0029	0.0047
353.36	0.9760	-	0.0029	-	533.33	0.9145	0.1234	0.0030	0.0054
373.15	0.9735	-	0.0029	-	553.37	0.9075	0.1766	0.0031	0.0079
393.25	0.9729	0.0044	0.0029	0.0043	573.80	0.8989	0.2361	0.0031	0.0086
413.74	0.9700	0.0072	0.0029	0.0043	594.12	0.8938	0.3179	0.0034	0.0127
433.01	0.9670	0.0145	0.0030	0.0039	614.41	0.8749	0.4073	0.0035	0.0160
453.79	0.9633	0.0269	0.0030	0.0040	8 MPa				
473.04	0.9615	0.0464	0.0030	0.0037	303.38	0.9613	-	0.0028	-
493.07	0.9561	0.0787	0.0031	0.0033	313.44	0.9598	-	0.0028	-
513.24	0.9546	0.1202	0.0031	0.0036	333.46	0.9577	-	0.0028	-
533.40	0.9542	0.1793	0.0032	0.0036	353.38	0.9546	-	0.0029	-
553.65	0.9510	0.2526	0.0036	0.0042	373.23	0.9514	0.0015	0.0028	0.0036
573.98	0.9442	0.3420	0.0032	0.0043	393.34	0.9456	0.0019	0.0029	0.0035
594.34	0.9426	0.4550	0.0036	0.0053	413.03	0.9423	0.0046	0.0029	0.0037
614.20	0.9396	0.5764	0.0045	0.0053	432.74	0.9371	0.0100	0.0029	0.0036
5 MPa					453.10	0.9309	0.0169	0.0029	0.0042
303.41	0.9747	-	0.0029	-	473.22	0.9242	0.0298	0.0029	0.0040
313.74	0.9741	-	0.0029	-	493.44	0.9172	0.0489	0.0029	0.0044
333.29	0.9715	-	0.0029	-	513.13	0.9093	0.0737	0.0029	0.0046
353.29	0.9715	-	0.0029	-	533.21	0.9021	0.1054	0.0029	0.0060
373.02	0.9677	0.0020	0.0029	0.0032	553.54	0.8930	0.1549	0.0030	0.0119
393.04	0.9658	0.0046	0.0029	0.0038	573.80	0.8833	0.2070	0.0032	0.0095
413.03	0.9634	0.0069	0.0029	0.0038	593.96	0.8706	0.2816	0.0033	0.0118
433.64	0.9582	0.0137	0.0030	0.0047	614.26	0.8505	0.3612	0.0038	0.0184
453.05	0.9560	0.0243	0.0029	0.0041	9 MPa				
473.39	0.9518	0.0405	0.0029	0.0041	303.42	0.9538	-	0.0029	-
493.47	0.9484	0.0650	0.0029	0.0046	313.21	0.9544	-	0.0029	-
513.65	0.9441	0.1037	0.0029	0.0065	333.47	0.9503	-	0.0028	-
533.69	0.9403	0.1546	0.0029	0.0064	353.25	0.9469	-	0.0029	-
553.94	0.9353	0.2141	0.0029	0.0076	373.07	0.9425	-	0.0029	-
574.17	0.9313	0.2921	0.0029	0.0102	393.03	0.9372	0.0016	0.0029	0.0030
594.41	0.9276	0.3918	0.0030	0.0126	413.05	0.9314	0.0049	0.0029	0.0037
614.73	0.9228	0.5012	0.0034	0.0155	433.13	0.9269	0.0094	0.0030	0.0033
6 MPa					453.09	0.9189	0.0165	0.0029	0.0020
303.19	0.9683	-	0.0029	-	473.71	0.9109	0.0284	0.0030	0.0036
313.61	0.9674	-	0.0029	-	493.91	0.9038	0.0451	0.0029	0.0040
333.36	0.9668	-	0.0029	-	513.97	0.8944	0.0689	0.0029	0.0040
353.27	0.9652	-	0.0029	-	534.12	0.8850	0.1016	0.0031	0.0049
373.11	0.9620	0.0022	0.0029	0.0039	554.08	0.8748	0.1440	0.0031	0.0056
393.18	0.9579	0.0041	0.0029	0.0044	574.67	0.8631	0.1994	0.0032	0.0082
413.43	0.9542	0.0063	0.0029	0.0036	594.76	0.8481	0.2691	0.0035	0.0115
433.63	0.9489	0.0135	0.0028	0.0068	614.98	0.8230	0.3464	0.0043	0.0153
453.57	0.9448	0.0214	0.0029	0.0072					

Table 31: obtained vapor-liquid equilibrium data and combined standard uncertainties of binary system 1-octanol/oxygen; the combined standard uncertainties of pressure and temperature range between $u_c(p) = \{0.002 - 0.031\}$ MPa and $u_c(T) = \{0.63 - 1.43\}$ K

T/K	x_{oct}	y_{oct}	$u_c(x_{oct})$	$u_c(y_{oct})$	T/K	x_{oct}	y_{oct}	$u_c(x_{oct})$	$u_c(y_{oct})$
3 MPa					6 MPa (continued)				
303.31	0.9756	-	0.0029	-	413.24	0.9362	0.0056	0.0029	0.0028
313.31	0.9740	-	0.0030	-	432.87	0.9332	0.0097	0.0029	0.0028
333.41	0.9741	-	0.0029	-	453.19	0.9317	0.0196	0.0029	0.0028
353.37	0.9727	-	0.0029	-	473.76	0.9271	0.0318	0.0030	0.0029
373.14	0.9715	-	0.0030	-	493.92	0.9234	0.0560	0.0029	0.0031
392.86	0.9723	-	0.0030	-	7 MPa				
412.54	0.9678	0.0072	0.0030	0.0028	303.25	0.9388	-	0.0029	-
432.15	0.9692	0.0136	0.0030	0.0029	313.31	0.9373	-	0.0029	-
453.66	0.9654	0.0304	0.0030	0.0031	333.37	0.9380	-	0.0029	-
473.77	0.9642	0.0523	0.0030	0.0033	353.34	0.9361	-	0.0029	-
4 MPa					373.14	0.9351	-	0.0029	-
303.27	0.9633	-	0.0029	-	393.46	0.9320	0.0020	0.0029	0.0029
313.45	0.9639	-	0.0030	-	413.28	0.9267	0.0052	0.0030	0.0029
333.44	0.9639	-	0.0031	-	433.01	0.9233	0.0088	0.0033	0.0029
353.40	0.9631	-	0.0032	-	453.11	0.9190	0.0177	0.0029	0.0028
373.27	0.9627	-	0.0034	-	473.80	0.9151	0.0314	0.0029	0.0029
392.89	0.9607	-	0.0034	-	493.78	0.9076	0.0508	0.0029	0.0030
413.08	0.9590	-	0.0045	-	8 MPa				
432.91	0.9562	0.0128	0.0029	0.0028	303.29	0.9304	-	0.0029	-
452.92	0.9535	0.0226	0.0029	0.0029	313.34	0.9302	-	0.0029	-
473.81	0.9518	0.0410	0.0029	0.0031	333.40	0.9297	-	0.0029	-
493.88	0.9496	0.0662	0.0029	0.0034	353.34	0.9289	-	0.0029	-
5 MPa					373.16	0.9273	-	0.0028	-
303.29	0.9542	-	0.0029	-	393.54	0.9227	-	0.0029	-
313.41	0.9555	-	0.0029	-	412.93	0.9194	0.0053	0.0029	0.0028
333.38	0.9557	-	0.0029	-	432.30	0.9127	-	0.0029	-
353.41	0.9538	-	0.0030	-	453.36	0.9085	0.0177	0.0029	0.0028
373.12	0.9538	-	0.0030	-	473.71	0.9037	0.0299	0.0034	0.0030
392.86	0.9514	0.0035	0.0030	0.0028	493.86	0.8984	0.0500	0.0030	0.0031
413.27	0.9497	0.0062	0.0031	0.0028	9 MPa				
433.08	0.9441	0.0115	0.0031	0.0028	303.29	0.9240	-	0.0029	-
452.93	0.9436	0.0207	0.0032	0.0029	313.35	0.9240	-	0.0030	-
473.76	0.9413	0.0356	0.0036	0.0030	333.42	0.9227	-	0.0033	-
493.87	0.9367	0.0592	0.0032	0.0034	353.31	0.9181	-	0.0029	-
6 MPa					373.36	0.9163	-	0.0029	-
303.20	0.9464	-	0.0036	-	393.28	0.9121	-	0.0029	-
313.32	0.9472	-	0.0045	-	413.11	0.9060	-	0.0029	-
333.37	0.9472	-	0.0029	-	432.84	0.9017	-	0.0029	-
353.36	0.9453	-	0.0029	-	453.51	0.8962	0.0165	0.0029	0.0028
373.12	0.9439	-	0.0029	-	473.81	0.8896	0.0292	0.0029	0.0028
393.53	0.9400	0.0031	0.0029	0.0028	493.85	0.8828	0.0458	0.0029	0.0029

Table 32: VLE data for the binary system n-tridecane(i)/N₂ with combined standard uncertainties u_c ; combined standard uncertainties for pressure and temperature lie within $u_c(p) = \{0.0008 - 0.0082\}$ MPa and $u_c(T) = \{0.62 - 2.28\}$ K

p /MPa	T /K	x_i	y_i	$u_c(x_i)$	$u_c(y_i)$
1.5	303.23	0.9835	-	0.0036	-
1.5	333.47	0.9775	-	0.0037	-
1.5	363.66	0.9789	-	0.0039	-
1.5	394.13	0.9747	-	0.0042	-
1.5	423.51	0.9710	-	0.0042	-
1.5	453.34	0.9757	-	0.0043	-
1.5	484.69	0.9652	0.0379	0.0042	0.0129
1.5	514.44	0.9694	0.0702	0.0042	0.0115
1.5	544.63	0.9730	0.1441	0.0055	0.0067
1.5	575.11	0.9655	0.2296	0.0073	0.0072
1.5	605.63	0.9682	0.3812	0.0071	0.0078
3	303.28	0.9652	-	0.0041	-
3	333.59	0.9619	-	0.0037	-
3	363.66	0.9594	-	0.0038	-
3	393.63	0.9574	-	0.0038	-
3	423.59	0.9512	-	0.0038	-
3	453.41	0.9486	-	0.0038	-
3	483.65	0.9439	0.0185	0.0040	0.0349
3	513.96	0.9291	0.0428	0.0042	0.0097
3	544.45	0.9341	0.0819	0.0045	0.0068
3	574.87	0.9343	0.1356	0.0049	0.0066
3	605.36	0.9307	0.2240	0.0049	0.0053
3	635.91	0.9120	0.3348	0.0059	0.0056
5	303.16	0.9448	-	0.0037	-
5	333.48	0.9396	-	0.0036	-
5	363.54	0.9361	-	0.0037	-
5	394.15	0.9310	-	0.0036	-
5	423.45	0.9253	-	0.0036	-
5	453.42	0.9183	-	0.0037	-
5	484.46	0.9090	0.0146	0.0037	0.0334
5	514.97	0.9032	0.0322	0.0039	0.0058
5	544.38	0.8913	0.0575	0.0044	0.0057
5	574.97	0.8841	0.0981	0.0044	0.0076
5	605.38	0.8703	0.1599	0.0046	0.0056
5	635.41	0.8346	0.2446	0.0072	0.0063
6.5	303.16	0.9294	-	0.0037	-
6.5	333.64	0.9252	-	0.0036	-
6.5	363.63	0.9180	-	0.0038	-
6.5	394.46	0.9139	-	0.0037	-
6.5	423.83	0.9065	-	0.0038	-
6.5	453.75	0.8953	-	0.0037	-
6.5	484.09	0.8874	0.0123	0.0038	0.0163
6.5	514.73	0.8770	0.0264	0.0040	0.0069
6.5	544.58	0.8628	0.0481	0.0042	0.0061
6.5	575.09	0.8504	0.0795	0.0046	0.0057
6.5	605.80	0.8309	0.1374	0.0049	0.0063
6.5	635.57	0.7912	0.2063	0.0070	0.0055
8	303.54	0.9164	-	0.0037	-
8	333.71	0.9087	-	0.0037	-
8	363.90	0.9033	-	0.0036	-
8	393.71	0.8948	-	0.0036	-
8	424.33	0.8851	-	0.0036	-
8	454.31	0.8738	-	0.0036	-
8	484.79	0.8615	0.0124	0.0039	0.0207
8	514.35	0.8532	0.0263	0.0039	0.0054
8	544.73	0.8314	0.0461	0.0044	0.0054
8	574.65	0.8213	0.0755	0.0048	0.0053
8	605.71	0.7920	0.1236	0.0051	0.0046
8	634.89	0.7365	0.1975	0.0074	0.0053
9	303.21	0.9054	-	0.0036	-
9	333.60	0.8982	-	0.0036	-
9	363.86	0.8912	-	0.0036	-
9	393.57	0.8841	-	0.0036	-
9	423.26	0.8734	-	0.0036	-
9	453.47	0.8636	0.0067	0.0037	0.0132
9	484.34	0.8503	0.0131	0.0037	0.0208
9	514.83	0.8346	0.0265	0.0040	0.0265
9	545.41	0.8143	0.0475	0.0043	0.0475
9	576.12	0.7967	0.0750	0.0048	0.0750
9	605.16	0.7696	0.1257	0.0053	0.1257
9	635.24	0.6999	0.1950	0.0078	0.1950

Table 33: VLE data for the binary system n-pentadecane(i)/N₂ with combined standard uncertainties u_c ; combined standard uncertainties for pressure and temperature lie within $u_c(p) = \{0.0011 - 0.0097\}$ MPa and $u_c(T) = \{0.63 - 2.26\}$ K

p /MPa	T /K	x_i	y_i	$u_c(x_i)$	$u_c(y_i)$
1.5	303.26	0.9809	-	0.0040	-
1.5	333.50	0.9814	-	0.0039	-
1.5	363.75	0.9789	-	0.0037	-
1.5	393.11	0.9770	-	0.0039	-
1.5	423.36	0.9765	-	0.0039	-
1.5	453.11	0.9743	0.0089	0.0037	0.0096
1.5	484.32	0.9702	0.0235	0.0042	0.0106
1.5	514.30	0.9676	0.0451	0.0043	0.0121
1.5	544.32	0.9643	0.0950	0.0058	0.0247
1.5	574.50	0.9576	0.1863	0.0054	0.0268
1.5	605.05	0.9598	0.3077	0.0062	0.0367
1.5	635.30	0.9675	0.4790	0.0065	0.0668
3	303.26	0.9651	-	0.0036	-
3	333.57	0.9648	-	0.0036	-
3	363.45	0.9632	-	0.0036	-
3	394.06	0.9586	-	0.0036	-
3	423.32	0.9566	-	0.0036	-
3	453.34	0.9513	0.0077	0.0037	0.0055
3	484.09	0.9483	0.0170	0.0037	0.0062
3	514.18	0.9417	0.0327	0.0039	0.0084
3	544.47	0.9387	0.0652	0.0041	0.0111
3	574.81	0.9300	0.1134	0.0043	0.0138
3	605.32	0.9290	0.1866	0.0041	0.0148
3	635.45	0.9233	0.2973	0.0042	0.0281
5	303.85	0.9443	-	0.0037	-
5	333.64	0.9414	-	0.0037	-
5	364.14	0.9383	-	0.0036	-
5	394.19	0.9327	-	0.0037	-
5	423.78	0.9282	-	0.0036	-
5	454.38	0.9238	0.0069	0.0037	0.0051
5	484.64	0.9139	0.0148	0.0037	0.0064
5	514.84	0.9034	0.0267	0.0043	0.0077
5	545.14	0.8976	0.0513	0.0046	0.0140
5	575.53	0.8929	0.0853	0.0044	0.0122
5	605.40	0.8831	0.1353	0.0047	0.0132
5	635.61	0.8635	0.2211	0.0045	0.0159
6.5	303.33	0.9312	-	0.0037	-
6.5	333.93	0.9277	-	0.0037	-
6.5	364.11	0.9212	-	0.0037	-
6.5	394.11	0.9177	-	0.0036	-
6.5	423.45	0.9091	-	0.0036	-
6.5	453.58	0.9024	0.0058	0.0036	0.0051
6.5	484.47	0.8918	0.0130	0.0037	0.0058
6.5	514.64	0.8838	0.0220	0.0040	0.0076
6.5	544.94	0.8718	0.0392	0.0042	0.0106
6.5	575.31	0.8532	0.0738	0.0044	0.0084
6.5	605.86	0.8440	0.1193	0.0044	0.0108
6.5	635.74	0.8298	0.1895	0.0048	0.0124
8	303.29	0.9161	-	0.0038	-
8	333.65	0.9103	-	0.0036	-
8	363.76	0.9010	-	0.0040	-
8	393.73	0.8967	-	0.0036	-
8	423.42	0.8853	-	0.0038	-
8	454.23	0.8774	-	0.0037	-
8	484.36	0.8668	0.0073	0.0037	0.0048
8	514.61	0.8560	0.0166	0.0038	0.0070
8	545.03	0.8435	0.0286	0.0039	0.0075
8	575.23	0.8273	0.0535	0.0042	0.0058
8	605.69	0.8087	0.0895	0.0044	0.0068
8	635.76	0.7815	0.1402	0.0048	0.0084
9	303.33	0.9094	-	0.0037	-
9	333.61	0.9006	-	0.0036	-
9	363.64	0.8928	-	0.0036	-
9	393.60	0.8841	-	0.0036	-
9	423.47	0.8749	-	0.0038	-
9	453.64	0.8635	-	0.0036	-
9	484.29	0.8513	0.0077	0.0037	0.0051
9	514.48	0.8352	0.0146	0.0037	0.0051
9	544.92	0.8239	0.0270	0.0040	0.0084
9	575.22	0.8036	0.0473	0.0044	0.0069
9	605.58	0.7846	0.0762	0.0044	0.0073
9	635.19	0.7510	0.1140	0.0051	0.0116

Table 34: VLE data including the additional validation datapoints for the binary system n-hexadecane(i)/N₂ with combined standard uncertainties u_c ; combined standard uncertainties for pressure and temperature lie within $u_c(p) = \{0.0090 - 0.0222\}$ MPa and $u_c(T) = \{0.62 - 2.13\}$ K

p / MPa	T / K	x_i	y_i	$u_c(x_i)$	$u_c(y_i)$
1.5	303.17	0.9797	-	0.0047	-
1.5	333.33	0.9721	-	0.0048	-
1.5	363.33	0.9735	-	0.0050	-
1.5	392.78	0.9763	-	0.0057	-
1.5	422.17	0.9756	-	0.0056	-
1.5	451.98	0.9729	-	0.0052	-
1.5	482.77	0.9662	-	0.0064	-
1.5	509.47	0.9610	-	0.0069	-
1.5	543.55	0.9670	-	0.0073	-
1.5	573.92	0.9552	-	0.0076	-
1.5	604.33	0.9603	0.2642	0.0083	0.0525
3	303.18	0.9661	-	0.0037	-
3	333.35	0.9630	-	0.0040	-
3	363.18	0.9619	-	0.0037	-
3	392.81	0.9587	-	0.0037	-
3	422.24	0.9558	-	0.0037	-
3	451.91	0.9497	-	0.0039	-
3	483.47	0.9426	0.0132	0.0042	0.0145
3	513.26	0.9377	0.0294	0.0060	0.0271
3	543.77	0.9329	0.0607	0.0063	0.0320
3	574.17	0.9250	0.0916	0.0054	0.0308
3	604.19	0.9210	0.1423	0.0055	0.0185
5	303.32	0.9434	-	0.0044	-
5	333.33	0.9376	-	0.0039	-
5	363.38	0.9367	-	0.0038	-
5	392.96	0.9287	-	0.0040	-
5	422.20	0.9248	-	0.0039	-
5	452.02	0.9213	-	0.0040	-
5	483.28	0.9162	0.0111	0.0046	0.0141
5	513.68	0.9050	0.0267	0.0055	0.0199
5	544.04	0.8993	0.0379	0.0054	0.0279
5	574.51	0.8822	0.0608	0.0053	0.0195
5	605.06	0.8734	0.1049	0.0063	0.0191
5	635.44	0.8601	0.1552	0.0073	0.0229
6.5	303.19	0.9295	-	0.0042	-
6.5	333.45	0.9239	-	0.0045	-
6.5	363.48	0.9185	-	0.0046	-
6.5	392.81	0.9145	-	0.0041	-
6.5	422.26	0.9005	-	0.0040	-
6.5	452.06	0.8931	-	0.0046	-
6.5	483.15	0.8880	0.0087	0.0053	0.0164
6.5	513.55	0.8767	0.0185	0.0060	0.0245
6.5	543.79	0.8672	0.0337	0.0055	0.0221
6.5	574.33	0.8587	0.0543	0.0053	0.0142
6.5	605.29	0.8421	0.0870	0.0051	0.0134
6.5	635.00	0.8248	0.1386	0.0054	0.0133
8	303.12	0.9167	-	0.0040	-
8	333.47	0.9119	-	0.0040	-
8	363.47	0.9011	-	0.0038	-
8	393.19	0.8930	-	0.0039	-
8	422.70	0.8810	-	0.0038	-
8	452.58	0.8736	-	0.0042	-
8	483.36	0.8630	0.0094	0.0049	0.0150
8	513.87	0.8528	0.0173	0.0046	0.0164
8	544.01	0.8402	0.0301	0.0046	0.0154
8	574.47	0.8299	0.0474	0.0048	0.0104
8	604.95	0.8047	0.0778	0.0053	0.0118
8	635.39	0.7820	0.1303	0.0053	0.0120
9	303.16	0.9092	-	0.0043	-
9	333.38	0.8982	-	0.0042	-
9	363.43	0.8942	-	0.0040	-
9	392.78	0.8860	-	0.0039	-
9	422.20	0.8737	-	0.0037	-
9	451.90	0.8618	-	0.0039	-
9	482.82	0.8538	0.0070	0.0041	0.0103
9	513.41	0.8362	0.0151	0.0050	0.0135
9	543.67	0.8205	0.0243	0.0046	0.0158
9	574.13	0.8103	0.0426	0.0049	0.0090
9	604.58	0.7882	0.0716	0.0054	0.0106
9	634.91	0.7573	0.1152	0.0053	0.0088
2	463.07	0.9585	0.0072	0.0053	0.0129
3	462.96	0.9468	0.0054	0.0047	0.0085
3	625.63	0.8751	0.1263	0.0121	0.0471
5	463.00	0.9156	0.0038	0.0040	0.0066
5	524.63	0.8957	0.0250	0.0068	0.0188
5	625.18	0.8437	0.1112	0.0062	0.0230
10	462.85	0.8417	0.0022	0.0040	0.0055

10	524.59	0.8071	0.0128	0.0046	0.0079
10	626.01	0.7173	0.0677	0.0062	0.0255

Table 35: VLE data for the binary system n-heptadecane(i)/N₂ with combined standard uncertainties u_c ; combined standard uncertainties for pressure and temperature lie within $u_c(p) = \{0.0008 - 0.0077\}$ MPa and $u_c(T) = \{0.62 - 2.05\}$ K

p / MPa	T / K	x_i	y_i	$u_c(x_i)$	$u_c(y_i)$
1.5	303.25	0.9801	-	0.0042	-
1.5	333.59	0.9787	-	0.0040	-
1.5	363.47	0.9754	-	0.0043	-
1.5	394.03	0.9728	-	0.0045	-
1.5	423.36	0.9677	-	0.0046	-
1.5	454.08	0.9636	-	0.0048	-
1.5	484.32	0.9590	-	0.0057	-
1.5	514.56	0.9507	-	0.0074	-
1.5	544.04	0.9476	-	0.0082	-
1.5	574.43	0.9435	-	0.0078	-
1.5	605.08	0.9377	0.1895	0.0087	0.0550
1.5	635.44	0.9334	0.3125	0.0140	0.0802
3	303.55	0.9606	-	0.0036	-
3	333.28	0.9592	-	0.0039	-
3	363.33	0.9567	-	0.0038	-
3	393.90	0.9558	-	0.0037	-
3	423.23	0.9518	-	0.0043	-
3	453.01	0.9477	-	0.0040	-
3	484.24	0.9405	-	0.0052	-
3	514.55	0.9323	-	0.0048	-
3	544.88	0.9242	0.0445	0.0062	0.0181
3	574.37	0.9132	0.0750	0.0078	0.0249
3	605.83	0.9025	0.1314	0.0092	0.0468
3	635.30	0.8784	0.1974	0.0133	0.0430
5	303.27	0.9435	-	0.0039	-
5	333.45	0.9386	-	0.0038	-
5	363.54	0.9333	-	0.0037	-
5	394.08	0.9274	-	0.0039	-
5	423.38	0.9236	-	0.0037	-
5	453.02	0.9182	-	0.0041	-
5	483.36	0.9115	-	0.0043	-
5	513.52	0.9000	-	0.0052	-
5	544.07	0.8904	0.0340	0.0059	0.0143
5	574.47	0.8820	0.0501	0.0055	0.0143
5	605.10	0.8707	0.0830	0.0070	0.0163
5	635.19	0.8655	0.1337	0.0066	0.0237
6.5	303.18	0.9267	-	0.0041	-
6.5	333.25	0.9204	-	0.0039	-
6.5	363.13	0.9179	-	0.0037	-
6.5	393.49	0.9104	-	0.0039	-
6.5	422.86	0.9042	-	0.0037	-
6.5	452.45	0.8925	-	0.0039	-
6.5	483.27	0.8785	-	0.0053	-
6.5	513.62	0.8700	0.0135	0.0053	0.0123
6.5	544.01	0.8605	0.0268	0.0060	0.0119
6.5	574.30	0.8565	0.0449	0.0073	0.0180
6.5	604.83	0.8398	0.0959	0.0092	0.0253
6.5	634.94	0.8230	0.1185	0.0110	0.0399
8	303.28	0.9157	-	0.0036	-
8	333.18	0.9083	-	0.0037	-
8	363.30	0.8988	-	0.0037	-
8	393.94	0.8949	-	0.0038	-
8	423.31	0.8841	-	0.0039	-
8	453.06	0.8732	-	0.0039	-
8	484.31	0.8663	-	0.0040	-
8	514.73	0.8473	0.0095	0.0047	0.0098
8	544.10	0.8368	0.0194	0.0050	0.0090
8	574.61	0.8167	0.0332	0.0047	0.0078
8	604.99	0.8066	0.0606	0.0058	0.0122
8	635.33	0.7803	0.0975	0.0064	0.0129
9	303.29	0.9061	-	0.0039	-
9	333.52	0.8988	-	0.0037	-
9	363.42	0.8908	-	0.0037	-
9	394.00	0.8791	-	0.0037	-
9	423.45	0.8683	-	0.0038	-
9	453.08	0.8601	-	0.0038	-
9	484.41	0.8493	-	0.0038	-
9	514.48	0.8287	0.0118	0.0045	0.0076
9	543.98	0.8180	0.0204	0.0052	0.0080
9	574.48	0.8041	0.0353	0.0057	0.0105
9	604.58	0.8087	0.0595	0.0058	0.0126
9	634.72	0.7873	0.1016	0.0069	0.0180

9 References

- [1] Pati A, Gierth S, Haspel P, Hasse C, Munier J. Strategies to Define Surrogate Fuels for the Description of the Multicomponent Evaporation Behavior of Hydrocarbon Fuels. In: SAE Technical Paper Series. SAE International 400 Commonwealth Drive, Warrendale, PA, United States; 2018.
- [2] Gierth S, Hunger F, Popp S, Wu H, Ihme M, Hasse C. Assessment of differential diffusion effects in flamelet modeling of oxy-fuel flames. *Combustion and Flame* 2018;197:134–44. <https://doi.org/10.1016/j.combustflame.2018.07.023>.
- [3] Bazyleva A, Abildskov J, Anderko A, Baudouin O, Chernyak Y, Hemptinne J-C de et al. Good Reporting Practice for Thermophysical and Thermochemical Property Measurements (IUPAC Technical Report). *Pure Appl Chem* 2021;93(2). <https://doi.org/10.1515/pac-2020-0403>.
- [4] Tassios DP. Applied chemical engineering thermodynamics. Berlin: Springer; 1993.
- [5] Franses EI. Thermodynamics with chemical engineering applications. Cambridge, GB: Cambridge University Press; 2014.
- [6] Rong B-G (ed.). Process synthesis and process intensification: Methodological approaches. Berlin, Boston: De Gruyter; 2017.
- [7] Dahm KD, Visco DP. Fundamentals of chemical engineering thermodynamics. Australia: Cengage Learning; 2015.
- [8] Gmehling J, Kleiber M, Kolbe B, Rarey J (eds.). Chemical thermodynamics for process simulation. Weinheim: Wiley-VCH; 2019.
- [9] Seiffert S, Thiele J. Microfluidics: Theory and practice for beginners. Berlin, Boston: De Gruyter; 2020.
- [10] Tabeling P. Introduction to microfluidics. Oxford, New York, NY: Oxford University Press; 2005.
- [11] Kuleshov A, Mahkamov K. Multi-zone diesel fuel spray combustion model for the simulation of a diesel engine running on biofuel. *Proceedings of the Institution of Mechanical Engineers, Part A: Journal of Power and Energy* 2008;222(3):309–21. <https://doi.org/10.1243/09576509JPE530>.

- [12] Yuan W, Hansen AC, Zhang Q. Predicting the Physical Properties of Biodiesel for Combustion Modeling. *Transactions of the ASAE* 2003;46(6):1487–93. <https://doi.org/10.13031/2013.15631>.
- [13] Sajots W. Vapor Pressures of Saturated Vapors at High Temperatures. *Beibl. Ann. Phys.* 1879;3:741.
- [14] Hannay JB, Hogarth J. On the solubility of solids in gases. *Proc. R. Soc. London* 1880 // 1879;30 // 29(196-199):178. <https://doi.org/10.1098/rspl.1879.0054>.
- [15] Ambrose D, Sprake C, Townsend R. Thermodynamic properties of organic oxygen compounds XXXVII. Vapour pressures of methanol, ethanol, pentan-1-ol, and octan-1-ol from the normal boiling temperature to the critical temperature. *The Journal of Chemical Thermodynamics* 1975;7(2):185–90. [https://doi.org/10.1016/0021-9614\(75\)90267-0](https://doi.org/10.1016/0021-9614(75)90267-0).
- [16] Ambrose D, Broderick BE, Townsend R. The critical temperatures and pressures of thirty organic compounds. *J. Appl. Chem.* 1974;24(6):359–72. <https://doi.org/10.1002/jctb.2720240607>.
- [17] Radosz M, Lydersen A. Heat of Vaporization of Aliphatic Alcohols. *Chemie Ingenieur Technik* 1980;52(9):756–7. <https://doi.org/10.1002/cite.330520918>.
- [18] Lydersen AL, Tsochev V. Critical temperatures and pressures and high temperature vapour pressures of seven alcohols. *Chem. Eng. Technol.* 1990;13(1):125–30. <https://doi.org/10.1002/ceat.270130117>.
- [19] Pélerin D, Gaukel K, Härtl M, Jacob E, Wachtmeister G. Potentials to simplify the engine system using the alternative diesel fuels oxymethylene ether OME1 and OME3–6 on a heavy-duty engine. *Fuel* 2020;259:116231. <https://doi.org/10.1016/j.fuel.2019.116231>.
- [20] Popp T, Lechner R, Becker M, Hebauer M, O'Connell N, Brautsch M. Potentials of OME/diesel blends for stationary power production – Improving emission characteristics of a diesel CHP unit. *Applied Thermal Engineering* 2019;153:483–92. <https://doi.org/10.1016/j.applthermaleng.2019.03.015>.
- [21] Richter G, Zellbeck H. Oxymethylene Ethers as an Alternative for Passenger Car Diesel Engines. *MTZ Motortech Z* 2017;78(12):66–73. <https://doi.org/10.1007/s35146-017-0131-y>.
- [22] ZHAO Q, WANG H, QIN Z, WU Z, WU J, FAN W et al. Synthesis of polyoxymethylene dimethyl ethers from methanol and trioxymethylene with molecular

- sieves as catalysts. *Journal of Fuel Chemistry and Technology* 2011;39(12):918–23. [https://doi.org/10.1016/S1872-5813\(12\)60003-6](https://doi.org/10.1016/S1872-5813(12)60003-6).
- [23] Baranowski CJ, Bahmanpour AM, Kröcher O. Catalytic synthesis of polyoxymethylene dimethyl ethers (OME): A review. *Applied Catalysis B: Environmental* 2017;217:407–20. <https://doi.org/10.1016/j.apcatb.2017.06.007>.
- [24] Breitzkreuz CF, Schmitz N, Ströfer E, Burger J, Hasse H. Design of a Production Process for Poly(oxymethylene) Dimethyl Ethers from Dimethyl Ether and Trioxane. *Chemie Ingenieur Technik* 2018;90(10):1489–96. <https://doi.org/10.1002/cite.201800038>.
- [25] Bongartz D, Burre J, Mitsos A. Power-to-OME - Processes for the Production of Oxymethylene Dimethyl Ether from Hydrogen and Carbon Dioxide. *Chemie Ingenieur Technik* 2018;90(9):1155. <https://doi.org/10.1002/cite.201855050>.
- [26] Burger J, Ströfer E, Hasse H. Production process for diesel fuel components poly(oxymethylene) dimethyl ethers from methane-based products by hierarchical optimization with varying model depth. *Chemical Engineering Research and Design* 2013;91(12):2648–62. <https://doi.org/10.1016/j.cherd.2013.05.023>.
- [27] Burger J, Siegert M, Ströfer E, Hasse H. Poly(oxymethylene) dimethyl ethers as components of tailored diesel fuel: Properties, synthesis and purification concepts. *Fuel* 2010;89(11):3315–9. <https://doi.org/10.1016/j.fuel.2010.05.014>.
- [28] KANG M, SONG H, JIN F, CHEN J. Synthesis and physicochemical characterization of polyoxymethylene dimethyl ethers. *Journal of Fuel Chemistry and Technology* 2017;45(7):837–45. [https://doi.org/10.1016/S1872-5813\(17\)30040-3](https://doi.org/10.1016/S1872-5813(17)30040-3).
- [29] Lautenschütz L, Oestreich D, Seidenspinner P, Arnold U, Dinjus E, Sauer J. Physico-chemical properties and fuel characteristics of oxymethylene dialkyl ethers. *Fuel* 2016;173:129–37. <https://doi.org/10.1016/j.fuel.2016.01.060>.
- [30] Honecker C, Neumann M, Glueck S, Schoenen M, Pischinger S. Optical Spray Investigations on OME3-5 in a Constant Volume High Pressure Chamber. In: SAE Technical Paper Series. SAE International400 Commonwealth Drive, Warrendale, PA, United States; 2019.
- [31] Dageförde T, Gröger K, Kawaharada N, Dinkelacker F. Velocity Field Measurements with High Speed Structural Image Velocimetry in the Primary Atomization Region of Future Diesel Fuels. In: SAE Technical Paper Series. SAE International400 Commonwealth Drive, Warrendale, PA, United States; 2020.

- [32] Boyd RH. Some physical properties of polyoxymethylene dimethyl ethers. *J. Polym. Sci.* 1961;50(153):133–41. <https://doi.org/10.1002/pol.1961.1205015316>.
- [33] Kulkarni A, García EJ, Damone A, Schappals M, Stephan S, Kohns M et al. A Force Field for Poly(oxymethylene) Dimethyl Ethers (OMEn). *J Chem Theory Comput* 2020;16(4):2517–28. <https://doi.org/10.1021/acs.jctc.9b01106>.
- [34] Rowane AJ, Gavaises M, McHugh MA. Vapor-liquid equilibria and mixture densities for 2,2,4,4,6,8,8-heptamethylnonane + N₂ and n-hexadecane + N₂ binary mixtures up to 535 K and 135 MPa. *Fluid Phase Equilibria* 2020;506:112378. <https://doi.org/10.1016/j.fluid.2019.112378>.
- [35] Rodriguez C, Rokni HB, Koukouvinis P, Gupta A, Gavaises M. Complex multicomponent real-fluid thermodynamic model for high-pressure Diesel fuel injection. *Fuel* 2019;257(5):115888. <https://doi.org/10.1016/j.fuel.2019.115888>.
- [36] SAE Technical Paper Series. SAE International 400 Commonwealth Drive, Warrendale, PA, United States; 2014.
- [37] Deep A, Kumar N, Karnwal A, Gupta D, Vibhanshu V, Sharma A et al. Assessment of the Performance and Emission Characteristics of 1-Octanol/Diesel Fuel Blends in a Water Cooled Compression Ignition Engine. In: SAE Technical Paper Series. SAE International 400 Commonwealth Drive, Warrendale, PA, United States; 2014.
- [38] García A, Monsalve-Serrano J, Villalta D, Zubel M, Pischinger S. Potential of 1-octanol and di-n-butyl ether (DNBE) to improve the performance and reduce the emissions of a direct injected compression ignition diesel engine. *Energy Conversion and Management* 2018;177:563–71. <https://doi.org/10.1016/j.enconman.2018.10.009>.
- [39] Phoon LY, Mustaffa AA, Hashim H, Mat R, Manan ZA, Yunus NA. Performance and emission characteristics of green diesel blends containing diethyl-succinate and 1-octanol. *Journal of Cleaner Production* 2017;161:1192–202. <https://doi.org/10.1016/j.jclepro.2017.06.219>.
- [40] Ashok B, Nanthagopal K, Anand V, Aravind KM, Jeevanantham AK, Balusamy S. Effects of n-octanol as a fuel blend with biodiesel on diesel engine characteristics. *Fuel* 2019;235:363–73. <https://doi.org/10.1016/j.fuel.2018.07.126>.
- [41] Nour M, Attia AM, Nada SA. Combustion, performance and emission analysis of diesel engine fuelled by higher alcohols (butanol, octanol and heptanol)/diesel blends. *Energy Conversion and Management* 2019;185:313–29. <https://doi.org/10.1016/j.enconman.2019.01.105>.

- [42] Li J, Yu W, Yang W. Evaluating performance and emissions of a CI engine fueled with n-octanol/diesel and n-butanol/diesel blends under different injection strategies. *Fuel* 2021;284:119085. <https://doi.org/10.1016/j.fuel.2020.119085>.
- [43] Li J, Zhou D, Yang W. A multi-component reaction mechanism of n-butanol, n-octanol, and di-n-buthylether for engine combustion. *Fuel* 2020;275:117975. <https://doi.org/10.1016/j.fuel.2020.117975>.
- [44] Atabani AE, AL Kulthoom S. Spectral, thermoanalytical characterizations, properties, engine and emission performance of complementary biodiesel-diesel-pentanol/octanol blends. *Fuel* 2020;282:118849. <https://doi.org/10.1016/j.fuel.2020.118849>.
- [45] Gainey B, Lawler B. The role of alcohol biofuels in advanced combustion: An analysis. *Fuel* 2021;283:118915. <https://doi.org/10.1016/j.fuel.2020.118915>.
- [46] Palmer J, Ramesh M, Kirsch V, Reddemann M, Kneer R. Spray Analysis of C₈H₁₈O Fuel Blends Using High-Speed Schlieren Imaging and Mie Scattering. In: SAE Technical Paper Series. SAE International400 Commonwealth Drive, Warrendale, PA, United States; 2015.
- [47] Zhu H, Bohac SV, Nakashima K, Hagen LM, Huang Z, Assanis DN. Effect of biodiesel and ethanol on load limits of high-efficiency premixed low-temperature combustion in a diesel engine. *Fuel* 2013;106:773–8. <https://doi.org/10.1016/j.fuel.2012.10.073>.
- [48] Masuda Y, Chen Z. Combustion and Emission Characteristics of a PCI Engine Fueled with Ethanol-Diesel Blends. In: SAE Technical Paper Series. SAE International400 Commonwealth Drive, Warrendale, PA, United States; 2009.
- [49] El-Seesy AI, Hassan H, Ibraheem L, He Z, Soudagar MEM. Combustion, emission, and phase stability features of a diesel engine fueled by Jatropha/ethanol blends and n-butanol as co-solvent. *International Journal of Green Energy* 2020;17(12):793–804. <https://doi.org/10.1080/15435075.2020.1798770>.
- [50] He B-Q, Shuai S-J, Wang J-X, He H. The effect of ethanol blended diesel fuels on emissions from a diesel engine. *Atmospheric Environment* 2003;37(35):4965–71. <https://doi.org/10.1016/j.atmosenv.2003.08.029>.
- [51] Di Y, Cheung CS, Huang Z. Experimental study on particulate emission of a diesel engine fueled with blended ethanol–dodecanol–diesel. *Journal of Aerosol Science* 2009;40(2):101–12. <https://doi.org/10.1016/j.jaerosci.2008.09.004>.
- [52] Raffius T, Ottenwalder T, Schulz C, Grunefeld G, Ko H-J, Pischinger S. Laser spectroscopic investigation of diesel-like jet structure using C₈ oxygenates as the fuel. *Fuel* 2019;235:1515–29. <https://doi.org/10.1016/j.fuel.2018.07.124>.

- [53] Preuß J, Munch K, Denbratt I. Performance and emissions of long-chain alcohols as drop-in fuels for heavy duty compression ignition engines. *Fuel* 2018;216:890–7. <https://doi.org/10.1016/j.fuel.2017.11.122>.
- [54] Coelho ST, Goldemberg J, Lucon O, Guardabassi P. Brazilian sugarcane ethanol: lessons learned. *Energy for Sustainable Development* 2006;10(2):26–39. [https://doi.org/10.1016/S0973-0826\(08\)60529-3](https://doi.org/10.1016/S0973-0826(08)60529-3).
- [55] Crago CL, Khanna M, Barton J, Giuliani E, Amaral W. Competitiveness of Brazilian sugarcane ethanol compared to US corn ethanol. *Energy Policy* 2010;38(11):7404–15. <https://doi.org/10.1016/j.enpol.2010.08.016>.
- [56] Schemme S, Breuer JL, Köller M, Meschede S, Walman F, Samsun RC et al. H₂-based synthetic fuels: A techno-economic comparison of alcohol, ether and hydrocarbon production. *International Journal of Hydrogen Energy* 2020;45(8):5395–414. <https://doi.org/10.1016/j.ijhydene.2019.05.028>.
- [57] Schemme S, Breuer JL, Samsun RC, Peters R, Stolten D. Promising catalytic synthesis pathways towards higher alcohols as suitable transport fuels based on H₂ and CO₂. *Journal of CO₂ Utilization* 2018;27:223–37. <https://doi.org/10.1016/j.jcou.2018.07.013>.
- [58] Maitlis PM, Klerk A de. *Greener Fischer-Tropsch Processes for Fuels and Feedstocks*. Wiley; 2013.
- [59] Fischer K, Wilken M. Experimental determination of oxygen and nitrogen solubility in organic solvents up to 10 MPa at temperatures between 298 K and 398 K. *J. Chem. Thermodyn.* 2001;33(10):1285–308. <https://doi.org/10.1006/jcht.2001.0837>.
- [60] Klima TC, Braeuer AS. Vapor-liquid-equilibria of fuel-nitrogen systems at engine-like conditions measured with Raman spectroscopy in micro capillaries. *Fuel* 2019;238:312–9. <https://doi.org/10.1016/j.fuel.2018.10.108>.
- [61] Schnabel T, Vrabec J, Hasse H. Henry's law constants of methane, nitrogen, oxygen and carbon dioxide in ethanol from 273 to 498 K: Prediction from molecular simulation. *Fluid Phase Equilib.* 2005;233(2):134–43. <https://doi.org/10.1016/j.fluid.2005.04.016>.
- [62] Malviya A, Vrabec J. Henry's Law Constant of Nitrogen, Oxygen, and Argon in Ternary Aqueous Alcoholic Solvent Mixtures. *J. Chem. Eng. Data* 2019. <https://doi.org/10.1021/acs.jced.9b00571>.
- [63] Boyer FL, Bircher LJ. The Solubility of Nitrogen, Argon, Methane, Ethylene and Ethane in Normal Primary Alcohols. *Journal of Physiscal Chemistry* 1960;64:1330–1.

- [64] Bo S, Battino R, Wilhelm E. Solubility of gases in liquids. 19. Solubility of He, Ne, Ar, Kr, Xe, N₂, O₂, CH₄, CF₄, and SF₆ in normal 1-alkanols n-C₁H₂+1OH (1 .ltoreq. 1 .ltoreq. 11) at 298.15 K. *J. Chem. Eng. Data* 1993;38(4):611–6. <https://doi.org/10.1021/je00012a035>.
- [65] Weng W-L, Lee M-J. Vapor-liquid equilibria for nitrogen with 2-methyl-1-pentanol, 1-octanol, or 1-decanol binary systems. *Fluid Phase Equilibria* 1996;122(1-2):243–53. [https://doi.org/10.1016/0378-3812\(96\)03012-9](https://doi.org/10.1016/0378-3812(96)03012-9).
- [66] Lu X, Wu Z, Hou Y. Solubilities of N₂, H₂, Ar in 1-octanol at high pressure. *Fluid Phase Equilibria* 1994;92:139–48. [https://doi.org/10.1016/0378-3812\(94\)80045-6](https://doi.org/10.1016/0378-3812(94)80045-6).
- [67] Fechter MH, Koschack J, Braeuer AS. Vapor-Liquid equilibria of the systems 1-octanol/nitrogen and 1-octanol/oxygen at pressures from 3 to 9 MPa and temperatures up to 613 K – Measured in a microcapillary with Raman spectroscopy. *Fuel* 2022;323(8):124352. <https://doi.org/10.1016/j.fuel.2022.124352>.
- [68] Lin H-M, Kim H, Chao K-C. Gas-liquid equilibria in nitrogen + n-hexadecane mixtures at elevated temperatures and pressures. *Fluid Phase Equilibria* 1981;7(2):181–5. [https://doi.org/10.1016/0378-3812\(81\)85020-0](https://doi.org/10.1016/0378-3812(81)85020-0).
- [69] Sultanov R, Skripka G, Namiot G. Yu. *Gazov. Delo* 1972;10(43).
- [70] Llave FM, Chung TH. Vapor-liquid equilibria of nitrogen-hydrocarbon systems at elevated pressures. *J. Chem. Eng. Data* 1988;33(2):123–8. <https://doi.org/10.1021/je00052a019>.
- [71] Gao W, Robinson RL, Gasem KAM. High-Pressure Solubilities of Hydrogen, Nitrogen, and Carbon Monoxide in Dodecane from 344 to 410 K at Pressures to 13.2 MPa. *J. Chem. Eng. Data* 1999;44(1):130–2. <https://doi.org/10.1021/je9801664>.
- [72] García-Córdova T, Justo-García DN, García-Flores BE, García-Sánchez F. Vapor–Liquid Equilibrium Data for the Nitrogen + Dodecane System at Temperatures from (344 to 593) K and at Pressures up to 60 MPa. *J. Chem. Eng. Data* 2011;56(4):1555–64. <https://doi.org/10.1021/je1012372>.
- [73] D'Avila SG, Kaul BK, Prausnitz JM. Solubilities of heavy hydrocarbons in compressed methane and nitrogen. *J. Chem. Eng. Data* 1976;21(4):488–91. <https://doi.org/10.1021/je60071a017>.
- [74] Leeuw VV de, Loos T de, Kooijman HA, Swaan Arons J de. The experimental determination and modelling of VLE for binary subsystems of the quaternary system N₂ + CH₄ + C₄H₁₀ + C₁₄H₃₀ UP to 1000 bar and 440 K. *Fluid Phase Equilibria* 1992;73(3):285–321. [https://doi.org/10.1016/0378-3812\(92\)80015-2](https://doi.org/10.1016/0378-3812(92)80015-2).

- [75] Deiters UK, Schneider GM. High pressure phase equilibria: experimental methods. *Fluid Phase Equilibria* 1986;29:145–60. [https://doi.org/10.1016/0378-3812\(86\)85018-X](https://doi.org/10.1016/0378-3812(86)85018-X).
- [76] Schwedt G. *Analytische Chemie: Grundlagen Methoden und Praxis*. Stuttgart: Thieme; 1995.
- [77] Peper S, Dohrn R. Sampling from fluid mixtures under high pressure: Review, case study and evaluation. *J. Supercrit. Fluids* 2012;66:2–15. <https://doi.org/10.1016/j.supflu.2011.09.021>.
- [78] Swaid I, Nickel D, Schneider GM. NIR—spectroscopic investigations on phase behaviour of low—volatile organic substances in supercritical carbon dioxide. *Fluid Phase Equilibria* 1985;21(1-2):95–112. [https://doi.org/10.1016/0378-3812\(85\)90062-7](https://doi.org/10.1016/0378-3812(85)90062-7).
- [79] Nickel D, Schneider GM. Near-infrared spectroscopic investigations on phase behaviour and association of 1-hexanol and 1-decanol in carbon dioxide, chlorotrifluoromethane, and sulfur hexafluoride. *The Journal of Chemical Thermodynamics* 1989;21(3):293–305. [https://doi.org/10.1016/0021-9614\(89\)90019-0](https://doi.org/10.1016/0021-9614(89)90019-0).
- [80] Diller DE, Chang RF. Composition of Mixtures of Natural Gas Components Determined by Raman Spectrometry. *Applied Spectroscopy* 1980;34(4):411–4.
- [81] Kaiser T, Voßmerbäumer C, Schweiger G. A new approach to the determination of fluid phase Equilibria: Concentration measurements by Raman spectroscopy. *Berichte der Bunsengesellschaft für physikalische Chemie* 1992;96(8):976–80. <https://doi.org/10.1002/BBPC.19920960805>.
- [82] Liebergesell B, Brands T, Koß H-J, Bardow A. Quaternary isothermal vapor-liquid equilibrium of the model biofuel 2-butanone + n-heptane + tetrahydrofuran + cyclohexane using Raman spectroscopic characterization. *Fluid Phase Equilibria* 2018;472:107–16. <https://doi.org/10.1016/j.fluid.2018.04.009>.
- [83] Liebergesell B, Flake C, Brands T, Koß H-J, Bardow A. A milliliter-scale setup for the efficient characterization of isothermal vapor-liquid equilibria using Raman spectroscopy. *Fluid Phase Equilibria* 2017;446:36–45. <https://doi.org/10.1016/j.fluid.2017.04.014>.
- [84] Liu N, Aymonier C, Lecoutre C, Garrabos Y, Marre S. Microfluidic approach for studying CO₂ solubility in water and brine using confocal Raman spectroscopy.

- Chemical Physics Letters 2012;551:139–43.
<https://doi.org/10.1016/j.cplett.2012.09.007>.
- [85] Wang J, He B, Xie L, Bei K, Li G, Chen Z et al. Determination of CO₂ Solubility in Water and NaCl Solutions under Geological Sequestration Conditions Using a Fused Silica Capillary Cell with in Situ Raman Spectroscopy. *J. Chem. Eng. Data* 2019;64(6):2484–96. <https://doi.org/10.1021/acs.jced.9b00013>.
- [86] Wang Z, Zhou Q, Guo H, Yang P, Lu W. Determination of water solubility in supercritical CO₂ from 313.15 to 473.15 K and from 10 to 50 MPa by in-situ quantitative Raman spectroscopy. *Fluid Phase Equilibria* 2018;476:170–8. <https://doi.org/10.1016/j.fluid.2018.08.006>.
- [87] Wang Z, Zhou Q, Guo H, Yang P, Lu W. Determination of water solubility in supercritical CO₂ from 313.15 to 473.15 K and from 10 to 50 MPa by in-situ quantitative Raman spectroscopy. *Fluid Phase Equilibria* 2018;476:170–8. <https://doi.org/10.1016/j.fluid.2018.08.006>.
- [88] Thien J, Peters C, Brands T, Koß H-J, Bardow A. Efficient Determination of Liquid–Liquid Equilibria Using Microfluidics and Raman Microspectroscopy. *Ind. Eng. Chem. Res.* 2017;56(46):13905–10. <https://doi.org/10.1021/acs.iecr.7b03230>.
- [89] Thien J, Reinhold L, Brands T, Koß H-J, Bardow A. Automated Physical Property Measurements from Calibration to Data Analysis: Microfluidic Platform for Liquid–Liquid Equilibrium Using Raman Microspectroscopy. *J. Chem. Eng. Data* 2020;65(2):319–27. <https://doi.org/10.1021/acs.jced.9b00636>.
- [90] Kasterke M, Thien J, Flake C, Brands T, Bahr L, Bardow André et al. Automated Measurement of Liquid-liquid Equilibria using Raman Spectroscopy and Single Droplet Tracking in Microfluidic Plug Flow. *Fluid Phase Equilibria* 2023;567(2). <https://doi.org/10.1016/j.fluid.2022.113718>.
- [91] Luther SK, Will S, Braeuer A. Phase-specific Raman spectroscopy for fast segmented microfluidic flows. *Lab Chip* 2014;14(16):2910–3. <https://doi.org/10.1039/C4LC00428K>.
- [92] Luther SK, Stehle S, Weihs K, Will S, Braeuer A. Determination of vapor-liquid equilibrium data in microfluidic segmented flows at elevated pressures using Raman spectroscopy. *Anal Chem* 2015;87(8):165–172. <https://doi.org/10.1021/acs.analchem.5b00699>.
- [93] Fechter MHH, Braeuer AS. Vapor-Liquid Equilibria of Mixtures Containing Ethanol, Oxygen, and Nitrogen at Elevated Pressure and Temperature, Measured with In Situ

- Raman Spectroscopy in Microcapillaries. *J. Chem. Eng. Data* 2020;65(7):3373–83. <https://doi.org/10.1021/acs.jced.0c00184>.
- [94] Hübner M, Minceva M. Microfluidics approach for determination of the equilibrium phase composition in multicomponent biphasic liquid systems. *Chemical Engineering Research and Design* 2022;184:592–602. <https://doi.org/10.1016/j.cherd.2022.06.023>.
- [95] Hübner M, Minceva M. Microfluidics approach for determination of the miscibility gap of multicomponent liquid-liquid systems. *Experimental Thermal and Fluid Science* 2020;112:109971. <https://doi.org/10.1016/j.expthermflusci.2019.109971>.
- [96] Chang Chiehming J, Chiu Kou-Lung, Day Chang-Yih. A new apparatus for the determination of P–x–y diagrams and Henry’s constants in high pressure alcohols with critical carbon dioxide. *Journal of Supercritical Fluids* 1998(12):223–37.
- [97] Chiehming J. Chang, Chany-Yih Day, Ching-Ming Ko, Kou-Lung Chiu. Densities and P-x-y diagrams for carbon dioxide dissolution in methanol, ethanol, and acetone mixtures. *Fluid Phase Equilibria* 1997(131):243–58.
- [98] Kariznovi M, Nourozieh H, Abedi J. Experimental measurements and predictions of density, viscosity, and carbon dioxide solubility in methanol, ethanol, and 1-propanol. *The Journal of Chemical Thermodynamics* 2013;57:408–15. <https://doi.org/10.1016/j.jct.2012.10.002>.
- [99] Matteo Stievano, Nicola Elvassore. High-pressure density and vapor–liquid equilibrium for the binary systems carbon dioxide–ethanol, carbon dioxide–acetone and carbon dioxide–dichloromethane. *Journal of Supercritical Fluids* 2005(33):7–14.
- [100] Bernhard Seifried, Feral Temelli. Density of Carbon Dioxide Expanded Ethanol at (313.2, 328.2, and 343.2) K. *J. Chem. Eng. Data* 2010(55):2410–5.
- [101] I. Tsivintzelis, D. Missopolinou, K. Kalogiannis, C. Panayiotou. Phase compositions and saturated densities for the binary systems of carbon dioxide with ethanol and dichloromethane. *Fluid Phase Equilibria* 2004(224):89–96.
- [102] Chany-Yih Day, Chiehming J. Chang, Chiu-Yang Chen. Phase Equilibrium of Ethanol + CO₂ and Acetone + CO₂ at Elevated Pressures. *J. Chem. Eng. Data* 1996(41):839–43.
- [103] H. TANAKA, M. KATO. Vapor-Liquid Equilibrium Properties of Carbon Dioxid + Ethanol Mixtures at high Pressure. *JOURNAL OF CHEMICAL ENGINEERING OF JAPAN* 1995(Vol. 28 No. 3):263–6.

- [104] Thulasidas TC, Abraham MA, Cerro RL. Bubble-train flow in capillaries of circular and square cross section. *Chemical Engineering Science* 1995;50(2):183–99. [https://doi.org/10.1016/0009-2509\(94\)00225-G](https://doi.org/10.1016/0009-2509(94)00225-G).
- [105] Triplett KA, Ghiaasiaan SM, Abdel-Khalik SI, LeMouel A, McCord BN. Gas–liquid two-phase flow in microchannels. *International Journal of Multiphase Flow* 1999;25(3):395–410. [https://doi.org/10.1016/S0301-9322\(98\)00055-X](https://doi.org/10.1016/S0301-9322(98)00055-X).
- [106] Pan Z, Zhang X, Xie Y, Cai W. Instantaneous Mass Transfer under Gas-Liquid Taylor Flow in Circular Capillaries. *Chem. Eng. Technol.* 2014;37(3):495–504. <https://doi.org/10.1002/ceat.201300354>.
- [107] Dang M, Yue J, Chen G, Yuan Q. Formation characteristics of Taylor bubbles in a microchannel with a converging shape mixing junction. *Chemical Engineering Journal* 2013;223:99–109. <https://doi.org/10.1016/j.cej.2013.02.108>.
- [108] Yin Y, Fu T, Zhu C, Guo R, Ma Y, Li H. Dynamics and mass transfer characteristics of CO₂ absorption into MEA/[Bmim][BF₄] aqueous solutions in a microchannel. *Separation and Purification Technology* 2019;210:541–52. <https://doi.org/10.1016/j.seppur.2018.08.045>.
- [109] Yue J, Chen G, Yuan Q, Luo L, Gonthier Y. Hydrodynamics and mass transfer characteristics in gas–liquid flow through a rectangular microchannel. *Chemical Engineering Science* 2007;62(7):2096–108. <https://doi.org/10.1016/j.ces.2006.12.057>.
- [110] Palmer DA. *Handbook of Applied Thermodynamics*. CRC Press; 2019.
- [111] Yeo YK. *Chemical Engineering Computation with MATLAB®*. Boca Raton: Taylor & Francis, CRC Press; 2017.
- [112] van der Waals, J. D. on the continuity of the gaseous and liquid states. Leiden; 1873.
- [113] Coutinho JA, Kontogeorgis GM, Stenby EH. Binary interaction parameters for nonpolar systems with cubic equations of state: a theoretical approach 1. CO₂/hydrocarbons using SRK equation of state. *Fluid Phase Equilibria* 1994;102(1):31–60. [https://doi.org/10.1016/0378-3812\(94\)87090-X](https://doi.org/10.1016/0378-3812(94)87090-X).
- [114] Lopez-Echeverry JS, Reif-Acherman S, Araujo-Lopez E. Peng-Robinson equation of state: 40 years through cubics. *Fluid Phase Equilibria* 2017;447:39–71. <https://doi.org/10.1016/j.fluid.2017.05.007>.
- [115] Peng D-Y, Robinson DB. A New Two-Constant Equation of State. *Ind. Eng. Chem. Fund.* 1976;15(1):59–64. <https://doi.org/10.1021/i160057a011>.
- [116] Fechter MHH, Haspel P, Hasse C, Braeuer AS. Vapor pressures and latent heats of vaporization of Poly(oxyethylene) Dimethyl Ethers (OME3 and OME4) up to the

- vicinity of the critical temperature. *Fuel* 2021;303:121274. <https://doi.org/10.1016/j.fuel.2021.121274>.
- [117] Privat R, Jaubert J-N, Mutelet F. Use of the PPR78 Model To Predict New Equilibrium Data of Binary Systems Involving Hydrocarbons and Nitrogen. Comparison with Other GCEOS. *Ind. Eng. Chem. Res.* 2008;47(19):7483–9. <https://doi.org/10.1021/ie800636h>.
- [118] Jaubert J-N, Mutelet F. VLE predictions with the Peng–Robinson equation of state and temperature dependent k_{ij} calculated through a group contribution method. *Fluid Phase Equilibria* 2004;224(2):285–304. <https://doi.org/10.1016/j.fluid.2004.06.059>.
- [119] Robinson DB, Peng DY. The characterization of the heptanes and heavier fractions for the GPA Peng-Robinson programs. Research Report RR-28. Gas Processors Association; Tulsa, Oklahoma 1978.
- [120] Fechter M, Braeuer AS. Vapor-Liquid Equilibria of binary systems consisting of nitrogen and n-tridecane, n-pentadecane, n-hexadecane and n-heptadecane at pressures of 1.5 - 9 MPa and temperatures of 303 – 633 K – determined with a Raman Spectroscopy coupled microfluidic device. *J. Chem. Eng. Data* accepted manuscript: 2023.
- [121] Gross J, Sadowski G. Perturbed-Chain SAFT: An Equation of State Based on a Perturbation Theory for Chain Molecules. *Ind. Eng. Chem. Res.* 2001;40(4):1244–60. <https://doi.org/10.1021/ie0003887>.
- [122] Gross J, Sadowski G. Application of the Perturbed-Chain SAFT Equation of State to Associating Systems. *Ind. Eng. Chem. Res.* 2002;41(22):5510–5. <https://doi.org/10.1021/ie010954d>.
- [123] Huang SH, Radosz M. Equation of state for small, large, polydisperse, and associating molecules. *Ind. Eng. Chem. Res.* 1990;29(11):2284–94. <https://doi.org/10.1021/ie00107a014>.
- [124] Span R, Wagner W. A New Equation of State for Carbon Dioxide Covering the Fluid Region from the Triple-Point Temperature to 1100 K at Pressures up to 800 MPa. *Journal of Physical and Chemical Reference Data* 1996;25(6):1509–96. <https://doi.org/10.1063/1.555991>.
- [125] National Institute of Standard and Technology. Thermophysical Properties of Fluid Systems. [February 24, 2023]; Available from: <https://webbook.nist.gov/chemistry/fluid/>.

- [126] Pénélox A, Rauzy E, Fréze R. A consistent correction for Redlich-Kwong-Soave volumes. *Fluid Phase Equilibria* 1982;8(1):7–23. [https://doi.org/10.1016/0378-3812\(82\)80002-2](https://doi.org/10.1016/0378-3812(82)80002-2).
- [127] Rackett HG. Equation of state for saturated liquids. *J. Chem. Eng. Data* 1970;15(4):514–7. <https://doi.org/10.1021/je60047a012>.
- [128] Spencer CF, Danner RP. Improved equation for prediction of saturated liquid density. *J. Chem. Eng. Data* 1972;17(2):236–41. <https://doi.org/10.1021/je60053a012>.
- [129] Spencer CF, Adler SB. A critical review of equations for predicting saturated liquid density. *J. Chem. Eng. Data* 1978;23(1):82–9. <https://doi.org/10.1021/je60076a008>.
- [130] Daubert TE, Danner RP. *Physical and thermodynamic properties of pure chemicals: Data compilation*. New York: Hemisphere Pub. Corp; 1989.
- [131] Dillon HE, Penoncello SG. A Fundamental Equation for Calculation of the Thermodynamic Properties of Ethanol. *Int J Thermophys* 2004;25(2):321–35. <https://doi.org/10.1023/B:IJOT.0000028470.49774.14>.
- [132] Brown OLI. The Clausius-Clapeyron equation. *J. Chem. Educ.* 1951;28(8):428. <https://doi.org/10.1021/ed028p428>.
- [133] Velasco S, Román FL, White JA. On the Clausius–Clapeyron Vapor Pressure Equation. *J. Chem. Educ.* 2009;86(1):106. <https://doi.org/10.1021/ed086p106>.
- [134] van Konynenburg PH, Scott RL. Critical lines and phase equilibria in binary van der Waals mixtures. *Phil. Trans. R. Soc. Lond. A* 1980;298(1442):495–540. <https://doi.org/10.1098/rsta.1980.0266>.
- [135] *Supercritical Fluids: Fundamentals for Application*. Cham: Springer International Publishing; 20.
- [136] Deiters UK, Kraska T. *High-pressure fluid phase equilibria: Phenomenology and computation*. Amsterdam, Boston (Mass.), Paris [etc.]: Elsevier; 2012.
- [137] Ziegler JW, Dorsey JG, Chester TL, Innis DP. Estimation of Liquid-Vapor Critical Loci for CO₂-Solvent Mixtures Using a Peak-Shape Model. *Anal Chem* 1995;67(2):456–61. <https://doi.org/10.1021/ac00098a034>.
- [138] Whitesides GM. The origins and the future of microfluidics. *Nature* 2006;442(7101):368–73. <https://doi.org/10.1038/nature05058>.
- [139] Lo RC. Application of Microfluidics in Chemical Engineering. *Chem Eng Process Tech* 1 2013;1002.

- [140] Martin A, Camy S, Aubin J. Hydrodynamics of CO₂-ethanol flow in a microchannel under elevated pressure. *Chemical Engineering Science* 2018;178:297–311. <https://doi.org/10.1016/j.ces.2017.12.046>.
- [141] Braeuer A (ed.). *In situ spectroscopic techniques at high pressure*. Amsterdam, Netherlands: Elsevier; 2015.
- [142] Rajan G (ed.). *Optical Fiber Sensors: Advanced Techniques and Applications*. 1st ed. CRC Press; 2017.
- [143] Luther SK, Schuster JJ, Leipertz A, Braeuer A. Microfluidic investigation into mass transfer in compressible multi-phase systems composed of oil, water and carbon dioxide at elevated pressure. *The Journal of Supercritical Fluids* 2013;84:121–31. <https://doi.org/10.1016/j.supflu.2013.10.002>.
- [144] Bureau International des Poids et Mesures. Evaluation of measurement data – Guide to the expression of uncertainty in measurement. [March 08, 2021]; Available from: <https://www.bipm.org/en/publications/guides/gum.html>.
- [145] Rosenthal DJ, Teja AS. Critical pressures and temperatures of isomeric alkanols. *Ind. Eng. Chem. Res.* 1989;28(11):1693–6. <https://doi.org/10.1021/ie00095a020>.
- [146] Shakhverdiev AN, Naziev YM, Safarov DT. Thermal properties of some aliphatic alcohols near liquid-vapor phase transitions. *Zh. Prikl. Khim.* 1992;65:1631–7.
- [147] Quadri SK, Khilar KC, Kudchadker AP, Patni MJ. Measurement of the critical temperatures and critical pressures of some thermally stable or mildly unstable alkanols. *The Journal of Chemical Thermodynamics* 1991;23(1):67–76. [https://doi.org/10.1016/S0021-9614\(05\)80060-6](https://doi.org/10.1016/S0021-9614(05)80060-6).
- [148] Moine E, Piña-Martinez A, Jaubert J-N, Sirjean B, Privat R. I -PC-SAFT: An Industrialized Version of the Volume-Translated PC-SAFT Equation of State for Pure Components, Resulting from Experience Acquired All through the Years on the Parameterization of SAFT-Type and Cubic Models. *Ind. Eng. Chem. Res.* 2019;58(45):20815–27. <https://doi.org/10.1021/acs.iecr.9b04660>.
- [149] Nannoolal Y, Rarey J, Ramjugernath D. Estimation of pure component properties. *Fluid Phase Equilibria* 2007;252(1-2):1–27. <https://doi.org/10.1016/j.fluid.2006.11.014>.
- [150] Joback KG, Reid RC. Estimation of Pure-Component Properties from Group-Contributions. *Chemical Engineering Communications* 1987;57(1-6):233–43. <https://doi.org/10.1080/00986448708960487>.

- [151] Wilson GM, Jasperson LV. Critical Constants T_c P_c . Estimation Based on Zero, First, Second-Order Methods. New Orleans, Los Angeles; 1996.
- [152] Marrero-Morejón J, Pardillo-Fontdevila E. Estimation of pure compound properties using group-interaction contributions. *AIChE J.* 1999;45(3):615–21. <https://doi.org/10.1002/aic.690450318>.
- [153] Marrero J, Gani R. Group-contribution based estimation of pure component properties. *Fluid Phase Equilibria* 2001;183-184:183–208. [https://doi.org/10.1016/S0378-3812\(01\)00431-9](https://doi.org/10.1016/S0378-3812(01)00431-9).
- [154] Li J, Xia L, Xiang S. A new method based on elements and chemical bonds for organic compounds critical properties estimation. *Fluid Phase Equilibria* 2016;417:1–6. <https://doi.org/10.1016/j.fluid.2016.01.008>.
- [155] Li H, Jia M. Measurements and Derivation of the Spray Simulation Required Physical Properties of Polyoxymethylene Dimethyl Ethers (PODEn). *Int J Thermophys* 2023;44(3). <https://doi.org/10.1007/s10765-022-03147-1>.
- [156] Beutler T, Prchal N, Günthner M. Numerical modeling of diesel and polyoxymethylene dimethyl ether spray in a high pressure chamber using the fischer primary breakup model. *Automot. Engine Technol.* 2022;7(3-4):409–26. <https://doi.org/10.1007/s41104-022-00120-w>.
- [157] Stryjek R, Vera JH. PRSV: An improved peng-Robinson equation of state for pure compounds and mixtures. *Can. J. Chem. Eng.* 1986;64(2):323–33. <https://doi.org/10.1002/cjce.5450640224>.
- [158] Stryjek R, Vera JH. PRSV2: A cubic equation of state for accurate vapor-liquid equilibria calculations. *Can. J. Chem. Eng.* 1986;64(5):820–6. <https://doi.org/10.1002/cjce.5450640516>.
- [159] Gude M, Teja AS. Vapor-Liquid Critical Properties of Elements and Compounds. 4. Aliphatic Alkanols. *J. Chem. Eng. Data* 1995;40(5):1025–36. <https://doi.org/10.1021/je00021a001>.
- [160] NIST ThermoData Engine (TDE) 10.2. National Institute of Standards and Technology (NIST).
- [161] Diamantonis NI, Economou IG. Evaluation of Statistical Associating Fluid Theory (SAFT) and Perturbed Chain-SAFT Equations of State for the Calculation of Thermodynamic Derivative Properties of Fluids Related to Carbon Capture and Sequestration. *Energy Fuels* 2011;25(7):3334–43. <https://doi.org/10.1021/ef200387p>.

- [162] Cibulka I, Zikova M. Liquid Densities at Elevated Pressures of 1-Alkanols from C1 to C10: A Critical Evaluation of Experimental Data. *J. Chem. Eng. Data* 1994;39(4):876–86. <https://doi.org/10.1021/je00016a055>.
- [163] Cibulka I. Saturated liquid densities of 1-alkanols from C1 to c10 and n-alkanes from C5 to C16: A critical evaluation of experimental data. *Fluid Phase Equilibria* 1993;89(1):1–18. [https://doi.org/10.1016/0378-3812\(93\)85042-K](https://doi.org/10.1016/0378-3812(93)85042-K).
- [164] Cibulka I, Hnědkovský L. Liquid Densities at Elevated Pressures of n -Alkanes from C 5 to C 16 A Critical Evaluation of Experimental Data. *J. Chem. Eng. Data* 1996;41(4):657–68. <https://doi.org/10.1021/je960058m>.
- [165] Messerly JF, Guthrie GB, Todd SS, Finke HL. Low-temperature thermal data for pentane, n-heptadecane, and n-octadecane. Revised thermodynamic functions for the n-alkanes, C5-C18. *J. Chem. Eng. Data* 1967;12(3):338–46. <https://doi.org/10.1021/je60034a014>.
- [166] Bazile J-P, Nasri D, Galliero G, Daridon J-L. Density, Speed of Sound, Compressibility, and Excess Properties of the Carbon Dioxide + n -Heptadecane Binary Mixture from 10 to 70 MPa. *J. Chem. Eng. Data* 2021;66(8):3245–57. <https://doi.org/10.1021/acs.jced.1c00311>.
- [167] Luning Prak DJ, Lee BG, Cowart JS, Trulove PC. Density, Viscosity, Speed of Sound, Bulk Modulus, Surface Tension, and Flash Point of Binary Mixtures of Butylbenzene + Linear Alkanes (n -Decane, n -Dodecane, n -Tetradecane, n -Hexadecane, or n -Heptadecane) at 0.1 MPa. *J. Chem. Eng. Data* 2017;62(1):169–87. <https://doi.org/10.1021/acs.jced.6b00542>.
- [168] Brostow W, Grindley T, Macip M. Volumetric properties of organic liquids as a function of temperature and pressure: Experimental data and prediction of compressibility. *Materials Chemistry and Physics* 1985;12(1):37–97. [https://doi.org/10.1016/0254-0584\(85\)90035-5](https://doi.org/10.1016/0254-0584(85)90035-5).
- [169] Würflinger A, Mondieig D, Rajabalee F, Cuevas-Diarte MA. pVT Measurements and Related Studies on the Binary System nC16H34 - nC17H36 and on nC18H38 at High Pressures. *Zeitschrift für Naturforschung A* 2001;56(9-10):626–34. <https://doi.org/10.1515/zna-2001-0904>.
- [170] Audsley A, Goss FR. 584. Atom polarisation. Part I. The solvent-effect theory and its application to the molecular refraction and polarisation of n-paraffins in the liquid state. *Journal of the Chemical Society (Resumed)* 1950:2989–97.
- [171] I. R. Kirchevsky, A. A. Ilinskaya. *Acta Physicochim. USSR* 1945;20:327–48.

- [172] Madani SA, Mohammadi M-R, Atashrouz S, Abedi A, Hemmati-Sarapardeh A, Mohaddespour A. Modeling of nitrogen solubility in normal alkanes using machine learning methods compared with cubic and PC-SAFT equations of state. *Sci Rep* 2021;11(1):24403. <https://doi.org/10.1038/s41598-021-03643-8>.
- [173] García-Sánchez F, Eliosa-Jiménez G, Silva-Oliver G, Vázquez-Román R. Vapor–liquid equilibria of nitrogen–hydrocarbon systems using the PC-SAFT equation of state. *Fluid Phase Equilibria* 2004;217(2):241–53. <https://doi.org/10.1016/j.fluid.2003.05.002>.
- [174] Taylor BN, Kuyatt CE. Guidelines for Evaluating and Expressing the Uncertainty of NIST Measurement Results: NIST Technical Note 1297; Available from: <https://emtoolbox.nist.gov/Publications/NISTTechnicalNote1297s.pdf>.